Techniques in High Resolution Observations from the Ground and Space, and Imaging of the Merging Environments of Radio Galaxies at Redshift 1 to 4.

by
Eric Steinbring
B.Sc. University of Winnipeg 1993
M.Sc. University of Alberta 1995
A Thesis Submitted in Partial Fulfillment of the
Requirements for the Degree of
DOCTOR OF PHILOSOPHY
in the Department of Physics and Astronomy

© Eric Steinbring, 2000, University of Victoria.
All rights reserved. This thesis may not be reproduced in whole or in part,
by photocopy or other means, without the permission of the author.

National Library of Canada
Acquisitions and Bibliographic Services
395 Wellington Street
Ottawa ON K1A 0N4
Canada

Bibliothèque nationale du Canada
Acquisitions et services bibliographiques
395, rue Wellington
Ottawa ON K1A 0N4
Canada

Your file Votre référence

Our file Notre référence

The author has granted a non-exclusive licence allowing the National Library of Canada to reproduce, loan, distribute or sell copies of this thesis in microform, paper or electronic formats.

L'auteur a accordé une licence non exclusive permettant à la Bibliothèque nationale du Canada de reproduire, prêter, distribuer ou vendre des copies de cette thèse sous la forme de microfiche/film, de reproduction sur papier ou sur format électronique.

The author retains ownership of the copyright in this thesis. Neither the thesis nor substantial extracts from it may be printed or otherwise reproduced without the author's permission.

L'auteur conserve la propriété du droit d'auteur qui protège cette thèse. Ni la thèse ni des extraits substantiels de celle-ci ne doivent être imprimés ou autrement reproduits sans son autorisation.

0-612-58583-2

Canada

Supervisor: Dr. D. Crampton

Abstract

High resolution imaging and spectroscopy are invaluable tools for extragalactic astronomy. Galaxies with redshifts of 1 or more subtend a very small angle on the sky - typically, only about an arcsecond. Unfortunately, this is also approximately the angular resolution achieved with a ground-based telescope regardless of its aperture. Atmospheric turbulence ruins the image before it reaches the telescope but the emerging technology of adaptive optics (AO) gives the observer the possibility, within limitations, of correcting for these effects. This is the case for instruments such as the Canada-France-Hawaii Telescope (CFHT) Adaptive Optics Bonnette (AOB) and the Gemini North Telescope (Gemini) Altitude-Conjugate Adaptive Optics for the Infrared (Altair) systems. The alternative is to rise above the limitations of the atmosphere entirely and put the telescope in space, for example, the Hubble Space Telescope (HST) and its successor, the Next-Generation Space Telescope (NGST).

I discuss several techniques that help overcome the limitations of AO observations with existing instruments in order to make them more comparable to imaging from space. For example, effective dithering and flat-fielding techniques as well as methods to determine the effect of the instrument on the image of, say, a galaxy. The implementation of these techniques as a software package called AOTOOLS is discussed. I also discuss computer simulations of AO systems, notably the Gemini Altair instrument, in order to understand and improve them. I apply my AO image processing techniques to observations of high-redshift radio galaxies (HzRGs) with the CFHT AOB and report on deep imaging in near-infrared (NIR) bands of 6 HzRGs in the redshift range $1.1 \leq z \leq 3.8$. The NIR is probing the restframe visible light - mature stellar populations - at these redshifts. The radio galaxy is

resolved in all of these observations and its 'clumpier' appearance at higher redshift leads to the main result - although the sample is very small - that these galaxy environments are undergoing mergers at high redshift. Finally, I look to the future of high resolution observations and discuss simulations of imaging and spectroscopy with the NGST. The computer software NGST VI/MOS is a 'virtual reality' simulator of the NGST observatory providing the user with the opportunity to test real observing campaigns.

Contents

List of Tables

List of Figures

Acknowledgements

I would like to thank David Crampton, John Hutchings, and Simon Morris of the National Research Council of Canada Herzberg Institute of Astrophysics for their invaluable support of, and advice on this work. I would also like to thank Colin Scarfe, Ann Gower, Chris Pritchet, and David Hartwick for making my studies at the University of Victoria possible; and Russ Robb for his assistance, which has made teaching undergraduate laboratories so rewarding. This work was supported in 1997 by a University of Victoria Fellowship and from 1995 through 1999 by a University of Victoria Graduate Teaching Fellowship.

Chapter 1

Introduction

1.1 Scientific Motivation for High Resolution Observations

One of the primary goals of modern observational astronomy is to understand the formation and evolution of galaxies. To do so we must peer across enormous distances at galaxies in order, by virtue of the finite speed of light, to see them as they were billions of years ago. However, looking across enormous distances means that these galaxies appear extremely faint and merely detecting them is a challenge. Fortunately, there are two powerful means of overcoming this obstacle. The first is to search for the most energetic of these galaxies. The second is to build very large telescopes.

Radio galaxies and quasars are immensely bright sources of radio emission probably powered by a $\sim 10^9\ M_\odot$ black hole driving an accretion disk. Ions accelerated in the magnetic field of this active galactic nucleus (AGN) emit synchrotron emission. This is observed in the form of a central peak and/or jets that terminate in a double-lobed morphology with a separation

of, typically, 30″ ($\sim 85\ h^{-1}$ kpc at $z = 1$) [1]. Their high luminosity facilitates detection in whole sky surveys made at radio wavelengths. For example, the 3C (at 178 MHz, Bennet 1962) and 4C catalogs (at 178 MHz, Pilkington and Scott 1965; Gower et al. 1967) contain several hundred such sources with fluxes greater than a few Jy.

These galaxies are also bright when observed in visible and near-infrared (NIR) light (the faintest from the 3C catalog having $K \approx 20$). One type of these objects has a bright central point source and, hence, is called a quasi-stellar object (QSO) or quasar. This point source, with blue nonstellar continuum and broad emission features, is the optical signature of the AGN. For $z < 0.6$ it might also be seen to reside within a galaxy much like those of the present universe (Bahcall et al. 1997 and references therein). The radio galaxy (RG), has a red, evolved, stellar continuum and narrow emission lines - although it looks much like the QSO in radio emission - and typically does not possess a bright point-source in the optical (de Koff et al. 1996 and references therein).

The great appeal of these objects is that their bright radio emission directs us to their optical counterparts from which a redshift can be determined. We can look nearby on the sky for objects at the same epoch and perhaps find members of the same galaxy environment. Historically, RGs and QSOs have been the galaxies of highest known redshift and by studying these objects one can hope to discover when star and galaxy formation began in the universe. We can follow them, using examples at various red-

[1]Here h is the dimensionless factor $H_0/100$ km s^{-1} Mpc^{-1}. Note, $1'' \approx 4$ kpc for $z = 1$ assuming $H_0 = 70$ km s^{-1} Mpc and $q_0 = 0.5$. Unless otherwise specified I will assume these physical parameters throughout.

shifts, from the early universe to more contemporary times. This allows us to determine how galaxies evolve in time. Now, it is possible that they are such bizarre objects that they do not represent the formation and evolution of typical galaxies, but they still offer us the opportunity to learn a great deal about the processes.

If we are to learn anything, though, we must study many examples of these galaxies including those at the highest redshifts and for this we need large optical telescopes. Not only that, the telescopes must be capable of resolving the same features seen in low redshift examples. Unfortunately, the optical component of a high-redshift RG or QSO subtends only about an arcsecond on the sky. Coincidentally, this is also about the effective limit of the resolving power of any ground-based telescope, regardless of size.

This resolution limit is set by the Earth's atmosphere. Turbulence distorts any image passing through it to the telescope and, typically, this means no object smaller than about an arcsecond can be resolved. One solution to this is to place the telescope above the Earth's atmosphere, but placing telescopes in Earth or solar orbit presents problems. Any instrument aboard this spacecraft must be very carefully designed. It is difficult or impossible to modify it once in orbit so it must be extremely reliable. Another solution is to build an instrument that can correct for atmospheric distortion and effectively accomplish the same goal with a ground-based telescope. This instrument is referred to as a adaptive optics (AO) system. It has some limitations. It requires a nearby bright star or a laser beacon to operate and it is difficult to achieve high resolution over a large area of sky. That sky is also brighter than that seen by the space-based observatory.

1.2 High-Redshift Radio Galaxies

The range of redshifts of the known radio galaxies spans from $z = 0.06$ for Cygnus A to well above $z = 3$. For example, Q 0902+34 at $z = 3.39$, 4C +41.17 at $z = 3.79$, and 6C 0140+326 at $z = 4.41$. It is well established that the most powerful low redshift radio sources are associated with giant elliptical (cD) galaxies, often the brightest cluster galaxies (BCGs). Studies of the environments of RGs and radio-loud QSOs ($0.5 < z < 1$) suggest that these reside in dense cluster environments (Yee and Green 1987, Hill and Lilly 1991).

The optical morphology of powerful RGs with redshifts greater than ~ 0.6 is dramatically different from that of those of lower redshift. They are clumpy and very irregular and generally appear as an extended string of knots with an apparent length of about an arcsecond that lies along the axis of the radio lobes (McCarthy et al. 1987, see McCarthy 1993 for a review).

The best optical imaging of these high-redshift RGs (HzRGs) has been obtained with the Hubble Space Telescope (HST) Wide-Field Planetary Camera 2 (WFPC2). These data were the product of an extensive program (~ 100 objects from the 3C and 4C catalogs), and have revealed very complex rest-frame ultraviolet (UV) morphologies down to the resolution limit of $\approx 0.1''$ (Longair et al. 1995; Best et al. 1996, 1997). These images reveal the immediate neighbourhood of the AGN host to be strings of knots with separations on the order of a few kpc aligned along the radio axis. These are embedded in a diffuse emission region with projected scales of ~ 50 kpc. Typically, several faint companion objects (~ 100 kpc projected radius from the host) are also found.

One of the major unanswered questions about the stellar population of HzRGs is whether it is young or old. Since the highest redshifts for RGs are in the 3 - 4 range, one might assume that they are very young systems since, for a universe with $q_0 = 0.5$, the look-back time is about 90% of the age of the universe.

A popular theory presented by Lilly and Longair (1984) is that most of the star formation in these systems took place in an initial burst at $z_{\rm formation} \sim 5 - 10$ and that minor star-formation episodes afterwords produce the dramatic morphologies in restframe UV light. At early times the stellar populations in these galaxies would be composed of O and B type stars. The main burst would decay and these populations would redden due to stellar evolution. If so, then RGs at $z \approx 2$ (4 Gyr after their burst of star formation) should be populated by mostly mature F and G type stars, and be bright at restframe visible wavelengths. This simple model can be studied for a variety of star-formation epochs using, for example, the spectral synthesis models of Bruzual and Charlot (1993). Their Galaxy Isochrone Synthesis Spectral Evolution Library (GISSEL) can output the K-magnitude of the model galaxy as a function of redshift which can be compared to observations. As can be seen in Figure 1.1 the simple model is reasonably successful in matching the $K - z$ relation for RGs but it is not the only way to account for the restframe UV light.

The alignment effect is suggestive of strong interaction along the radio axes. The high incidence of double and multiple component galaxies with separations of a few kpc suggests that these are in the process of merging in the direction defined by the radio axis (West 1994). Furthermore, it has

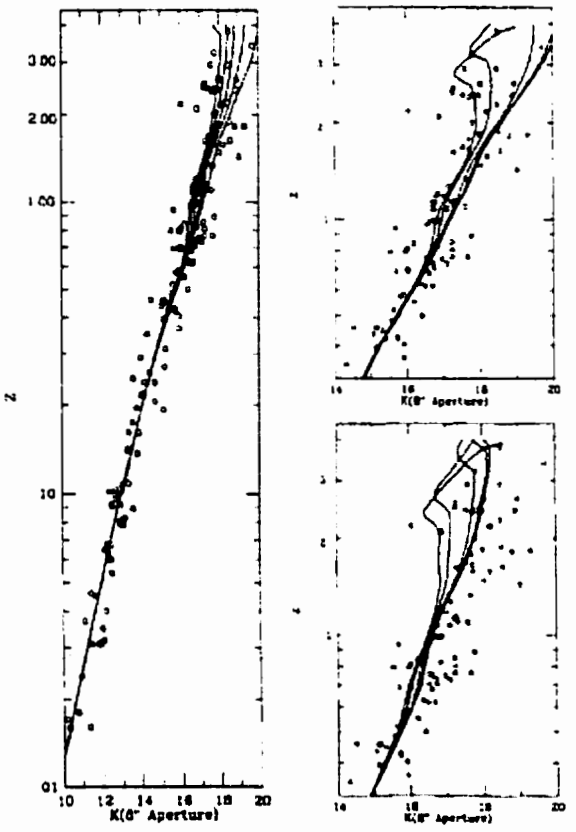

Figure 1.1: The $K-z$ relation for the 3C radio galaxies taken from McCarthy (1993). In the left-hand plot the curves show a passively evolving population of mass $1.5 \times 10^{12}\ M_{\odot}$ with $z_{\rm formation} = 20$ assuming $h = 0.5$ and $q_0 = 0.1$, 0.2, 0.3, 0.4, and 0.5. The left hand plots show the same data. In the upper plot the curves assume $h = 0.5$ and $q_0 = 0.1$ but $z_{\rm formation} = 30$, 20, 10, 5, and 4. The bottom plot assumes $q_0 = 0.5$ for the same values of $z_{\rm formation}$. It would appear that a simple model with an initial starburst and passive evolution can match the observed NIR magnitudes of RGs.

been suggested that star formation could be induced by the shocking of the intergalactic medium (IGM) by jets along the radio axis (Chambers & Charlot 1990). The high linear polarization ($> 10\%$) of the $z \sim 1$ galaxies from the 3C catalog seems to suggest that, at least at lower redshifts, scattering of AGN light from electrons or dust is important (Cimatti et al. 1997). Dey et al. (1997) find low polarization ($< 3\%$) for the $z = 3.8$ 4C +41.17 and suggest that, at higher redshifts, jet-induced star formation may provide most of the extended blue galaxian light.

1.2.1 Radio Galaxy Evolution

The restframe UV morphologies of HzRGs may be dramatic but in order to study galaxy evolution in HzRGs one should follow the mature stellar populations. If these populations are mapping out the structure of the 'true' galaxy one might well ask how this structure changes in time. Do these galaxies appear as elliptical galaxies from early epochs ($z \sim 4$) to the present or, if not, how do they evolve?

Deep, high-resolution NIR imaging allows the study of HzRGs to be extended to the most distant ones known. The great advantage of this is that once a RG is beyond $z \sim 1$, observations in the NIR are detecting radiation that was emitted at optical wavelengths in the restframe of the RG. This permits the investigation of the restframe-visible properties of RGs over a large range in redshift and enables the discrimination between opposing viewpoints on HzRG formation and evolution - mature, red, passively evolving ellipticals or young, bursting irregulars - by permitting studies of the morphology of the stellar populations of HzRG environments. Work on imaging HzRGs in the

NIR using the HST have been hampered by the failure of the Near-Infrared Camera and Multi-Object Spectrometer (NICMOS) in January 1999. Of the 11 objects imaged, all are of $z < 1.8$. Zirm et al. (1998) suggest that the NIR morphologies of these objects are more consistent with dynamically relaxed elliptical host galaxies.

1.2.2 Relationship between Radio Galaxies and Quasars

It has been long suspected that HzRGs with their double lobed radio morphology and extended optical (and NIR) morphology along the radio axis are simply QSOs seen at a different aspect. That is, they are observed with their radio axis projected against the sky instead of straight along the observer's line of sight. There are many arguments in favour of this. Radio galaxies and QSOs have similar radio fluxes and a simple geometric argument to unite the two follows a well established link between Type I and II Seyfert galaxies at low redshift. Recent studies of RGs and QSOs at $z > 2$ suggest they also probably reside in similar cluster (or proto-cluster) environments, with several companion galaxies within a projected distance of a few hundred kpc (e.g. the radio-galaxy MRC 0316-257, $z = 3.14$, Le Fèvre et al. 1996; quasars BR 1202-0725, $z = 4.69$, and BR 2237-0607, $z = 4.56$, Hu et al. 1996).

One way to demonstrate that RGs and QSOs are objects from the same population is to show that their radio lobe morphologies are similar. The only difference should be the apparent extent of the radio lobes on the sky. Lister et al. (1994) find that a simple model of projection can explain the differences in observed sizes for their sample of 114 QSOs and 78 RGs with $z < 2$. This type of test alone cannot *prove*, however, that the hosts of the

AGN activity are the same for HzRGs and QSOs.

Another method that might help determine if HzRGs and QSOs are from the same population is to show that the objects that host their AGNs are similar. This would mean determining the morphology of the stellar component and deep high resolution NIR imaging should be able to show if HzRGs and QSO host galaxies appear to be the same type of galaxy. There have been attempts to image the host galaxies of $1 < z < 4$ QSOs in the NIR with HST (Storrie-Lombardi et al. 1998) and AO (Aretxaga et al. 1998, Hutchings et al. 1998, 1999). Mostly these have been hampered by poor S/N and/or poor spatial resolution and do not definitively show that QSOs are hosted by galaxies similar to HzRGs.

Even without the added complexity of removing the light of the AGN from the QSO host galaxy and the achievement of high S/N it would be difficult to make this connection. If the QSO AGN were hosted by the same type of galaxy as an HzRG it might not look the same to an observer because the elongated structure would be foreshortened by its different aspect. The string of knots would be collapsed along the line of sight. However, the difference would seem to be less apparent as one considered knots further ($> 1''$) away from the central core objects. That is, if the QSO and HzRG environments are the same it should at least be surprising if the cluster environments of the two have different richnesses.

Here high resolution NIR observations are important. The compact faint companions of the HzRG are lost in ground based non-AO observations. So too for observations of QSOs. In fact, for QSOs the case is even worse because the wings of the bright AGN often obscure the region within a $2''$ projected

distance from the core. Thus, deep NIR AO observations can at least show if the nearby environments of QSOs and HzRGs are dramatically different, which would seem to suggest that they are different objects.

1.2.3 Sample Selection and Observation

Ideally, a study of the stellar environments of HzRGs should have a sample that covers a wide range in redshift and radio brightness. The major discovery surveys of RGs contain several hundred sources each. Thus, there are thousands of RGs from which to choose a sample that should satisfy these criteria.

The difficulty is, however, that *very* few of these galaxies will satisfy the selection criteria for observation with a natural guide-star adaptive optics system such as the Canada-France-Hawaii Telescope (CFHT) Adaptive Optics Bonnette (AOB) [2]. The major problem here is that a suitable guide-star must not only be bright but in close proximity on the sky to the RG. Thus, in effect, the selection criterion for the radio galaxy sample is purely based on the proximity of a guide star.

This may yield a very small sample but at least it is assured to be chosen without bias for a particular physical trait. Radio galaxy surveys select objects based on radio flux which is not at all dependent on the projected proximity of stars. One might suggest that their identification with an optical counterpart does prohibit ones with bright stars very close to, or, worse, superimposed on, the galaxy. But this will not, of course, correlate with radio brightness or redshift or any other intrinsic parameter of the RG sample

[2]This system is also referred to as Probing the Universe with Enhanced Optics (PUEO); usually written as Pueo. The name AOB will be maintained throughout this text.

either.

The work discussed here involves a program of deep imaging of HzRGs with the CFHT AOB that was designed to provide similar depth and resolution in the NIR as that provided by HST in the optical. This was undertaken at the suggestion of John Hutchings, David Crampton, and Simon Morris of the National Research Council (NRC) Herzberg Institute of Astrophysics (HIA) who, in late 1996, were also proposing to investigate QSO host galaxies with $z > 1$ by the same method. I had participated in some of their preliminary deep AOB imaging of QSO hosts during a commissioning run in June 1996. With this experience I, along with these collaborators, proposed for and received a 3-night run in June 1997 to investigate 5 HzRGs with $1 < z < 2$. After the success of this run we received 3 more nights in January 1998 and observed 5 HzRGs at $2 < z < 4$.

The aim of the HzRG study was to discover if the compact knots found in restframe UV had corresponding restframe-visible counterparts or if the stellar HzRG morphology was more like that of an evolved elliptical galaxy. I also hoped to determine if the cluster environments of HzRG and QSO samples were similar.

The failure of NICMOS has meant that a thorough program of NIR imaging of $1 < z < 4$ RGs will have to wait until a repair mission in March 2001. There is is no other published AO program involving HzRGs at the present time [3]. The situation is similar for QSO host galaxies. Fortunately, my involvement with the companion study of QSO host galaxy fields lead by John Hutchings has provided a direct comparison for the HzRG sample with

[3] Although 3C 294 has been observed with the University of Hawaii AO system (Stockton et al. 1999). These results will be discussed in Chapter 5.

imaging of similar resolution (Hutchings et al. 1998, 1999).

1.3 Dissertation Overview

The goal of this work has been to develop techniques to overcome some of the limitations of both space and ground-based high resolution observations. Some of these new techniques were employed in a study of the formation and evolution of RGs and QSOs.

The next chapter contains an introduction to concepts in AO and space-based observations with large telescopes. This begins by motivating high spatial resolution for telescopes by discussing the physical scales probed by sub-arcsecond imaging. A justification for building large telescopes - both with AO and in space - is presented. The imaging and spectroscopic instrumentation best suited to exploit these new observatories is outlined. Some groundwork in the theory of AO is then laid and a discussion is presented of the hardware that carries this out in a real system.

Several new techniques in the simulated and real observation with ground-based AO and space-based telescopes are discussed in detail in Chapter 3. Adaptive optics systems capable of obtaining deep high-resolution observations rivaling space-based telescopes is a recent advance in astronomy. In order to be competitive, the Gemini North Telescope (Gemini) Altitude-Conjugate Adaptive Optics for the Infrared (Altair) and other systems will need to overcome some serious limitations to the field of view (FOV) over which they can maintain good correction. A computer simulation that I developed for predicting this FOV is presented. Predicting the capabilities of the proposed Next-Generation Space Telescope (NGST) is not an easy

task either. It will be capable of observations that no present instrument can match. My novel computer simulation for investigating this instrument - a 'virtual reality observatory' - is presented. Although deep imaging of astronomical objects is not a new field, the possibility of deep AO imaging poses several unique challenges. The methods that I developed to deal with observing, image processing, and analysis for the CFHT AOB are discussed.

Simulated observations from the ground and space, based on the software detailed in Chapter 3, follow in Chapter 4. The results for simulated observations with Gemini Altair are presented. A method for improving the FOV by manipulating the control of the adaptive optical components is discussed. Suggestions for the design of imagers and spectrographs aboard the NGST are discussed based on realistic simulations of scientifically interesting observations.

Real observations and analysis using the CFHT AOB follow in Chapter 5. This is in the context of an imaging study of HzRGs. The results of this study and the implications for the environments of HzRGs at $1 < z < 4$ are given in Chapter 6.

Conclusions for both the instrumentation and scientific results along with some suggestions for future work are to be found in Chapter 7. A glossary of terms, including abbreviations, acronyms, and definitions, is included.

Chapter 2

Concepts for High Resolution Observations

2.1 Physical Scales Probed by Sub-Arcsecond Imaging

If we propose imaging of galaxies with resolution better than an arcsecond we should know what physical scales will be probed. In an Euclidean geometry (or a close enough approximation to one) distances can be measured using the familiar metric

$$ds^2 = dx^2 + dy^2 + dz^2 \tag{2.1}$$

where s is the distance and x, y, and z are the Cartesian coordinates in three dimensions. For measuring sizes of objects at cosmological distances, a cosmological treatment of the size-distance (or, at least size-redshift) relationship is in order. Assuming the universe is homogeneous and isotropic yields the Robertson-Walker metric. In polar coordinates Equation 2.1 is replaced with its equivalent for a curved four dimensional space-time (Peebles

1993):

$$ds^2 = dt^2 - a^2R^2[d\chi^2 + \sinh^2\chi(d\theta^2 + \sin^2\theta d\phi^2)], \tag{2.2}$$

where θ, ϕ, and $r = R\sinh\chi$, are the coordinates and t is time.

The physical length subtended by an angle of θ on the sky would then be (Peebles 1993)

$$l_{\text{physical}} = ar\theta. \tag{2.3}$$

That is,

$$l_{\text{physical}} = \theta/H_0F_\theta \tag{2.4}$$

where H_0 is the Hubble parameter in km s^{-1} Mpc^{-1} and the function

$$F_\theta = (1+z)/H_0a_0r(z) \tag{2.5}$$

is a dimensionless integral depending on the density parameter Ω for each z. These integrals have been solved and can be found, for example, in Peebles (1993). For $H_0 = 70$ km s^{-1} Mpc^{-1} and $\Omega_0 = 1.0$ with negligible cosmological constant this suggests $1''$ subtends a physical scale of $l_{\text{physical}} = 4.2$ kpc for an object at $z = 1$. This would be approximately 5.9 kpc if $H_0 = 50$ km s^{-1} Mpc^{-1}.

Thus, 5-20 kpc is also approximately the physical size of an HzRG based on the best optical observations with the Hubble Space Telescope (HST) (See Section 1.2). A typical knot within this galaxy is only $0.2''$ across or ~ 1 kpc in physical scale.

To measure the apparent brightness of objects we use a magnitude scale defined by

$$m = m_0 - 2.5\log f \tag{2.6}$$

where f is the flux and where m is the apparent magnitude of an object measured in factors of 2.5 from a zero-point of m_0. Now, the light from distant sources appears fainter and using Equations 2.4, 2.5, and 2.6 the distance modulus is given by (Peebles 1993)

$$m - M = 25 + 5\log[3000(1+z)H_0 a_0 r(z)] - 5\log h \tag{2.7}$$

where M is the absolute magnitude and the numerical factor in the logarithm is the present Hubble length, $c/H_0 = 3000h^{-1}$ Mpc. For $z = 1$ and $h = 0.7$ this gives a distance modulus of $m - M \approx 43$.

In summary, galaxies at high redshift will appear very faint and subtend a very small angle on the sky. Sub-arcsecond resolution is necessary in order to obtain information about HzRG morphology.

2.2 Resolving Individual Galaxies

An obvious advantage of very deep observations is that extremely faint galaxies, ones that otherwise would not provide sufficient flux, will become visible. It is important to estimate how many galaxies this will be. One reason for this is to know, as observations become deeper, if there will be so many galaxies visible on the sky that it will be difficult to discern one from another. This is a question of galaxy crowding. Empirically, the counts of the

number of galaxies per square-degree on the sky as a function of apparent magnitude is a steep function down to magnitudes of $B = 30$ - the faintest that any observations have reached to date (See Figure 3.9). This suggests that if galaxies were distributed randomly on the sky there would be about one for every 13 arcsec^2 of magnitude $B \approx 30$. Models of number counts that do not take into account evolution of galaxies suggest that this spatial density will level off for magnitudes fainter than this (e.g. Lin et al. 1999) but these models do not agree with the faint end of Figure 3.9. In any case, there will be a large number of galaxies visible in any imaging deeper than that obtained to date.

It should also be added that these galaxies will not be distributed randomly on the sky. The distribution of galaxies in the universe has a great deal of structure the exact details of which are beyond the scope of this work. The basic idea is that a galaxy is more likely to be found next to other galaxies. Empirically, this galaxy-galaxy correlation function is well described by a power law:

$$\xi(r) = (r_0/r)^\gamma, \tag{2.8}$$

where ξ is the probability of finding a galaxy within radius r and where $r_0(z)$ and γ are to be determined. The value of γ has been determined observationally for $z < 0.5$ to be about 1.8 and the form of r_0 well fitted by (Carlberg et al. 1998)

$$r_0 = 5.15(1+z)^{-(3+\epsilon)/\gamma} h^{-1} \text{ Mpc} \tag{2.9}$$

where $\epsilon = -0.6 \pm 0.4$. Using these numbers and assuming $h = 0.7$ gives

a value of $r_0 = 1.2$ Mpc at $z = 1$. Using the approximate value of 4 kpc arcsec^{-1} at $z = 1$ suggests $r_0 \approx 3'$ on the sky.

Another issue is the quantification of the morphology of the individual galaxies themselves. Mature passively evolved elliptical galaxies (such as types E and S0) and central bulges within galaxies have a typical morphology that is well defined by the empirical formula of de Vaucouleurs (1948):

$$\mu(r) = \mu_{\text{effective}} - 3.31[(r/r_{\text{effective}})^{1/4} - 1], \tag{2.10}$$

where μ is the surface brightness in mag arcsec^{-2}, r is the radius in arcseconds, and $r_{\text{effective}}$ is the radius within which half the light is emitted. An empirical formula that describes spiral galaxies (such as Types Sa, Sb, and Sc) and galaxy disks well is given by (Freeman 1970)

$$\mu(r) = \mu_{\text{central}} + 1.09(r/r_{\text{disk}}) \tag{2.11}$$

where μ is the surface brightness in mag arcsec^{-2}, r is the radius in arcseconds, μ_{central} is the central surface brightness, and r_{disk} is the radius at which the central brightness has fallen by a factor of e.

Generally, galaxies do not nicely fall into two catagories that are well described by either Equation 2.10 or 2.11. Their overall shape (excluding, say, bright star-formation regions) is, however, usually well described by some linear combination of the two. Ones that are not are referred to as irregulars (type Irr) [1]. The optical morphology of HzRGs is one example.

Historically, the determination of galaxy morphology and irregularity has been done 'by eye'. One useful alternative is to attempt to reduce the

[1]This division of galaxy morphology into three main groupings is due to Hubble (1926)

galaxy into a structure that maps out the brightest connected regions (called a skeleton) and use an algorithm to quantify the morphology. Some workers have attempted to develop more repeatable means of comparing galaxies based on this quantitative approach by, for example, using neural networks (Naim et al. 1997).

2.3 Large Astronomical Telescopes

The light gathering power of a reflecting optical telescope goes as the square of the diameter of its primary mirror. A second, and equally important consideration, however, is the quality of the images it delivers. That is, how extended is an image of a distant point-source at the focus of the telescope. This shape of stellar image is described by the point-spread function (PSF) and the narrower the PSF, measured by the full width at half maximum intensity (FWHM), the better. A narrower PSF also means a higher peak for a given amount of flux. The ratio of the peak height compared to its optimal value (no telescopic or atmospheric aberrations) is called the Strehl-ratio.

Although it is less expensive to construct a large (8 m) telescope on the ground (Gemini North Telescope (Gemini) construction $\sim$ 130 million Canadian dollars excluding instruments) as opposed to in space (Next-Generation Space Telescope (NGST) estimated at over 700 million Canadian dollars excluding instruments) there is a singular advantage to having a telescope above Earth's atmosphere. The quality of astronomical images is essentially perfect until they reach Earth's atmosphere. Here, turbulence distorts the images and no simple telescope, independent of aperture size, will restore them.

The only degradation of the image for a space-based telescope is due to the finite aperture of the telescope and imperfections in the optics, for example, the microscopic roughness ($\sim$ 5 nm root-mean-square (RMS)) in the surface of the mirror - 'micro-roughness'. A good approximation to the effect of micro-roughness on the PSF is to assume that some fraction of the photons are scattered out in random directions. The net effect is to have a sharp PSF that is amid a uniform halo of scattered flux. The reduction in Strehl-ratio due to this scattering is well approximated by (Mahajan 1983)

$$S_{\text{scattered}} \approx 1 - e^{-(4\pi\sigma/\lambda)^2} \tag{2.12}$$

where λ is the wavelength and σ is the RMS micro-roughness of the primary mirror.

Whether the telescope is on the ground or in space, what to do with the photons is the next question. We could simply apply direct imaging to the task. This would be of particular benefit for the case of space-based observations, as the lack of atmospheric distortions and large aperture necessarily implies excellent spatial resolution. Thus, tiny structures of only $0.1''$ diameter - say, knots in an HzRG - could be resolved. A polarizing filter would be useful as well. Highly polarized light would suggest that the knots are scattered light from an AGN while unpolarized light could suggest direct incoherent emission from star-formation regions.

Of course, we might want to resolve the light from an object in wavelength as well. A series of filters for the imager might be sufficient for low resolution spectroscopy to find the general shape of the galaxy spectral energy distribution (SED) in the optical and NIR. A dispersive spectrograph

would certainly be in order for higher resolutions. This could be used, for example, to find emission lines in the galaxy. Perhaps only one slit is needed. High angular resolution suggests that this slit might also be quite narrow. Almost all the flux of a point source would be contained within, perhaps, only an 0.1″ diameter aperture for an 8 m telescope in space.

This suggests, further, that an array of slits, all parallel to each other, could 'dissect' an extended object into spectra from regions only about 0.1″ apart. This integral field unit (IFU) would be a powerful tool for studying the complicated environment of a galaxy. For example, we might be able to discern an active galactic nucleus (AGN) in a QSO-host galaxy next to the star formation regions surrounding it by obtaining spatially resolved spectra - even if those regions are separated by only, say, 0.2″ on the sky. The full advantage of the high resolution and superior collecting power of the telescope seems to be gained.

Perhaps we do not want to obtain spatially resolved spectra of a single galaxy but spectra of many galaxies over a large field of view (FOV). In this case what is needed is a multi-object spectrograph (MOS). Many single slits are placed at the focal plane, one for each object of interest. This could be accomplished by way of a robotic arm moving optical-fibre-fed slits or a plate machined for each field. Spectra of all the objects could be obtained simultaneously.

There are other types of instruments that could be used to manipulate the flood of photons captured by a large telescope, but, for the most part, only imagers and dispersive slit-spectrographs will be discussed here.

Of course, these instruments and the telescope that feeds them are all

worthless without a device to record the photons that pass through. In all modern instrumentation for the optical and NIR a 2-dimensional focal-plane array electronic detector is used. This is a solid state device that has a photo-sensitive material arranged in a 2-dimensional grid. The most common of these is the charge-coupled device (CCD) although similar devices with different electronic architectures are also used. The design, and particularly the photo-sensitive material employed, is dependent on the wavelength of the photons of interest. An indium-antimonide (InSb) material with a broad region of sensitivity over 1-4 microns might work well in an extremely cold (40 K) detector designed for the NIR, but, if the device is intended for wavelengths shortward of 1 micron, a mercury-cadmium-telluride (MgCdTe) or hybrid visible silicon (HyViSi) [2] device will have a better response.

The choice of specifications will have a direct impact on the quality of the final image of, for example, the spectrum of the HzRG star-formation region. The size of the pixels should be made physically small enough that no spatial information is lost. That is, there should be two pixels across the full width at half maximum (FWHM) of the image of a point source (Nyquist sampling). The noise added to our images and spectra, then, is due only to the limited efficiency of the detector, the non-zero temperature (dark-current), and imperfections in the detector electronics.

It would seem that a large telescope in space with the right instrumentation can produce spatially resolved images and spectra of extremely faint objects. It would seem a pity that the same was not possible from the ground due to the Earth's atmosphere. The advent of adaptive optics (AO), an in-

[2]This is also refered to as a silicon-pin-diode device. The term HyViSi will be used throughout the text.

strument imposed in the optical path in front of the imager or spectrograph, is overcoming this hurdle as well. A feedback system involving a sensor (a digital imager as discussed above), a deformable mirror (a reflective surface that can be shaped with electronic actuators), and a computer communicating between the two can correct for the effects of the turbulent atmosphere.

There are obvious advantages to building a large telescope on the ground. The cost is much lower and the telescope is easily accessible for repairs and upgrading. There are some notable disadvantages as well. The area of sky that can be corrected by the AO system is small and since the telescope is on the ground there is additional background light due to the scattered and emitted light of the Earth's atmosphere. This makes the background brighter than from space, and although there is a lot of flux from, say, the star formation region of our HzRG and it is resolved, the contrast between it and the sky around it will be lower than from space.

Fortunately, there are methods to combat even these problems for the ground-based AO observations. These are typically done after the image or spectrum is recorded and are called post-processing. Given sufficient exposure time it is possible to make the quality of ground and space-based observations the same. The aim of this field of study and the goal of my work in particular is to make these techniques compatible and complementary.

2.3.1 Astronomical Adaptive Optics

I now discuss briefly astronomical AO. The goal is to describe the effect of the Earth's atmosphere on the PSF and elucidate the concepts of measuring and correcting it. More complete reviews of astronomical AO can be found

in Roddier (1981) and Beckers (1993).

When the wavefront from an object is emitted (let us assume a point source for simplicity) it expands uniformly in all directions in a spherical shell. To a distant observer a small section of this wavefront, say, a circular patch 8 m in diameter should be uniformly flat. That is, if we were to point an 8 m diameter Earth-orbiting telescope at that star (ignoring imperfections in the optics) a perfect diffraction-limited image of that star would be produced at the focal plane. The image would be the Fourier transform of a plane wave at the focal plane - a diffraction pattern containing all the flux captured by an 8 m telescope. Unfortunately, this would not be the case if that same telescope were transferred to a position on the ground. The image that results from the interposition of the Earth's atmosphere between the star and the telescope is far from a perfect diffraction pattern.

Consider the interface of air and a hot surface, say, over the roof of the ground-based observatory. The images that we see through this layer of air move rapidly and are distorted. This also occurs at higher-altitude layers in the Earth's atmosphere and, combined, the effect is to increasingly blur the image of the star.

Consider one such layer. Imagine a volume of air within that layer with a characteristic diameter of l, velocity v, and kinematic viscosity ν. If heated, that volume of air will rise smoothly. If these are the only important quantities a dimensional argument gives (the Reynolds' number)

$$R = vl/\nu. \tag{2.13}$$

As long as R obeys $R < R_{\text{critical}}$ for some R_{critical} the flow should remain

smooth. If that same volume of air attains $R > R_{\text{critical}}$ it will become turbulent. The basic idea is that turbulence occurs when the geometry changes faster than the kinematic viscosity can keep the entire flow moving in one direction. If we note that the kinematic viscosity of air is $\nu \approx 1.5 \times 10^{-5}$ m^2 s^{-1} and assume $v = 1$ m s^{-1} and $l = 10$ m, this implies $R = 6.7 \times 10^5$.

Kolmogorov (1941) turbulence is based on the assumption that the kinetic energy of these initial large scale motions is transferred to smaller and smaller scale motions. That is, the flow breaks up into smaller and smaller eddies (with smaller values of R_{critical}) and when R_{critical} gets small enough the process stops and the kinetic energy is dissipated as heat by viscous friction. Let's call this rate of dissipation per unit mass ϵ. Conservation of energy demands that ϵ must equal the rate of production of turbulent energy. Assume that the velocity v of motion at scale l depends only on l and ϵ - that is, only on the size and rate of dissipation of energy. A dimensional argument gives (Roddier 1981)

$$v \propto \epsilon^{1/3} l^{1/3} \tag{2.14}$$

and, furthermore, the kinetic energy is given by

$$E = 1/2mv^2 \tag{2.15}$$

where m is the mass of air in the volume. Thus, the energy scales from l to $l + dl$ as

$$E(l)dl \propto (\epsilon^{1/3})^2 (l^{1/3})^2 dl \propto l^{2/3} dl. \tag{2.16}$$

Thus,

$$\int E(l)dl \propto \int l^{2/3}dl \tag{2.17}$$

and, thus (the Kolmogorov law),

$$\int E(l)dl \propto l^{5/3}. \tag{2.18}$$

Typically, $l_{\text{smallest}} \sim 1$ mm and $l_{\text{biggest}} \sim 100$ m. The latter scale is on the order of the size of turbulent layers.

We now have the underpinnings of when turbulence will occur - given by the Reynolds' number - and how the energy will be dissipated according to scale - given by the Kolmogorov law. The next thing to note is that temperature is a function of altitude in Earth's atmosphere.

Consider again a single atmospheric layer. We define a variance in temperature T between two points $\mathbf{r}$ and $\mathbf{r}+\rho$ within the layer as

$$D_T(\rho) = < |T(\mathbf{r}+\rho) - T(\mathbf{r})|^2 >_{|\mathbf{r}}. \tag{2.19}$$

A dimensional argument demands, if we assume ρ, ϵ, and the rate of production of temperature fluctuations, η, are the only relevant quantities, that (Roddier 1981)

$$D_T(\rho) \propto \eta\epsilon^{-1/3}\rho^{2/3} \tag{2.20}$$

which is usually written as

$$D_T(\rho) = {C_T}^2\rho^{2/3}. \tag{2.21}$$

This means, on average, the variance in the temperature is proportional to $\rho^{2/3}$. The term ${C_T}^2$ is referred to as the structure constant of temperature variations.

Now, temperature variations in air, D_T, correspond directly to index of refraction variations, D_n. That is,

$$D_n(\rho) = {C_n}^2 \rho^{2/3} \tag{2.22}$$

where pressure equilibrium requires (Roddier 1981)

$$C_n \propto (P/T^2) C_T \tag{2.23}$$

and where P is the pressure.

Smooth flow in a layer of atmosphere with an altitude-dependent temperature difference becomes turbulent and mixed due to a scale-dependent viscous breakdown of the flow. This is also equivalent to saying that the smooth altitude dependence of temperature becomes mixed with the turbulent flow. Since temperature and index of refraction are related this is also equivalent to saying that the atmospheric layer will achieve a mixed index of refraction according to Equation 2.22.

Let us now consider the shape of our stellar wavefront as it travels through this turbulent layer to our telescope on the ground. We define a variance in the phase ϕ between the two points at positions $\mathbf{y}$ and $\mathbf{y} + \mathbf{x}$ on the *surface* of the wavefront as

$$D_\phi(\mathbf{x}) = < |\phi(\mathbf{y} + \mathbf{x}) - \phi(\mathbf{y})|^2 >_{\mathbf{y}}. \tag{2.24}$$

By analogy to Equation 2.20 and noting that $\int \rho^{2/3} d\rho \propto \rho^{5/3}$ we have

$$D_\phi(x) \propto {r_0}^{-5/3} x^{5/3} \tag{2.25}$$

in units of rad^2 where $r_0 = r_0(\lambda)$ is called the coherence length (or Fried parameter) and λ is the wavelength of light.

This is, however, only the effect of a single layer of turbulence. In reality the atmosphere will have several layers of turbulent flow and, thus, $C_n = C_n(h)$ where h is the altitude. One layer is associated with the temperature difference between the ground, telescope, and its enclosure and the surrounding air. A second layer occurs at approximately 1000 m above local ground-level where the day/night heating cycle is responsible. Since in this work the telescopes under consideration are well above this layer we will not be concerned with it. A third important regime occurs at the tropopause ($\sim$ 8000 m), where high wind shears contribute to the turbulence (Racine and Ellerbroek 1995).

The wavefront for a distant source must pass through these layers to reach the telescope and the variation of the wavefront is the addition of the effects of those layers. Furthermore, this distant source will seldom be one directly above the observatory and, thus, the variation in r_0 is also dependent on zenith angle α according to (Fried 1982)

$$r_0(\lambda, \alpha) \propto \lambda^{6/5} (\cos \alpha)^{3/5} (\int {C_n}^2 dh)^{-3/5}. \tag{2.26}$$

It is logical to ask over what angle on the sky the wavefront distortions are approximately the same. This is called the isoplanatic angle and can be approximated by (Fried 1982)

$$\theta \propto r_0/H \tag{2.27}$$

where H is the average over the turbulent layers defined as

$$H = \sec\alpha(\int {C_n}^2 h^{5/3} dh / \int {C_n}^2 dh)^{3/5}. \tag{2.28}$$

The region of sky thus defined is often referred to as the isoplanatic patch.

The advanced and retarded regions of the wavefront cause the blurring of the image at the focal plane of the telescope. This is the seeing - usually measured by the FWHM of the PSF at the focal plane. The Fourier transform of the wavefront at the pupil plane becomes the image at the focal plane. In mathematical terms, the primary mirror maps this pupil vector space into the image vector space. Every vector in the pupil space that does not map perfectly into a point source at the focal-plane distorts the image from a perfect point source. As long as we can advance the retarded part of the wavefront and vice-versa we can return the wavefront to a flat surface. A mirror that could deform itself to the shape of the incoming distorted wavefront could serve this purpose.

In order to achieve this shape first we need a mathematical representation of it. A popular modal representation is the Zernike polynomials (see, for example, Noll 1976). They are normalized to have an RMS of unity over the pupil and except for the piston term are the familiar modes that astronomers recognize from the focusing of a telescope. The piston term is given by

$$Z_1 = 1 \tag{2.29}$$

and represents a phase shift over the entire wavefront. Since we are not concerned with *when* the wavefront left the star this is not important. The second and third terms are referred to as the tip or tilt of the wavefront and are given by

$$Z_2 = 2r\cos\theta, \tag{2.30}$$

and

$$Z_3 = 2r\sin\theta. \tag{2.31}$$

In essence, these represent a drift in position of the point source. The fourth term, defocus, is given by

$$Z_4 = 3^{1/2}(2r^2 - 1) \tag{2.32}$$

which measures the spread of the PSF. There are an infinite number of aberrations beyond this as well.

The goal of an AO system is to match the highest possible number of Zernike modes in the surface form of the adaptive mirror. That is, to decrease the RMS variation in the wavefront to increase the flux falling into the shape of a perfect point source image at the focal plane. A measure of this correction of the wavefront is the Strehl ratio. It is the ratio of the height of the PSF delivered compared to the peak if the correction were perfect. It is also approximated by measuring the RMS variation in the wavefront in radians, σ, according to (Marechal approximation)

$$S \approx e^{-\sigma^2}, \tag{2.33}$$

where S is the Strehl ratio.

Another important aspect is to realize that these variations are constantly changing. It is the challenge of AO not to just build a device that can mimic the shape of the incoming wavefront but one that can take on many different shapes every second. Two important time scales are defined by the correlation length and the size of the telescope pupil. A typical value of r_0 is about 10 cm and a typical wind speed is $v_{\text{wind}} = 10$ m/s. This implies that for an 8 m telescope an entirely new wavefront shape the size of the pupil is presented every

$$\tau_{\text{pupil}} \propto D/v_{\text{wind}} \approx 0.8 \text{ s.} \tag{2.34}$$

The individual ripples on this overall shape - defined by the correlation length - are changing over a time scale of

$$\tau_{\text{higher order}} \propto r_0/v_{\text{wind}} \approx 0.01 \text{ s.} \tag{2.35}$$

Clearly, the adaptive components of a real AO system must operate at a frequencies well over 100 Hz.

Of course, it is not useful to be able to run adaptive optic elements at these frequencies if there is not a means of measuring the incoming wavefront variations at the same rate. There must also be a means of converting these measurements into voltages to drive those active elements. There are several methods for achieving this that are implemented in real working systems. Two main devices for measuring wavefront distortions are a Shack-Hartmann sensor and a wavefront-curvature sensor.

The Shack-Hartmann sensor measures the distortions in the wavefront

from a point source by dissecting it into a grid using a lenslet array. Each section of the grid images onto a 2-dimensional electronic detector. In this way the wavefront shape is broken down into a grid of measurements of image motion. Each of the small imagers reads out the brightest pixel in its array and, thus, the image position. A real-time computer is then able to reconstruct the original shape of the incoming wavefront.

The curvature sensing method is by means of a moving membrane which is perpendicular to the optical axis. This membrane vibrates at $\sim$ 100 Hz and forms intra- and extra-focal images of the pupil on a 2-dimensional detector array. This information permits the reconstruction of the Laplacian (instead of the scalar field as with the Shack-Hartmann sensor) of the wavefront shape. That is, it gives the local curvature over the pupil of the telescope.

In a real system there are usually two adaptive components in the optical path. The first is a fast steering mirror that corrects the second and third Zernike modes or tip and tilt. This must operate at $\sim$ 10 Hz to arrest image motion. A second component is a deformable mirror (DM). This is typically a continuous mirrored surface that can be manipulated by a grid of actuators pushing and pulling on the backside of the mirror to generate the shape of the remaining modes of the wavefront. This must operate at the much higher rate of $\sim$ 100 Hz to accomplish this task. The configuration of the adaptive components is generally to place them in front of the WFS and run the system as a closed loop. That is, the computer interprets between the two components and applies a correction to the adaptive components based on wavefront measurements and then senses the result. It makes another correction based on this. The net effect is a system that is constantly 'honing'

in on the correct wavefront shape.

Another important consideration is how the telescope is pointed during the operation of the AO system. Assume the WFS is placed in the optical axis of the telescope and a dichroic feeds the AO system with visible light while the NIR is sent to the imager. In the case of a natural guide-star system the telescope is pointing at a bright star and the isoplanatic patch is centered on that star. This arrangement is perfect as long as the guide-star is the target object. It certainly can be the case if the guide-star is actually, say, the bright core of an active galaxy. Perhaps the target object is nearby - within 10″ of the guide-star. This also would be effective as long as the detector used to provide imaging allowed for a sufficient FOV to include the target object. If not, then somehow the telescope must be pointed at the target object while simultaneously providing light for the AO system.

This is accomplished by means of a pick-off mirror feeding the WFS. This way the telescope can slew to the 'off-axis' position, that is, point at an object other than the guide-star while the AO system is operating. In this new configuration the isoplanatic patch is, of course, still centred on the guide-star but the imager is centred on the target object. From now on the term off-axis will be used to denote offset positions from the 'on-axis' guide-star. The farther away in offset from the guide-star an object is the farther it is off-axis, and as we might expect, the poorer the correction obtained. In fact, if the offset is much more than an arcminute off-axis there is essentially no correction obtained for the PSF. That is, the PSF is essentially that of the natural seeing conditions without AO. Of course, if the natural seeing becomes worse so too does the corrected PSF - on-axis or off-axis.

This variation in the PSF is not a concern as long as we can record the PSF throughout an observation. As long as the PSF is known we may perform a deconvolution on the image to restore it to what it would appear like under better seeing conditions.

This mathematical process amounts to using knowledge of the PSF to guess at what the image would look like if the PSF were narrower. If that guess is a good one the flux contained in a stellar image remains the same but its FWHM decreases. Similarly, an image of an extended object will be sharpened but only as expected from a narrower PSF. In fact, we might imagine that if an image of a star were deconvolved completely using a very accurate PSF it should converge to the solution that all the flux in the star was contained in a single pixel in the image. This is, in fact, what happens. It is generally very difficult to know the PSF this accurately and, thus, the deconvolution of *extended* objects is often seen as a 'black art' and rather suspect.

Of course, if we can deconvolve an image the reverse process must be possible. If we know the PSF (normalized to have a total flux of unity) a convolution can be performed. In the case of the image of a star deconvolved to have all of its flux in one pixel, this would converge on the original image before deconvolution.

2.3.2 Ground-Based Telescopes with Adaptive Optics

Astronomical AO systems were at first primarily designed for existing 4 m class telescopes such as the Canada-France-Hawaii Telescope (CFHT). This observatory was constructed in the 1970s and is situated at the peak of the

extinct Mauna Kea volcano in Hawaii. Its superb site already affords excellent natural seeing conditions. The observatory is situated at an elevation of about 4000 m which is above the diurnal heating layer. Steady undisturbed airflow at the observatory location provides less surface layer turbulence than other sites even on the same peak. The observatory floor is refrigerated and the dome air kept cool by means of retrofitted vents and fans in order to maintain as little difference as possible in temperature between the telescope enclosure and the surrounding air. This results in natural seeing of approximately 0.65″ FWHM (yearly median value).

The present generation of large ground-based astronomical telescopes such as Gemini have apertures of 8 m or more. Gemini is also situated on Mauna Kea and likewise provides excellent seeing conditions. The reduction of turbulence due to the telescope and enclosure has been a major aspect of the design. Huge vents integrated into the telescope enclosure can be opened to provide smooth circulation of air over the telescope. Unlike CFHT, Gemini was designed with AO instrumentation in mind.

The CFHT and Gemini systems both use natural guide-stars (although the Gemini system may be retrofitted with a laser guide-star) and are instruments mounted at the Cassegrain focus of the telescope. For the CFHT Adaptive Optics Bonnette (AOB) the WFS employed is of the curvature-sensing type. For the Gemini Altitude-Conjugate Adaptive Optics for the Infrared (Altair) system a Shack-Hartmann sensor is employed. Another difference between the AOB and Altair systems is that the Altair optical path places the DM at an image conjugate to an altitude of 6500 m above the pupil of the telescope. This will increase its delivered isoplanatic patch

size by optimizing the system to correct for the main atmospheric turbulence layer above the telescope (the ground layer effects being reduced by Gemini's specially designed enclosure). This approach presents some complexities in the design of the optics. One difficulty is that the DM must be larger than the image of the telescope pupil.

Although spectroscopy may be performed on images after compensation with these systems we are only concerned here with direct imaging through broadband filters. In both cases the telescope can image through standard filters such as R, I, J, H, and K onto large format CCDs or NIR detectors. For CFHT the optical imager is the Faint Object Camera (FOCAM), a 2048 $\times$ 2048 pixel ($2' \times 2'$ FOV) CCD. In the NIR the original instrument during commissioning was the small format, 256 $\times$ 256 pixel ($9'' \times 9''$ FOV), Montreal Near-Infrared Camera (MONICA) which has since been replaced with the large format 1024 $\times$ 1024 pixel ($36'' \times 36''$) Infrared Array (KIR).

2.3.3 Space-Based Telescopes

The existing space-based optical and NIR telescope is the 2.4 m HST. Its 8 m class successor is the NGST which is to be launched in 2009. The HST is an Earth orbiting observatory. This means it suffers from both scattered light off the Earth and the blockage of targets by the Earth during its orbit. The NGST will benefit from a fainter background and an extremely cold environment ($\sim$ 40 K) due to its orbit at the anti-Solar Lagrangian point (L2).

The primary imaging instrumentation aboard the HST consists of the Wide-Field Planetary Camera 2 (WFPC2) and the Near-Infrared Camera

and Multi-Object Spectrometer (NICMOS). The WFPC2 is an optical imager with a suite of filters including equivalents to the standard broadband U, B, V, R, and I. It is composed of 4 large format 1024 $\times$ 1024 pixel CCDs ($2' \times 2'$ FOV). The 512 $\times$ 512 pixel ($50'' \times 50''$ FOV) NIR imager within NICMOS has a separate suite of filters including equivalents to J, H, and K.

Chapter 3

Techniques in High Resolution Observations

3.1 Adaptive Optics Imaging with the Gemini North Telescope

Experience with the Canada-France-Hawaii Telescope (CFHT) Adaptive Optics Bonnette (AOB) suggests that changes in natural seeing result in variation in the delivered point spread function (PSF) over course of minutes. The delivered Strehl ratio and full-width at half-maximum (FWHM) can vary by more than a factor of 2 over the course of hours. Moreover, objects which happen to have a nearby star bright enough for the wavefront-sensor (WFS) are very rare. Typically, correction is made with a star which is offset 10″ to 30″ from the target and the PSF is worse for increasing offset. The difficulty in obtaining empirical measurements of this variation is that the effects of changing seeing and changing anisoplanatism are mixed. A numerical simulation can elucidate matters by modeling the anisoplanatic effects in isolation.

A simulation will need at least one synthetic turbulence layer. It will also need an artificial deformable mirror (DM) and WFS and a synthetic control algorithm interpreting between the two. A great deal of utility would be gained by the ability to easily modify the parameters of the synthetic AO components and determine if there is a means of reducing the anisoplanatism of the system. This might entail a means of extrapolation of the DM voltages to outside the illuminated WFS region. There already exist sophisticated numerical AO simulations with published results (Northcott 1991, Rigaut et al. 1994). The simulations of both Northcott and Rigaut were designed to predict the performance of the CFHT AOB and Gemini North Telescope (Gemini) Altitude-Conjugate Adaptive Optics for the Infrared (Altair) systems. However, they were primarily motivated by the need to determine the delivered on-axis PSF. The off-axis results did not include the effect on anisoplanatism from extrapolation of DM voltages.

I have developed AO computer simulations in order to model anisoplanatism. In January through March 1998, under contract to the National Research Council of Canada (NRC), I built a simulation to assist the Herzberg Institute of Astrophysics (HIA) team in the preliminary design of the Altair AO system for Gemini. It might have been possible for me to modify Rigaut's code (to which I had access) to study this effect. However, this simulation is very complicated and since it employs several turbulence layers it would have been difficult to be sure that *only* anisoplanatism was being tested. My simulation employs a single synthetic turbulence layer. It simulates the telescope pupil, the tip-tilt and DM, and the WFS along with their control algorithms in order to predict the off-axis PSF for offsets up to 60″. Most importantly,

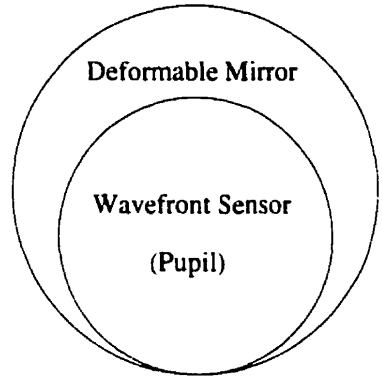

Figure 3.1: The Altair-Offaxis pupil footprint on the DM. In the Altair design the target is centred on the DM instead of the pupil.

it permits the adjustment of the control algorithm in order to minimize the degradation of the PSF and Strehl-ratio with offset. This aspect of 'slaving' actuator voltages in the DM for what would be an unilluminated region of the WFS was not employed in any available software at the time. The resulting simulation, Altair-Offaxis, is written in Interactive Data Language (IDL) and calculates the off-axis degradation in the corrected wavefront for an AO system. It does this by measuring the Zernike modes for the illuminated region of the WFS and then applying a correction to the DM - extrapolating to the 'unilluminated' region of the DM (See Figure 3.1). The extrapolation of the Zernike modes to study the anisoplanatic behavior of Altair was suggested by Glen Herriot of the HIA. The design of the software was my own. The goal of this project, as presented to me, was to study the effect of introducing hysteresis into the DM motion. It was suspected that significant hysteresis might cause a serious time-lag in the response of the DM. This, in turn, could cause more severe anisoplanatism. A commercial DM with less

hysteresis might be purchased at higher cost and it was necessary to know early in the design process if this was warranted.

3.1.1 Artificial Atmospheric Turbulence

In order to develop a computer model of an AO system we need to simulate the effects of atmospheric turbulence. This amounts to determining the surface of a plane-wave after it has travelled through a single turbulence layer. A digital representation of this surface is called a phase-screen. That is, it is the record of the result of randomly advancing or retarding sections of the wavefront as the result of Kolmogorov turbulence. Equation 2.25 describes the variance in the phase we would expect for this phase-screen as a function of separation on the surface of the plane-wave. This is for a plane-wave passing through a single turbulence layer of given coherence length. Thus, this equation gives a statistical description of the amplitude of the advanced or delayed regions of the wavefront and any recipe for synthesizing the effect of turbulence only needs to satisfy it.

We can imagine an algorithm to generate a phase-screen. Consider a 2-dimensional array of pixels as wide as the pupil of the telescope and many times that in length. That is, it has sufficient resolution across the pupil that each pixel is much smaller than r_0. Since the phase-screen is also many pixels long we can imagine 'pulling' this image over the pupil of the telescope at a typical wind-speed. The values of the pixels in the phase-screen are set by taking the Fourier transform of a spectrum assuming Kolmogorov statistics (Equation 2.18) (Cochran 1985). This method has been employed by Rigaut (1994) to generate phase-screens that satisfy Equation 2.25 and I obtained the

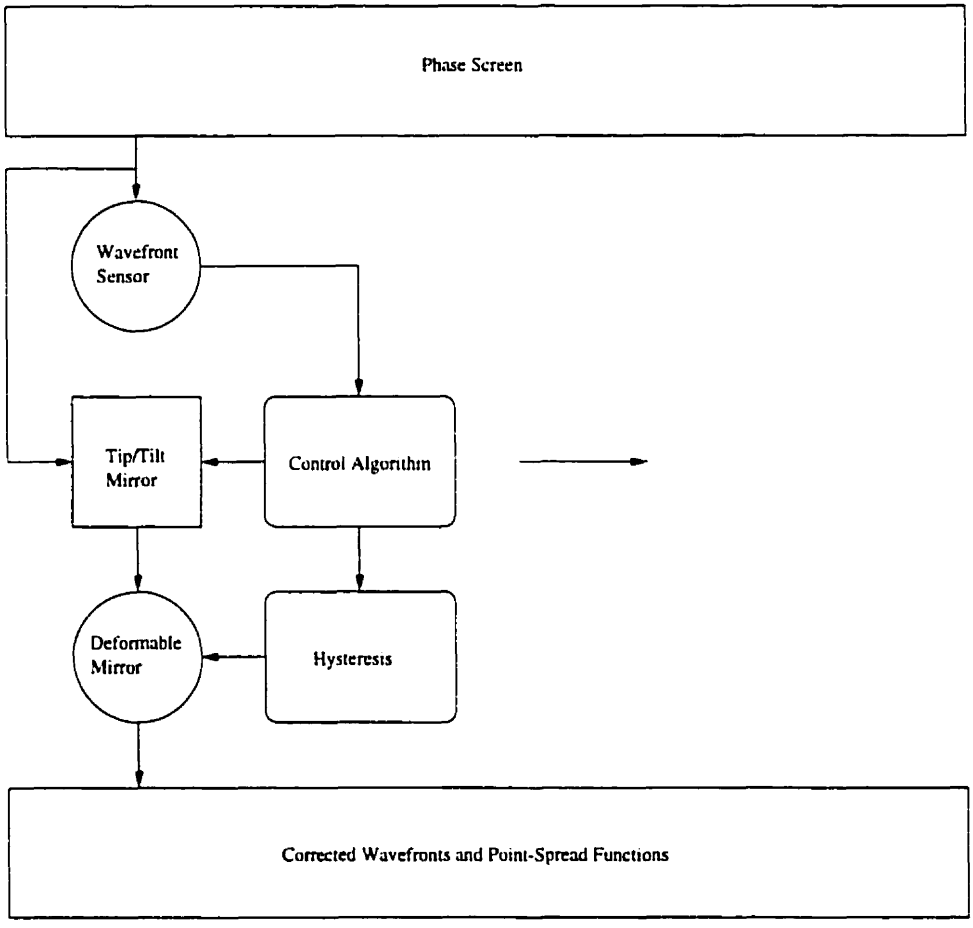

Figure 3.2: The Altair-Offaxis software architecture.

phase-screens employed in my code from him. These screens simulate single layer Kolmogorov turbulence with an r_0 that can be scaled by resampling the pixel scale of the images.

3.1.2 Synthetic Adaptive Optics System

The simulation operates by presenting a synthetic WFS with an image of the phase-screen at several time-steps. The WFS 'measures' the surface by decomposing it into a representation using the Zernike basis. The Zernike coefficients are calculated for the pupil section of the WFS after the prescription of Roddier (1994).

Piston mode is removed from the phase-screen prior to calculation of the coefficients by subtracting the average of the pupil section. The simulation assumes perfect wavefront sensing and its transformation into voltages for the DM. That is, it calculates the correction of up to 105 Zernike-modes for a phase-screen passing over the pupil of a circularly symmetric unobstructed telescope. Model output voltages are calculated for both the pupil (illuminated guide-star footprint) and the 'dark' (unilluminated) region of the DM (See Figure 3.3). The Zernike coefficients for the pupil are simply assumed to hold outside.

The user can prescribe how many Zernike-modes should be corrected for inside and outside the pupil, although tip-tilt correction will always be applied. The user can correct up to the same number of modes (to a maximum of 105) outside the pupil as inside. The program bins the voltages corresponding to defocus and higher order modes into a grid of user-specified dimensions to simulate the DM. Typically, there will be many more input

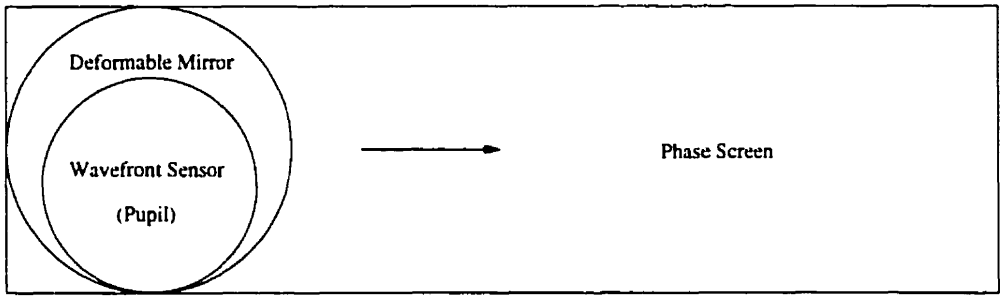

Figure 3.3: The configuration of the DM and pupil-footprints on the phase-screen in the Altair-Offaxis simulation.

modes than degrees of freedom in this model DM. Thus, the effect is to have the number of corrected modes limited purely by the chosen resolution of the DM and by hysteresis. Hysteresis can be applied to each DM actuator voltage based on a model for magnetic hysteresis of Cortial et al. (1997).

As an alternative to Zernike-mode correction, slaving may be used to extrapolate voltages for the dark actuators and a prescription is illustrated in Figure 3.4. Here, the centre pixel is an illuminated actuator at the edge of the WFS, the immediately adjacent actuators are within a user-specified number of pixels, and the rays emanating from the four sides of the box are also of a user-specified length. Each illuminated actuator around the edge of the pupil has that voltage slaved to the dark pixels surrounding it. When more than one illuminated actuator influences a dark actuator the voltages are averaged.

To facilitate easy comparison of results, perfect correction can be applied inside the pupil, independent of any extrapolation that takes place in the dark region. Other options allow for the position of the guide-star to be moved, the degree of turbulence to be varied, and the modeling of hysteresis for the

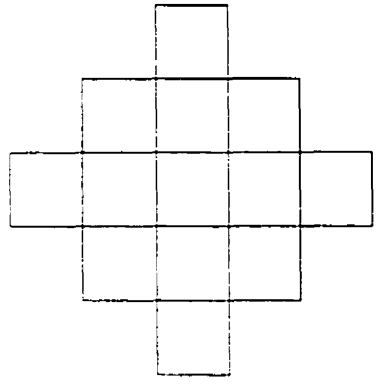

Figure 3.4: The Altair-Offaxis slaving function. The central actuator is an illuminated one nearest the edge of the WFS. The user can give a prescription for slaving the other actuators to this voltage.

DM actuator voltages. The guide-star can be offset from the optical axis of the telescope. The offset is perpendicular to the wind direction and increases towards the south as depicted in the output images. This configuration permits the calculation of the off-axis Strehl-ratio to a distance of about 60″ for Gemini.

The output actuator voltages are boxcar-smoothed to simulate the surface of the DM. The output mirror figures (both the tip-tilt mirror and the DM) are then subtracted from the input phase-screen.

3.1.3 Synthetic Off-Axis Imaging

The PSF of a point source at the image plane of the telescope is the Fourier transform of the wavefront at the pupil. Thus, to determine the off-axis PSF, Fourier transforms of regions the size of the telescope pupil are calculated for several positions on the corrected wavefront. These are essentially images of (uniformly bright) stars as seen through the AO system. They correspond

```
                    Altair-Offaxis

  1     Pixel scale in arcseconds per pixel
128     Speed of simulation in pixels
 10     D/r0 at the observation wavelength
 48     Position of the guide in pixels above the bottom edge of the display
 18     Number of actuators spanning the DM
  1     Half the size of the box over which to slave actuators (slaving function)
  1     Length of the finger over which to slave actuators (slaving function)
yes     Apply perfect correction inside the pupil
yes     Calculate the Zernike basis
105     Highest calculated Zernike order
 11     Highest extrapolated Zernike order
yes     Apply hysteresis to the DM voltages
```

Figure 3.5: The Altair-Offaxis parameter file. The speed, resolution, D/r_0, order of Zernike-correction, and slaving mechanism can be specified.

to the guide-position and several offset positions - target positions - for the telescope. The Strehl-ratios of all of these synthetic AO PSFs are calculated by comparing their peak height to the peak height they would have had if the corrected wavefront were perfectly flat. The PSFs are recorded at each time step. At the end of the simulated exposure they are averaged and the delivered Strehl-ratios for the guide-star and target positions are given.

The program is designed to maximize the resolution of the DM for the simulation and emulate the configuration of the Altair system for observations in H-band. The DM is circular and 128 pixels across. The telescope pupil is 96 pixels across (75% of the DM area projected on the sky). Each pixel thus corresponds to approximately 2″ on the sky. The phase-screen is 1024 pixels in length and for a typical scaling of $D/r_0(1.65 \text{ microns}) = 80$ would correspond to a volume of air approximately 12 km long. The user inputs the wind-speed in pixels/iteration with a typical value being about 8. Thus, for iterations of 0.01 seconds the program spans 1200 r_0 and simulates

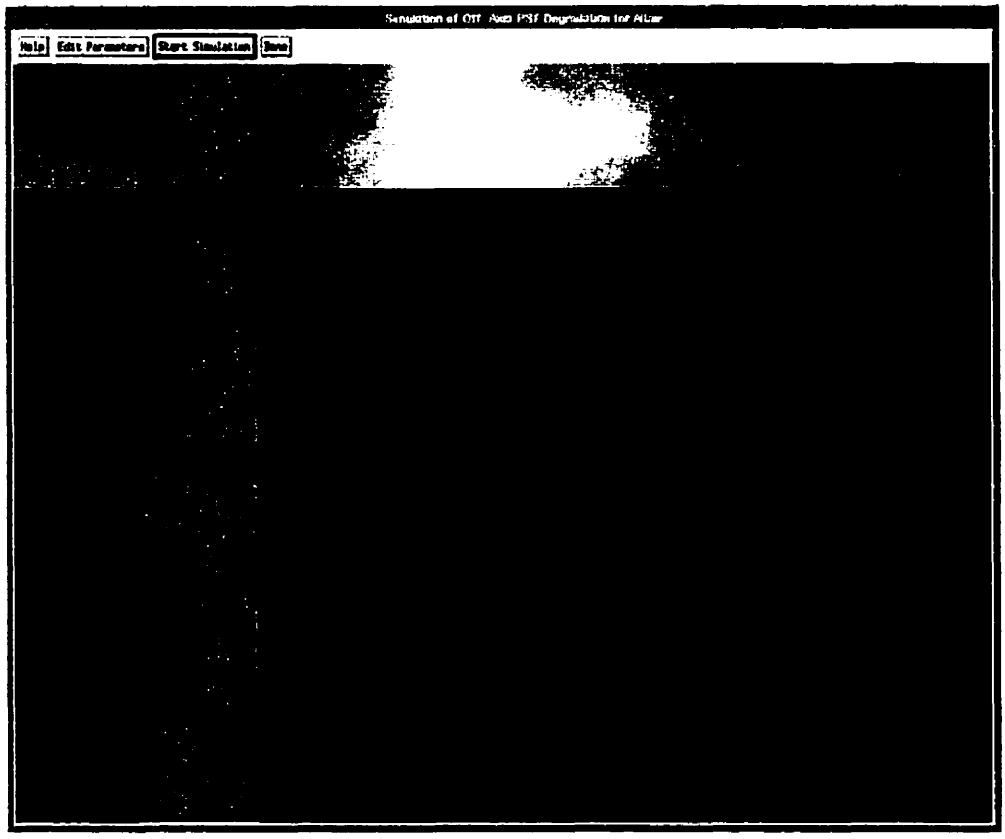

Figure 3.6: The display for the Altair-Offaxis software. During a simulation the display consists of 6 rows of images. The phase-screen is displayed along the top row. The section of the phase screen presented to the WFS for the current iteration is overlaid. Below is the section of phase-screen projected on the DM for the pupil. Below these are the resultant mirror figures for the tip-tilt and DM. Next, the sum of the tip-tilt and DM figures. Lastly, the resultant phase-error projected on the DM. When the simulation is completed, the co-addition of each is presented in their respective rows.

a windspeed of about 10 m s^{-1} with a total exposure of 1-1.5 s.

3.2 Observing with the Next-Generation Space Telescope

Although it is clear that the Next-Generation Space Telescope (NGST) will be a powerful instrument for deep imaging and spectroscopy in the optical and near-infrared (NIR) it is not clear what instrumentation will best exploit this regime. Since NGST will be a unique facility capable of observations deeper than any instrument yet built a numerical simulation is probably the only way of predicting what we will see. A simulation must provide artificial deep fields with synthetic stars and galaxies fainter and at higher resolution than NGST will be capable of. Since the instrumentation for this observatory is not yet designed (it is not even known what the complement of instruments will be!) a simulation must provide a wide range of imaging and spectrographic capabilities.

In January through September 1999 I built simulations in order to assist in early design proposals for the NGST Integrated Science Instrument Module (ISIM) by the NRC/HIA and the Canadian Space Agency (CSA). By extrapolating the results for the Hubble Space Telescope (HST) Wide-Field Planetary Camera 2 (WFPC2) and Near-Infrared Camera and Multi-Object Spectrometer (NICMOS) I have created a simulation of what deep galaxy fields and globular cluster fields will look like for the NGST. The user can choose how to extrapolate the HST number counts, how dense the fields should be, and what the background should look like. The simulation includes the three main telescope designs including mirror coatings and micro-

roughness as well as a model of the background zodiacal light - with solar absorption features - based on telescope orbit.

There are several options for the design of a Multi-Object Spectrograph (MOS) for NGST. They differ in their means of directing the light of the sources into the spectrograph. However, all configurations will require the determination of an optimal slit size. At the suggestion of David Crampton of the HIA, a numerical simulation was designed to determine the effect of slit size on the S/N of an extracted spectrum of a galaxy.

The original test program was designed to study a single galaxy with a single slit of variable size. An archival B-band image of M 51 was scaled both in pixel sampling and brightness to match its appearance if imaged by NGST. Furthermore, this scaling could be altered to simulate its appearance if it were at different redshifts and for different exposure lengths. A template spectrum of an Sb galaxy was obtained and shifted according to the user-defined redshift. The brightness of the image was scaled by the resulting spectral energy distribution (SED) for many wavebands and thus an artificial spectrum for each pixel was determined. A rectangular aperture could be selected and placed on this 'spectral-image'. By applying a spectral-response curve for a broadband filter as well as the quantum efficiency for a given detector, direct imaging of this field could be simulated. The light passing through could also be dispersed to create the output of an artificial spectrograph. A region of interest could be selected from this spectrum to yield an extracted spectrum. Finally, the S/N of this extracted spectrum was output. By varying the size of the aperture the user could determine the optimal S/N. In order to determine the background light a model based on

Wheelock (1994) was employed. This was suggested by Simon Morris of the HIA. This simulation was made even more realistic by including the effects of detector gain, readout and shot noise, and by performing the integration as a co-addition of many 1000 s exposures.

These investigations suggested that even a bright galaxy such as M 51 would not be detected in imaging by NGST (total exposures of $\sim 10^6$ s) if it were at $z > 2$. Others (e.g. Burgarella et al. 1998) have come to the same conclusion using similar scaling arguments. My simulation also made it clear that $S/N = 10$ low-resolution spectroscopy of galaxies with apparent magnitudes much fainter than $H = 30$ would require exposure times greater than 10^6 s.

The goal of this investigation was to determine the optimal size of slits and possibly determine advantages and disadvantages to the various mechanisms for directing the light into the spectrograph. The initial investigation was inadequate because it did not simulate a realistic galaxy field as seen with the NGST. It also had only one slit. It was clear that although the technique of simulating a spectrograph was sound a better means of generating artificial NGST fields was needed. Furthermore, a means of expanding this single slit model to simulate a multiplexed observation would need to be devised. The key scientific programs that were simulated were chosen to match those of highly ranked proposals in the Design Reference Mission (DRM). The deep galaxy imaging and spectroscopy proposals of Lilly et al. (1998) drove the galaxy simulations while stellar fields were designed to simulate those in the proposal of Rich and Margon (1998).

In order to investigate these proposals I constructed a simulation of imag-

ing, image-slicing, and slit-spectroscopy for the NGST in the NIR. All aspects of the Multi-Object Spectrograph (MOS) performance are simulated including filters, slit-masks, gratings, detectors, and exposure-control. The MOS can perform automated surveys. It can undertake an imaging or spectroscopic survey, perform data reductions, take photometry, as well as extract and analyze spectra all automatically.

The large primary mirror alone suggests powerful imaging capabilities for NGST not only for near and mid-infrared wavelengths but also for wavelengths shorter than 1.0 micron. The NGST will have a pupil area roughly 10 times that of HST, and thus, a diffraction limit roughly 10 times smaller. It is easy to see that there will be a considerable advantage for NGST in collection area and spatial resolution. Also, this will be compounded by the improved performance of more advanced detectors than were available for HST. What effect these improvements have on real images and how to best take those observations - for example, what type of detector or pixel sampling to use - is not so clear.

At the suggestion of Paul Hickson of the University of British Columbia a simulation was developed to study the relative merit of a dedicated Visible Imager (VI) for NGST over using the NIR camera outside its optimal wavelength range. This was a natural extension of the earlier numerical simulation work that I carried out for the Canadian NGST MOS study. There the goal was to determine the advantages and disadvantages of various slit-mask designs for the MOS, but included in this was a simulation of broadband imaging with a simulated NIR camera. It appeared that the best means of comparing the VI and NIR camera (which in this simulation would be the

MOS imaging mode) would be a direct comparison of imaging of the same field with the two 'virtual' instruments. A means of generating artificial NGST deep galaxy fields had already been developed for the MOS simulations but improvements would be needed due to the better pixel sampling of the VI. Also, the NGST PSF would play a crucial role in the VI studies. Discussions with John Hutchings and Peter Stetson of the HIA suggested that optimizing the pixel scale of the VI at around 0.6 microns would make one of its advantages the detection of point sources. A simulation that quantified this advantage would be needed. It was decided that a simulation of a globular cluster field - one that could be superimposed on a galaxy background to simulate observations of extragalactic globular clusters - was needed.

In order to compare with the MOS imager directly I have constructed a simulation of imaging in the visible for the NGST. The VI simulation provides imaging through broadband filters. All aspects of VI performance are simulated including the number and coatings of reflective surfaces, filters, detector efficiencies, pixel sizes, readout, dark, gain, well depth, and duration and number of exposures. Like the MOS, the VI simulation can perform automated imaging surveys and reduction of data.

3.2.1 Artificial Deep Fields

To simulate deep imaging for NGST we need a realistic NGST deep field. We might begin from 'first principles' and generate an entirely artificial galaxy field given an expected luminosity function, size-magnitude relation, etc. Perhaps it could even include galaxy evolution. But this is dissatisfying because there will be no way to know what galaxy evolution NGST will see until

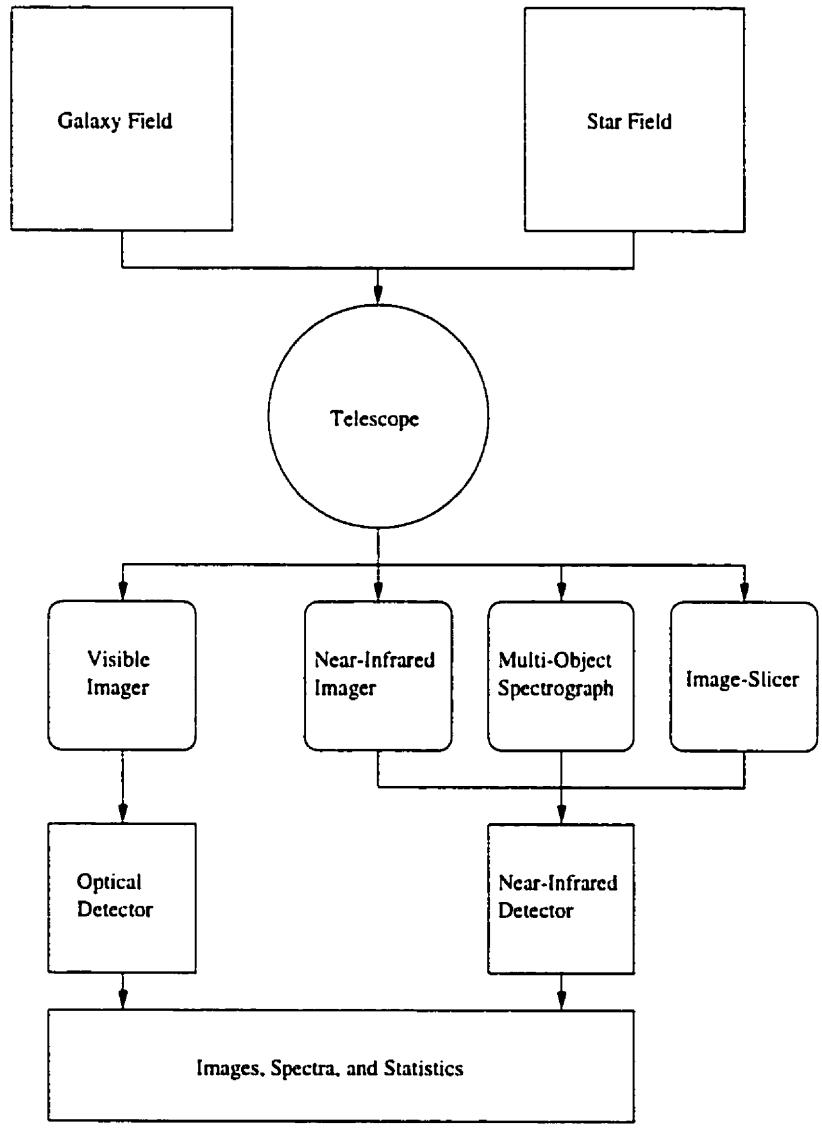

Figure 3.7: The NGST VI/MOS software architecture.

NGST can observe it. An alternative is to take the deepest known observations - those of the HST deep fields and extrapolate from them. This idea is similar to the method of Hubble Deep Field cloning by Bouwens et al. (1998). However, the goal of their method is mainly to alter the redshift distribution of the original HST WFPC2 deep fields without increasing the depth of the exposures. The goal discussed here is to add many new fainter galaxies to the deep fields - in effect, greatly increasing the depth of exposures. The simulation uses images from the HST NICMOS Deep Field South (HDFS) and photometric redshift survey data on the galaxies in this field to generate artificial NGST fields. It utilizes a model for the background illumination consisting of a scattered and thermal component of the zodiacal light. It has template spectra of four different galaxy types, E/S0, Sbc, Scd, and Irr which are redshifted according to a photometric redshift catalog. The galaxies are generated by spreading the H-band HST NICMOS image over the range of 0.5 to 5 microns according to the resulting SEDs.

The simulation generates the artificial NGST field by taking the faint galaxies from the HST field (say, $H > 25$), shifting them fainter by a few magnitudes and to a factor higher in redshift, making them smaller, and then putting them back into the field in randomized locations and rotations.

Since the galaxies in the original HST field are undersampled and noisy they are replaced in the simulation by artificial galaxies. They retain the spectral classification, brightness, redshift, and size of the original galaxies but these properties are used to generate highly oversampled artificial galaxy images. These morphological templates correspond to the four galaxy spectral types and are based on a two component model with an $r^{1/4}$-bulge and ex-

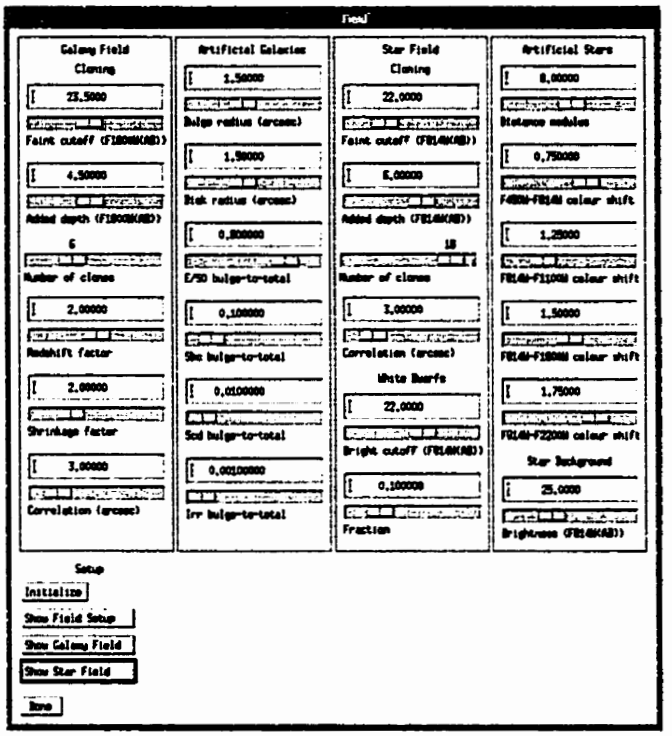

Figure 3.8: The control interface for NGST deep-field generation.

ponential disk. The disk is augmented with spiral structures, star-formation regions, etc., based on scaling an image of the brightest low-redshift spiral galaxy available in the HDFS. Also, by tuning the parameters of the simulation this disk structure can imitate the morphology of the most irregular objects in the HDFS. The resulting template galaxies are formed with user-supplied values for bulge and disk radii, and bulge-to-total ratios (B/T). Later, they will be convolved with the instrumental PSF of the NGST and resampled to the pixel sampling of the detectors.

Note that the spatial distribution of galaxies in the resulting field from this method is not entirely random. The galaxies are preferentially put down

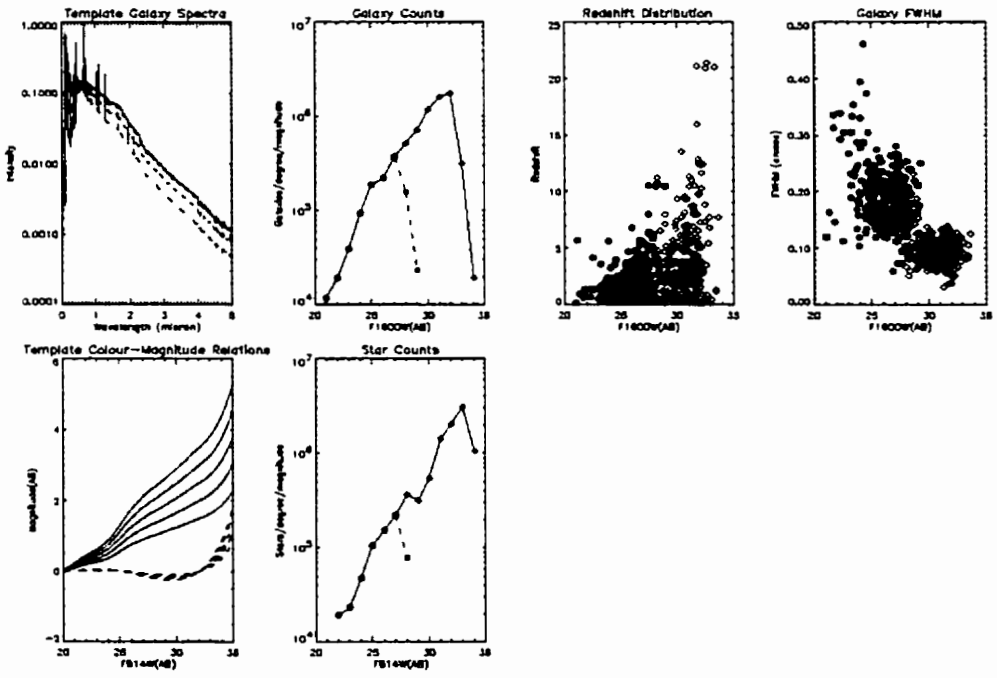

Figure 3.9: A display of various parameters for the artificial deep fields. The upper panel is for galaxies and the lower for stars. The user can adjust the cloning parameters to achieve an extrapolation for NGST (open circles) based on observed HST results (filled circles).

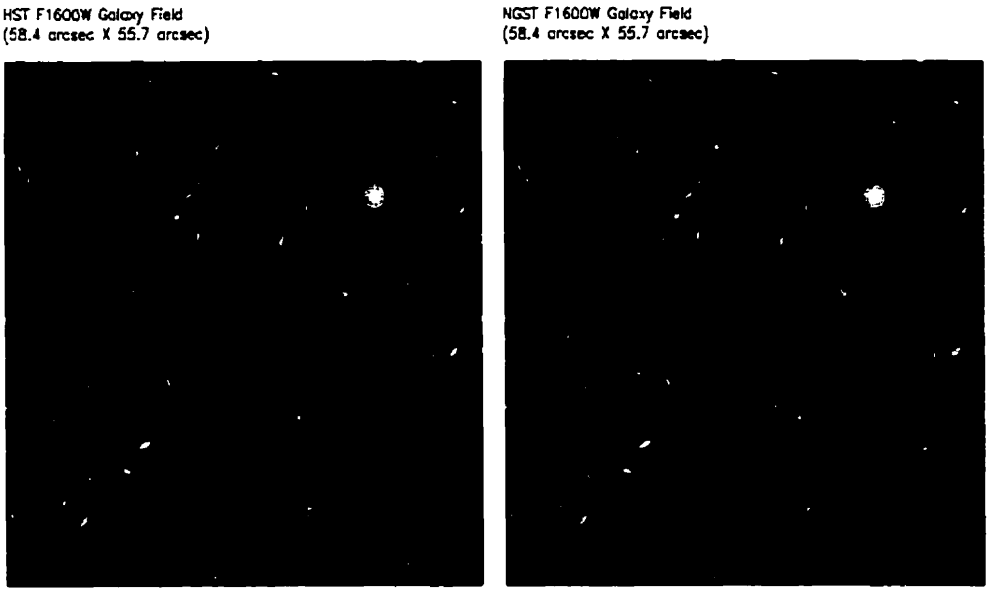

Figure 3.10: An artificial deep NGST galaxy field (right) based on extrapolation of HST data (left). In order to account for the higher spatial resolution of the NGST the original images of galaxies have been replaced with greatly oversampled artificial ones with the same physical parameters.

(according to a normal distribution with a specified correlation length - see Equation 2.9) next to randomly chosen original galaxies. This simulates the projected spatial clumpiness of a real distribution. The simulation actually puts several clones back in the field for each faint galaxy to mimic the steep increase in source counts at these magnitudes. The background is calculated using a model that includes a scattered and thermal component of the zodiacal light (Morris 1999). In this simulation, however, the scattered component is multiplied by the observed NIR solar spectrum to simulate the effects of solar absorption features.

The simulation has some difficulty with overlapping galaxies. The masks

used to separate galaxies are circular and the galaxies can have very small separations. In the case of extreme overlap, the average magnitude is used in the updated catalog. The spectral types may be mixed under these circumstances. That is, a portion of a galaxy might have an SED that is intermediate to the different overlapping types.

The artificial star fields are generated in a similar manner to the galaxy fields. Photometry was carried out in a deep HST WFPC2 field in M 15 (obtained from the CADC HST data archive). Published HST WFPC2 photometry of NGC 6397 (King et al. 1998) was used to make template colour-magnitude diagrams for the main sequence and white-dwarf sequence and provide the colour information for the different filters in the simulation. Each star in the original HST field is replaced with a NGST PSF (to be determined later) with the same brightness. As with the galaxy simulation, for each star fainter than a given magnitude several clones are placed in the NGST field within a correlation length of other stars. The net effect is a field with the correct number counts and the same spatial distribution function as the original HST field. The stars in this entire field can be shifted fainter and made more dense to simulate their appearance at an extragalactic distance. Furthermore, they can be superimposed on a galactic background (a scaled archival HST WFPC2 image of NGC 5457) of a given surface brightness.

3.2.2 Virtual Next-Generation Space Telescope

The instrumental PSF used in the earlier MOS simulations was a Gaussian with a FWHM given by the diffraction limit of the telescope. This was improved for the VI study by forming a high resolution mask of the NGST pupil

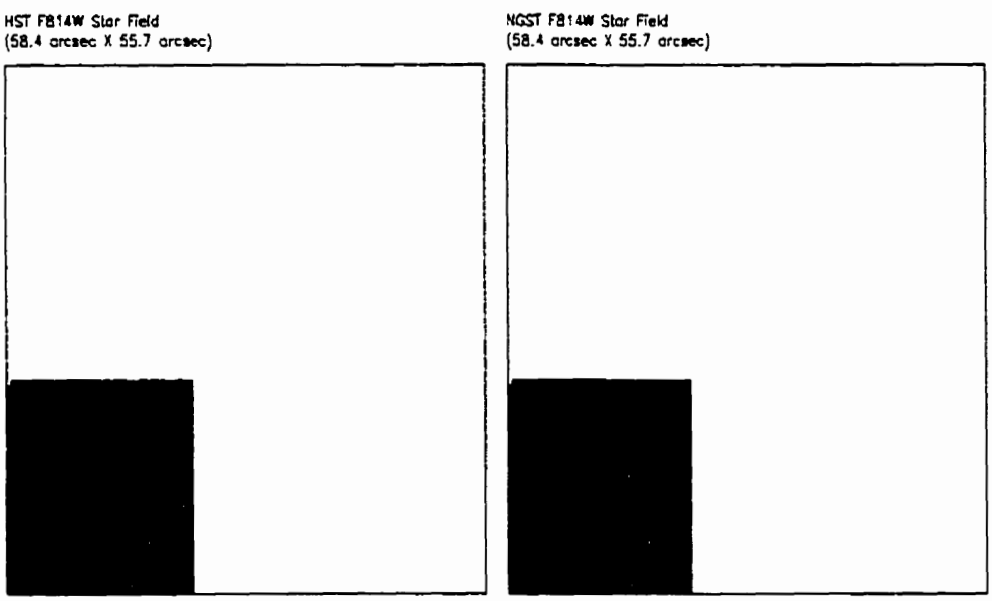

Figure 3.11: An artificial deep NGST globular-cluster field (right) based on the extrapolation of HST data (left).

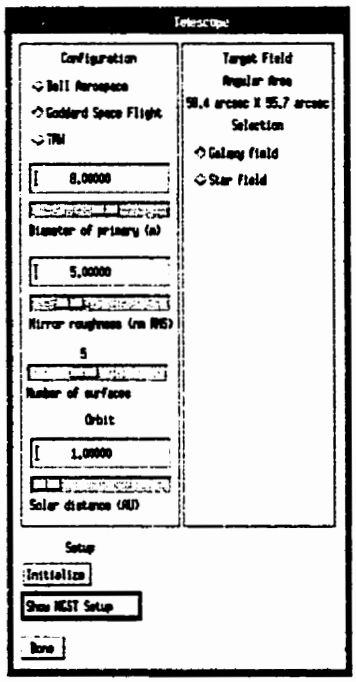

Figure 3.12: The control interface for the NGST.

(for the three proposed observatory designs) and taking the Fourier transform. Morbey (1999) suggests that the Strehl reduction for wavelengths shortward of 1.0 micron for NGST is reasonably well described by the scattering law in Equation 2.12. This law is applied to the diffraction pattern of the NGST to achieve the telescope PSF at the focal plane. The telescope throughput - including the number of gold surfaces - is also calculated.

3.2.3 Virtual Imagers

The VI and NIR camera filters are simulated with specified efficiency curves and correspond to the HST WFPC2 and NICMOS filters. The detectors are also simulated and include size, pixel scale, well depth, gain, quantum

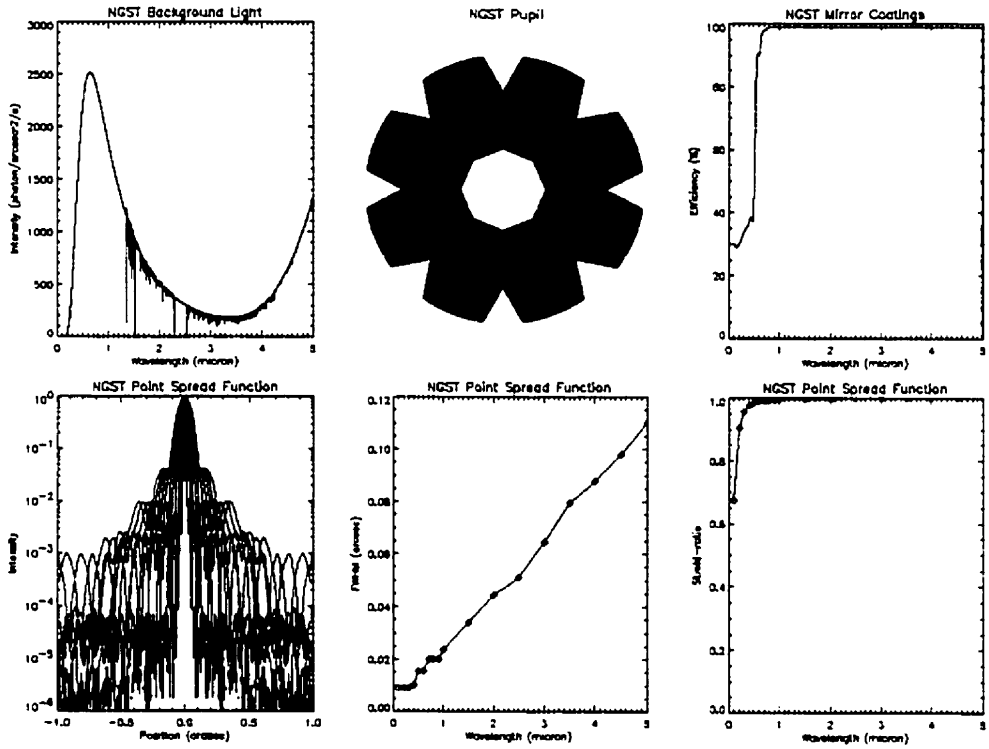

Figure 3.13: A display of various parameters for the NGST.

efficiency, dark current, and readout noise as variable parameters. The user can select a particular $4.0'' \times 4.0''$ galaxy or star field for study from the artificial NGST deep fields and perform broadband imaging on it. The exposure duration and number of co-adds can be specified. Given the user-inputs for detector type, size, pixel scale, etc., the simulation outputs what the imagers would record - including Poisson noise - on the detector. Three main types of detector - indium-antimonide (InSb), mercury-cadmium-telluride (HgCdTe), and hybrid visible silicon (HyViSi) devices - are available. The simulation performs automated data reduction and photometry. Diagnostic numbers are output, such as the magnitude, radius, and B/T of the galaxy. In the case of star fields the colour-magnitude diagrams are output for a given choice of filters.

3.2.4 Virtual Multi-Object Spectrograph

Improvements to the original artificial NIR imager and spectrograph were made. The filters and gratings are simulated with specified efficiency curves. The detector is also simulated and permits the specification of size, pixel scale, well depth, gain, quantum efficiency, dark current, and readout noise. The user can select a particular galaxy for study from the resulting artificial NGST deep field and perform direct imaging or spectroscopy on it. The slit size, grating resolution, and exposure duration can be manipulated. Given the user-inputs for detector type, size, pixel scale, etc., the simulation outputs what the imager or spectrograph would record - including Poisson noise - on the detector. Here, the choice of detector is either an InSb or HgCdTe device. The user can prescribe a region for spectral extraction. The sim-

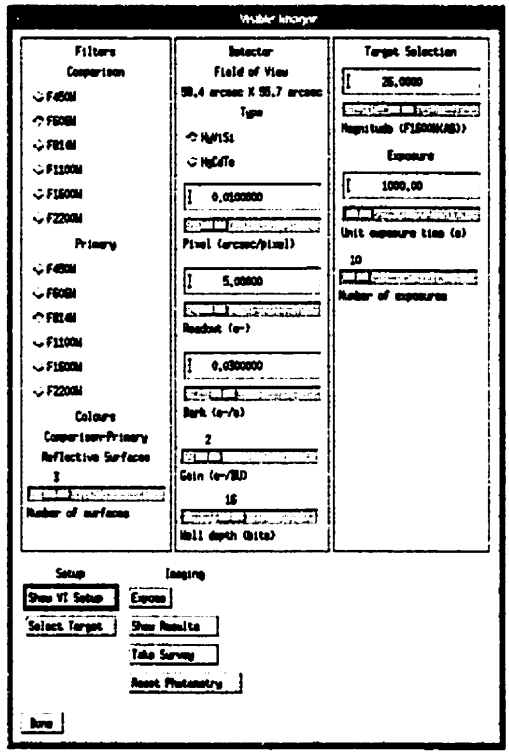

Figure 3.14: The control interface for the VI. Broadband imaging with an optical detector can be carried out using a variety of filters.

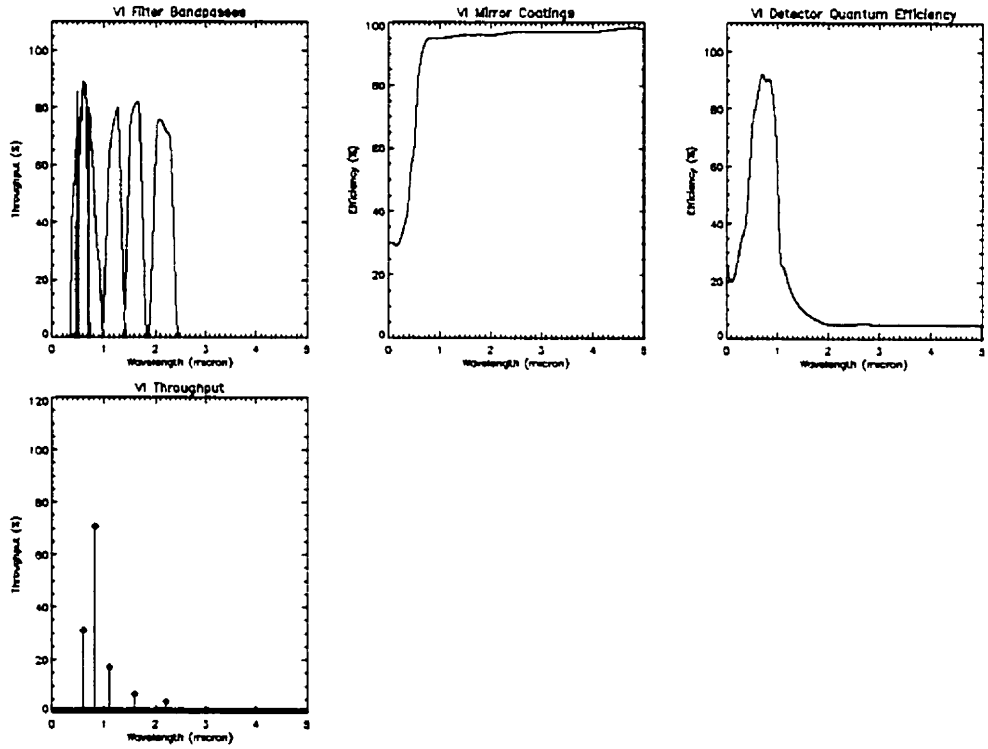

Figure 3.15: A display of various parameters for the VI.

ulation performs automated data reduction and extracts the spectrum. It does this by taking a simulated integration of the background (without *any* galaxies) of the same duration and with the same slit as with the observation of the galaxy. It then subtracts the background. Diagnostic numbers are then also output, such as the H-band magnitude and radius of the galaxy as well as S/N and resolution of the extracted spectra.

The Canadian design for the MOS included an integral field unit (IFU) employing an image slicer (Crampton et al. 1999) and, for completeness, I devised a means of simulating this as well. This is achieved by scanning across an approximately $2.0'' \times 4.0''$ region centred on the selected galaxy and performing slit-spectroscopy as described in Section 3.2 at, say, 20 positions. The resulting spectra are reformatted to a single slit and recorded by the detector. Also recorded is the region covered by spectra on the detector - the footprint - which provides statistics on the efficiency of detector coverage.

Finally, a multiplexing mode was included. The number and size of spectrograph slits can be specified and they are placed on galaxies of a given magnitude selected at random. Four different focal plane mask configurations are simulated. These are a micro-mirror mask (as in MacKenty 1999), a reconfigurable fibre-fed system, a slit-mask composed of sliding bands, and a micro-machined shutter mask. The latter three are comparable to those described in the Canadian NGST MOS studies (Crampton et al. 1999). The simulation operates by 'blocking out' regions of the focal plane of the different mask configurations as each available position is used. As in the image-slicing mode, the resulting spectra on the detector and their footprints are recorded. The four different mask types can be compared directly based on field and

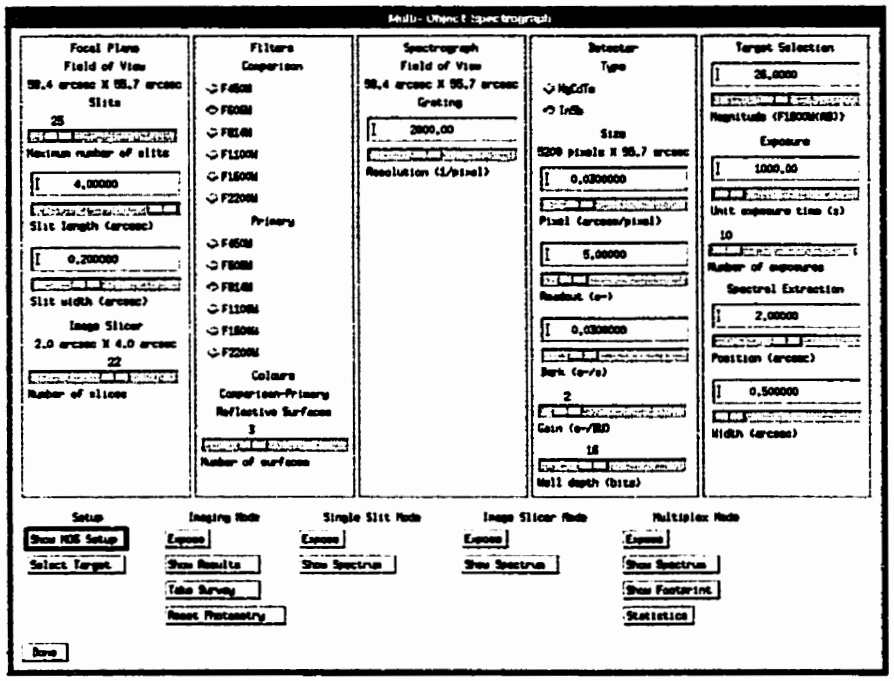

Figure 3.16: The control interface for the MOS. Broadband imaging with a NIR detector can be carried out using a variety of filters. Spectroscopy can be performed using a single slit, an image-slicer, or different multi-plexing arrangements.

detector coverage.

3.2.5 Virtual Deep Surveys

An important aspect of this new software is that the user can apply all of the simulated instruments to the observation of any galaxy or star in the artificial fields. The artificial deep fields, telescope, and instruments are all integrated into a virtual observatory called NGST VI/MOS. User-friendly interfaces written in IDL allow for the prescription of deep-field characteristics and the specifications for the telescope and instruments. Afterwards, the user

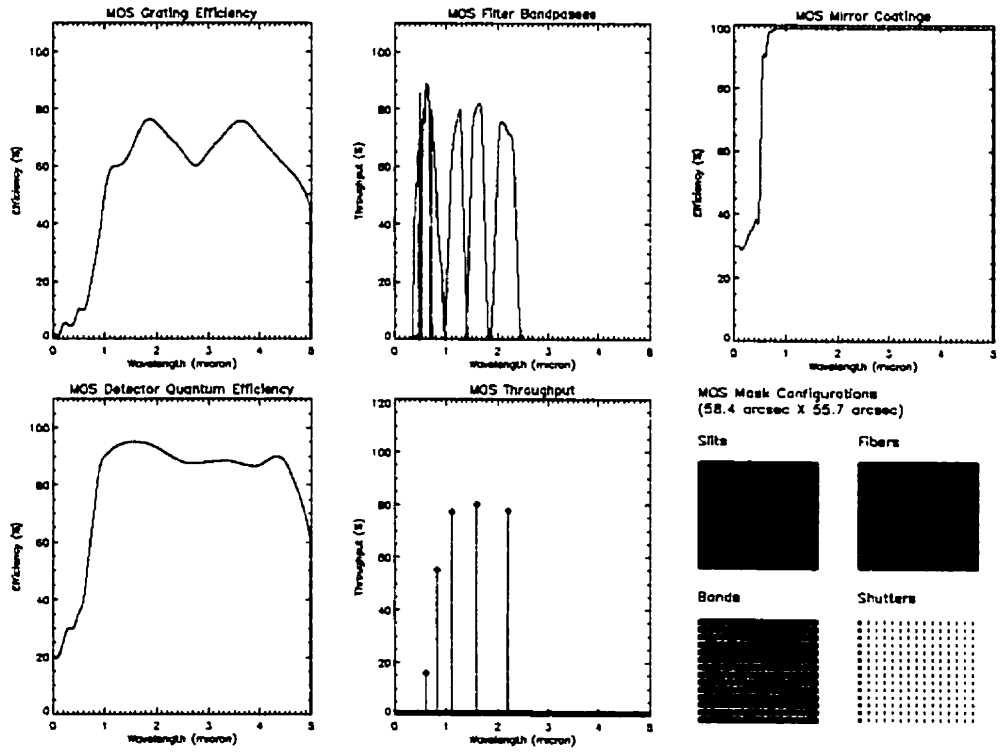

Figure 3.17: A display of various parameters for the MOS.

can 'point' the telescope at either the deep galaxy or star field and select a particular object for study.

The following example suggests some of the advantages of this design. The user could select, say, an $z = 4$ Scd galaxy and perform deep broadband imaging with the VI through an R filter. The same target could then be imaged with the MOS using an H filter and a deeper exposure. Will the star-formation regions still be visible with the poorer pixel sampling and a HgCdTe detector? Perhaps this should be followed up with deep $R = 1000$ spectroscopy using a $0.05'' \times 4.0''$ slit. Maybe it would be best to use a bigger slit to let in more light. Why not try the IFU on the same field? All of these observations can be performed quickly with simulated images or spectra appearing on a display. The photometry and spectral extraction are all done automatically. The program also automatically returns the B/T and S/N per pixel of galaxies as well as the colour-magnitude diagram when star-fields are observed.

Alternatively, the user can allow the telescope to perform an automated survey of either a galaxy or star field. The user can specify filters, grating, slit-size, and a brightness selection criterion. The telescope will randomly select objects, observe, and record the results. The software can display the configuration of the MOS slit-mask used in the survey as well as how efficiently the detector was covered with spectra.

A web-based version of the software is available. It gives a simplified version of the IDL interface which demonstrates the results of deep imaging and spectroscopy with NGST in the Hubble Deep Field South (see http://astrowww.phys.uvic.ca/~steinb/).

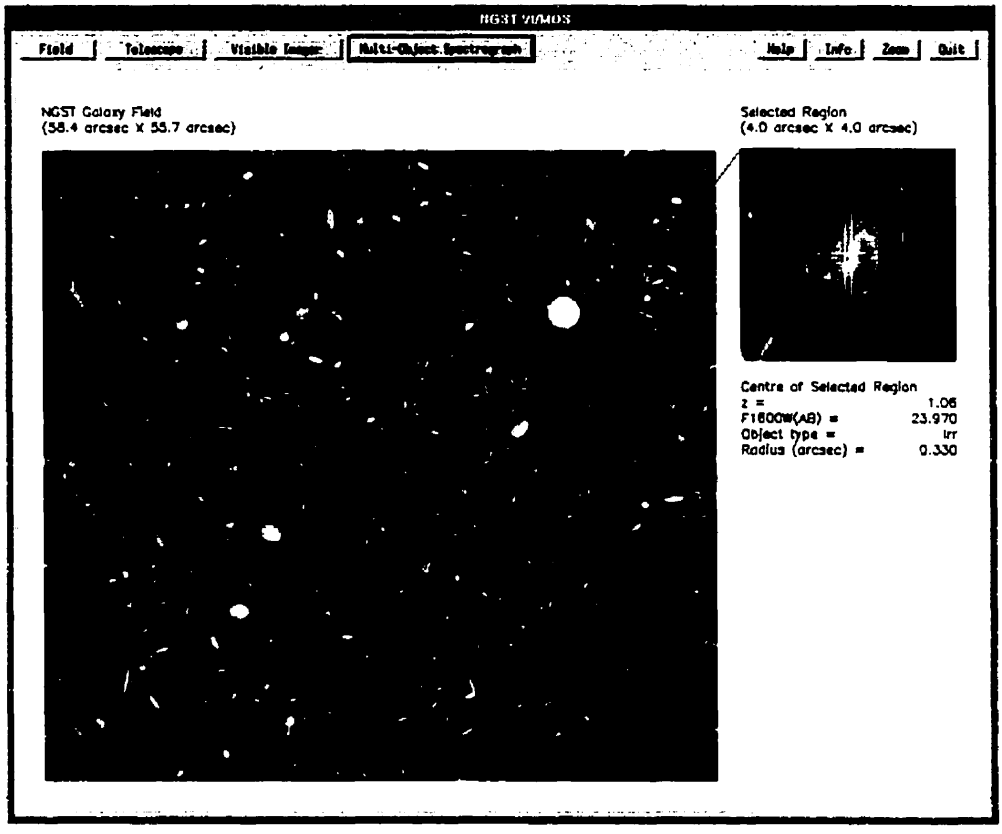

Figure 3.18: The control interface for the NGST VI/MOS software. The user can 'point the telescope' and apply any of the simulated instruments to the observation of any galaxy in the artificial field. Alternatively, the telescope can be run in a survey mode and perform data reductions automatically.

3.3 Imaging with the Adaptive Optics Bonnette

A natural guide-star AO system on a large astronomical telescope can render diffraction-limited images of faint targets of resolution similar to a space-based telescope (see Rigaut et al. 1998 for a discussion of AOB). In some respects the observing procedures are similar (at least for imaging). The telescope is aimed at a target position and many exposures are taken, often at several slightly different telescope pointings. This dithering of exposures is done to remove the effects of cosmic ray strikes and improve the flat-fielding of the detector.

There are, however, some distinct challenges for AO observations in general, and the CFHT AOB in particular, especially if it is hoped that they can be competitive with the HST. It should also be stressed that all of the observations discussed here are *pioneering* ones. When I first observed with AOB in June 1996 there was little experience in AO observing techniques and essentially no experience in very deep observations (ones that cover hours of observing time per target) to draw on (a review of AO observing progress to 1996 can be found in Tessier 1996). I have found that good observing technique and image-processing methods can help to overcome the challenge of being competitive with HST.

Only objects that are sufficiently near an adequately bright star are possible targets. For a space-based observation the isoplanatic patch is effectively the entire field of view (FOV). This is not true for an AOB observation and it is very important how far offset the target is from the guide-star. This offset must be less than approximately 30″ and this strong restriction is a

new one for ground-based imaging. Also, this bright star cannot be allowed to saturate the images badly.

Another obvious difference with space-based imaging is the background light. From space most of the background light is from the zodiacal light of the solar system (light scattered and re-emitted from dust in the ecliptic plane), some light scattered from the atmosphere (in the case of Earth orbit) and from the spacecraft itself. This background presents a problem for removal during processing of the images but it is not as variable or as bright as the background presented to a telescope on the ground. This is a particular problem for NIR observations with AOB. For deep observations, flat-fields generated from observations of the illuminated inside of the telescope dome (dome-flats) are inadequate to correct for the sensitivity variations across the detector. It is much better to use observations of the sky (of the same exposure duration as those on the target) to account for the slight non-linearity of the detector and the colour of the sky in the observations. It is even better to use the target exposures themselves to generate the flat-field since it accounts for the quickly changing sky-brightness. But since there is probably a bright star in the field this is a difficult procedure. We might point the telescope in such a way as to omit this bright star from the field but that is not wise either. Bright stars are valuable in determining the PSF in the field.

Deep imaging of faint objects with AO requires that we juggle several - often competitive - goals. We want to choose targets close to a bright guide-star yet not saturate the image with the light from it. Also, individual exposures need to be long to accumulate enough flux to see the faint object yet short enough to follow the varying sky brightness. Finally, we must

obtain information that can describe the PSF near the target observation. The image of the guide-star might be sufficient if it is close enough to the target but this is usually not the case. An offset of 10″ to 20″ is sufficient to render this information inadequate and, therefore, a means of determining the PSF at the target position is necessary.

3.3.1 Target Selection and Imaging Methods

Selecting possible targets for the AOB demands that an $R < 15$ guide-star be nearby on the sky. This condition was determined from experience during the commissioning phase for the AOB in June of 1996. The magnitude of 15 was obtained by trial and error; magnitudes fainter than this were insufficient to run the AOB WFS reliably. If the natural seeing became worse than about 1.0″ FWHM while using a fainter guide-star the corrected on-axis PSF was not better than 0.3″ FWHM.

For the purposes of the science observations discussed here the most important aspect was to maintain a small FWHM. It can be seen in Figure 3.19 that the Strehl-ratio falls off fairly quickly with offset. These data were obtained during the AOB commissioning phase in 1996 and are the measurements of individual bright stars in a mosaiced observation of M 5 (they will be discussed in more depth in Section 5.2). This drop in Strehl ratio might be a concern for spectroscopy where putting the most flux through a small slit is paramount. For imaging, however, the real concern is maintaining a good FWHM and we can see from Figure 3.20 that for AOB the FWHM falls off more slowly with offset. Thus, any target within about 45″ of a guide-star brighter than $R = 15$ is possible. Brighter guide-stars that are

closer are, of course, better.

In order to obtain lists of possible targets with these conditions I adopted the following method. First, the list of all the objects of interest with their coordinates on the sky was compiled. Then, only those targets visible from the CFHT (latitude of about 20 degrees north) were considered. However, this is a less stringent condition then that imposed by the AOB operation limits. Operating on a guide-star further than 45 degrees from the zenith was found to be difficult to maintain. This is probably due to a combination of factors. The line of sight passes through an increasing thickness of air near the horizon, which reduces transparency and increases turbulent effects. In any event, it was taken as an empirical fact that operation on guide-stars with declinations below -25 degrees and above 65 degrees north and either 3 hours ahead of or behind the meridian was not possible. Of those objects, the next selection criterion was whether the target had an $R = 15$ star within 45″ on the sky. This was accomplished by entering the coordinates of the list of possible targets into the United States Naval Observatory (USNO) Guide-Star Catalog (GSC) using the internet interface and requesting a list of all stars in the database within 45″ offset. The USNO catalog was used because it is the most complete star catalog down to magnitudes of about $R = 16$. This selection criterion was always found to be the most stringent and was met, typically, by only 1-5% of objects from any list of targets.

In real observations it was found that an $R = 15$ guide-star was sufficient for targets with offsets of 45″ as long as the natural seeing was approximately 0.8″ FWHM or better. This would, for example, provide a 0.2″ FWHM corrected PSF at 20″ offset in H. But if the seeing were to degrade to 1.0″

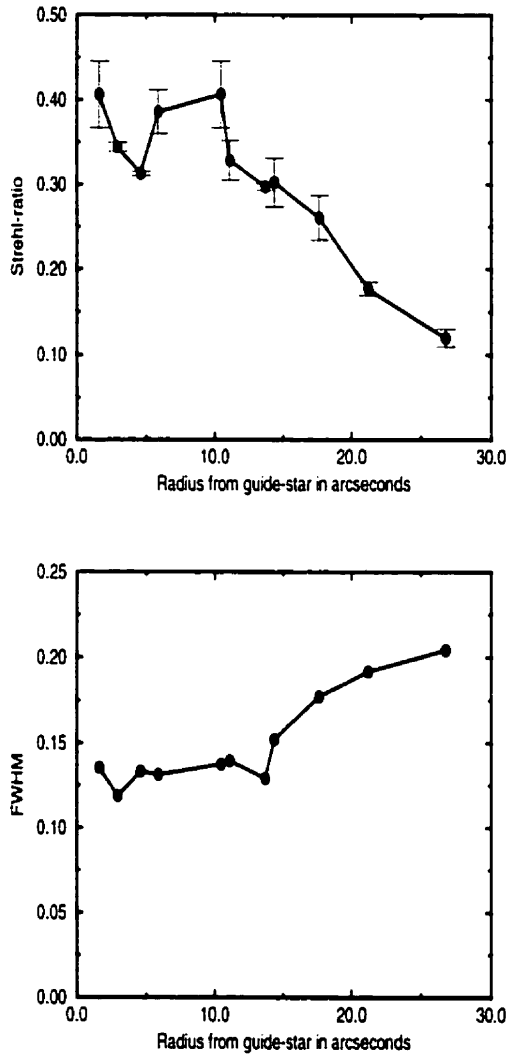

Figure 3.19: Plots of PSF Strehl-ratio and FWHM as a function of telescope offset for CFHT AOB.

FWHM or worse the corrected PSF at that point would surely be worse than 0.5″ FWHM. Since, often, our targets were at offsets of 20″ or more this was not ideal. To achieve this result why not simply observe them without AO during good seeing conditions?

Since it was noted that the natural seeing could often degrade beyond 0.8″ FWHM over the course of a few hours (the typical duration of an observing session for a faint target) observation with an $R = 15$ guide-star was often not satisfactory. The ideal target possessed a guide-star of $R = 12$ or better within 20″ offset. It was found that for those stars the correction would always be 0.2″ FWHM or better at the target position. Thus, an observing strategy must attempt to balance the need to observe all required targets while considering the possibility that seeing conditions might change. For AO observations, learning the art of coordinating seeing conditions with the available targets is a difficult but necessary task.

Once a target was selected, observations with AOB began by first pointing the telescope at the guide-star. Typically, a few observations with the camera through an H filter were made to ensure that the telescope and AOB were aligned, that the AOB was operating properly, and that the on-axis PSF was at least sharper than 0.2″ FWHM. Then the telescope was offset to the science position by using the AOB interface provided for that purpose. The AOB handles internally the maintenance of guiding without effort by the observer. Sometimes, if the guide-star was faint, the guiding would be lost. This was indicated by a drop in flux on the WFS which is registered on a display on the AOB interface.

Individual integrations of 5-20 minutes were obtained in a dither of offsets

of a few arcseconds. This was found to be sufficient to eliminate cosmic ray strikes and stars and provided for the generation of flat-fields from the images. Usually the H filter, which provided the best compromise between low sky-brightness and quality of PSF, was used. Some J and K-band observations were also obtained but it was found that it was best to wait for good seeing conditions (better than 0.7″ FWHM) to observe in J since AO correction is worse for shorter wavelengths (see Section 2.3.1). The sky is about 5-10 times brighter in K-band and it was found that shorter exposures were advisable here in order to track the variation in sky-brightness.

Observations of NIR standard stars from the United Kingdom Infrared Telescope (UKIRT) catalog were made in order to make photometric calibrations. This catalog of standard stars is useful in two ways because they are of a brightness similar to the guide-stars used by the AOB. Since these were, typically, the first observations made during the night they provided a check that the AOB was operating properly. Secondly, they provided the photometry necessary to calibrate the target observations. The stars in the catalog have established J, H, and K fluxes. In order to find the flux of a given target the zero-point magnitude of the calibration star was found first.

Only one other standard NIR-detector correction was necessary. This was to obtain an exposure of the same duration without exposing the camera to light in order to determine the counts due to thermal energy in the camera itself. This dark-field was subtracted from all other images.

3.3.2 Point-Spread Function Calibration

When faint objects are observed with AOB the guide-star is usually offset from the science target. For the the 1024×1024 pixel infrared camera (KIR) at least, the guide-star is often within the FOV ($36'' \times 36''$) of the detector. This has advantages and disadvantages. First of all, it ensures that a bright star will be available to characterize the on-axis PSF. Unfortunately, target integrations are typically very long (5-20 minutes in duration) and will probably leave a saturated image of the star. This might mean that several very short calibration exposures (1-30 seconds in duration) might be interleaved with those observations and averaged to obtain an unsaturated image of the star to characterize the PSF. Otherwise, the on-axis PSF can be obtained using the wavefront reconstruction technique of Véran et al. (1996). This produces essentially the same information as would be obtained if an image of the guide-star were made using the camera itself.

Even so, this will not give the PSF at the target position and in response to a need to obtain reliable PSFs for the processing of images from the AOB QSO host study (Hutchings et al. 1998) I developed a means of providing this information using calibration observations of dense star-fields. This work was carried out from June 1996 to June 1997. I am not aware of any other method to determine off-axis AO PSFs in this semi-empirical manner. The user must obtain observations of a dense star-field each night; the core of a globular cluster works best. The AOB is guided on a star of similar brightness to the one used in the target observations. It is likely that the required PSF is at an off-axis position outside the FOV of the camera, so a mosaic of the star-field is generated by repositioning the telescope. The goal is to

obtain an unsaturated image of the guide-star as well as a roughly uniform distribution of stars at many off-axis positions. Now, although the guide-star in the star-field calibration image is similar in brightness to the one used in the target observation it is very unlikely that the delivered PSF is identical. The natural seeing will likely be different with, say, 0.5″ FWHM in one and 1.0″ FWHM in another. This might give delivered PSFs of 0.10″ FWHM and 0.15″ FWHM respectively. Thus, my PSF reconstruction technique folds in information about the on-axis PSF during the science observation with the star-field mosaic data.

3.3.3 Image Flat-Fielding Issues

Since the targets were faint the imaging discussed here necessarily involved long integrations. It proved impossible to correct for the pixel-to-pixel variations in sensitivity of the detector for those exposures using dome-flats. Both the Montreal Near-Infrared Camera (MONICA) and KIR have relatively smooth linear responses to increasing signal but dome-flats of the same median flux as the observations did not flat-field the images properly. The reason is likely that the colour of the inside of the telescope dome is not at all like that of the night sky. It was found that only images of the night sky taken during the time of the observations were adequate to generate a flat-field. Unfortunately, with observing time at a premium it would have been too costly to make dedicated observations of the sky in all filters during the observing run.

I developed a technique to generate flat-fields from the observations themselves. The problem was that there were typically several faint stars

and a *severely* overexposed guide-star in the images. Generating flat-fields from images of the night sky containing stars is a standard image processing technique. The difference here is the small FOV and high percentage of saturated pixels in each of the frames. Perhaps 20% of the pixels in each of the frames would have significant signal in them from stars and would need to be excluded from the calculations. With few images with which calculate a median value a good method of determining which pixels to exclude was required.

3.4 Image Processing Tools for the Adaptive Optics Bonnette

There are several factors that make the reduction of AO observations challenging and unique. The variable AO PSF makes the analysis of images difficult. The necessity of a bright nearby guide-star means that a bright object is often in the FOV. Typically it is many times brighter than the object of interest. Compounding these problems is that the detector used in the observations is not generally a CCD. Observations are often made with NIR detectors which have small FOV, nonlinearities, and problems with persistence. I developed the software package AOTOOLS for the Image Reduction and Analysis Facility (IRAF) environment in order to assist in the reduction of AO imaging observations and, specifically, those obtained with the CFHT AOB. It is intended to act as a data-reduction pipeline for AO observations.

First of all, since AO observations are often carried out in the NIR, the challenge of using NIR detectors is an issue. These first and second generation detectors typically have a large number of non-linear pixels. The

task BADPIXEL generates a bad-pixel mask. Once one is obtained, the user might still need to deal with persistent signal in the images. Near-infrared detectors typically have a readout architecture with four separate quadrants. If persistent signal (video noise) is a problem, the task PERSISTENCE can be used to subtract it. The user will still need to know how to mosaic the images back together. Since NIR detectors are still physically fairly small and the AO fields that they survey also small it is possible that there are no bright stars that are coincident in all frames in the mosaic. Thus it may be difficult to find the sky-coordinates of the centre of the frames. The task POSITION uses a coordinate transformation derived from the AO-system WFS position to determine the centre of the field for a list of images.

The sky is brighter in the H-band than in the visible, and several times as bright in the K-band. The brightness also changes over the course of minutes. Since NIR detectors, besides having numerous bad pixels are slightly non-linear, using dome-flats or twilight sky-flats to flat-field the images is probably inadequate for very deep imaging. Without dedicated sky observations, generating flat-fields with the images themselves becomes necessary. The task FLATFIELD removes the bright stars from the observations and uses the residual images to generate flat-fields. The task DITHER can then be used to reconstruct the mosaic pattern of the original observations.

With the images processed and mosaiced the user will find that the PSF - if there are enough bright stars in the field to determine it - is variable. Furthermore, the user may not have an observation of the guide-star in order to determine the PSF at all. Since the corrected seeing during the observations has almost certainly varied it is difficult to know the PSF at the target

position. The package DEGRADE solves these problems. If there is only a badly overexposed image of the guide-star ONAXIS can be used to generate a PSF for on-axis in the mosaic using other observations of the guide-star, that are not overexposed. This will still not give the PSF everywhere in the field, however. Using a calibration observation of a dense star-field, OFFAXIS can determine the PSF in the rest of the target field.

With processed fields and an accurate PSF in hand all that remains is to determine if the observations are resolved. The task PROFILE provides a simplified way of comparing the profile of the PSF and the observation of, say, a galaxy. It generates the elliptic-isophotal profile of the object and can be rerun to determine the model fit and then run one last time on the PSF profile to determine if the object was resolved.

Each of the tasks within the AOTOOLS package is now described in more detail. In most cases these new IRAF tasks use pre-existing IRAF subroutines to do many of the calculations. I designed them this way to facilitate quick implementation of the software. The nature of each task is unique to either AO imaging in general or to the CFHT AOB with MONICA or KIR in particular.

3.4.1 Generating Bad Pixel Maps

The task BADPIXEL is designed to determine over-sensitive, under-sensitive, or dead pixels. A flat-field is median-filtered to smooth out these non-linear pixels. Then the original flat-field is divided by this smoothed image. Any pixels at a given sigma-level above and below the median signal-level are recorded. This sigma-level has been specifically tuned (by trial and error)

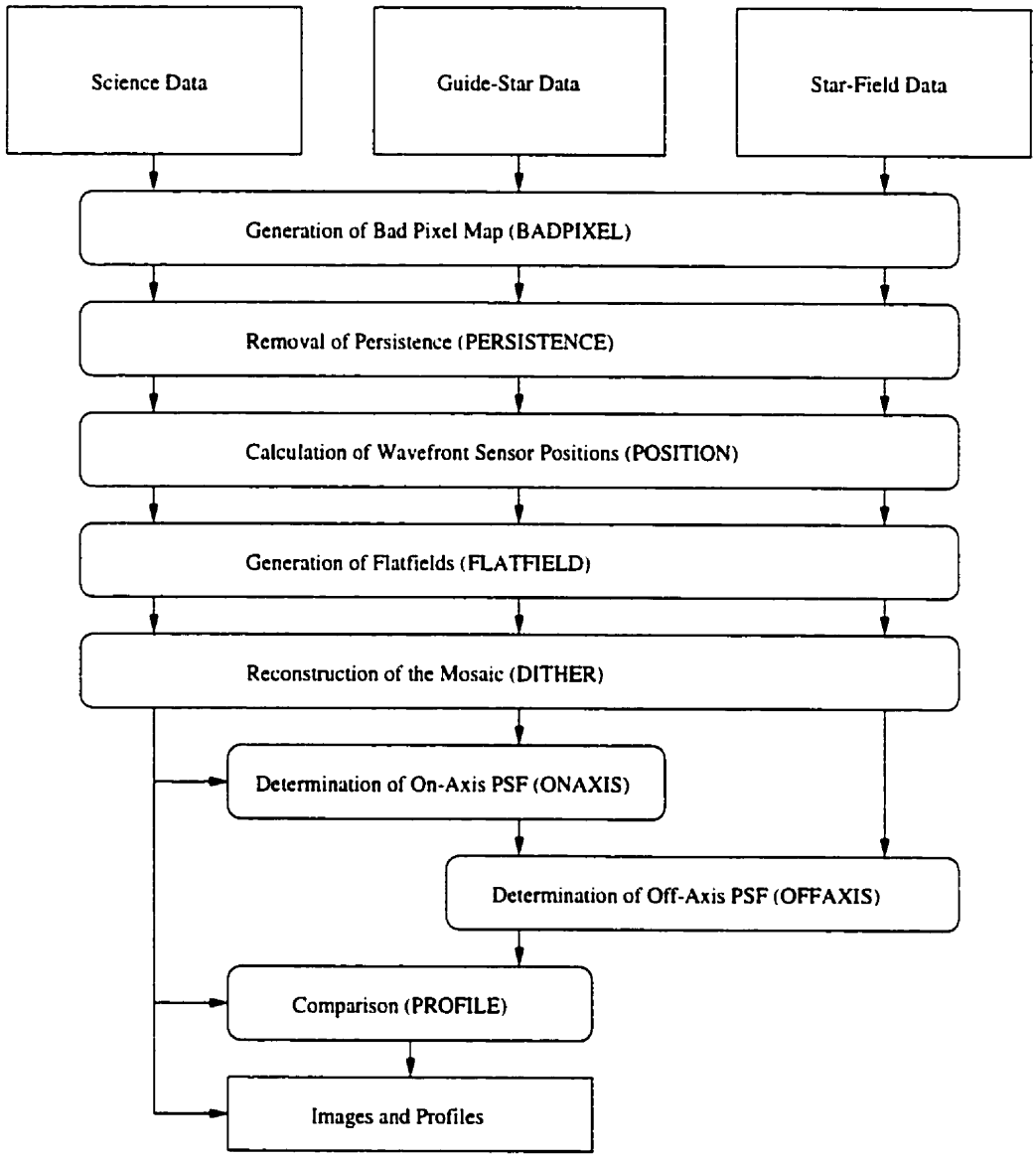

Figure 3.20: The AOTOOLS software architecture. This IRAF package provides a complete image processing pipeline for CFHT AOB observations.

```
                    Image Reduction and Analysis Facility
PACKAGE = aotools
   TASK = badpixel

(infile = ▌          flatfield) input flat-field
(smooth =                 yes) smooth the image?
(box    =                  20) size of smoothing box
(funfit =                  no) fit with a function?
(size   =                   0) include how many pixels surrounding a bad one?
(order  =                  3.) order of sigma-clipping
(list   =                   )
(mode   =                   q)
```

Figure 3.21: The AOTOOLS BADPIXEL interface.

for MONICA and KIR to detect the greatest number of non-linear pixels without including adjacent linear pixels. It then outputs a map of these pixels with unit value for all nonlinear pixels. In effect, it takes an input median flat and outputs a bad-pixel map for the detector.

3.4.2 Removing Persistent Signal

Video noise is a problem for the MONICA detector and needs to be subtracted. This is because, although persistent, the spatial structure of the signal changes during observations of a single target object (say, over the course of 30 minutes). The task PERSISTENCE subtracts persistent signal from NIR detectors and was specifically designed for the MONICA detector. The program simply median-smooths the raw image to generate an image of the persistent signal and then subtracts it. However, the MONICA readout architecture of four independent quadrants is exploited to improve the result. The persistent signal has the same structure in each of the four quadrants and the software can be set to use, say, only one or two of the quadrants to perform this task if a bright star is located in one of the other quadrants. In

```
                    Image Reduction and Analysis Facility
PACKAGE = aotools
   TASK = persistence

(infile = ▌                image) input image
(quad1  =                    yes) use quadrant 1 in pattern construction?
(quad2  =                    yes) use quadrant 2 in pattern construction?
(quad3  =                    yes) use quadrant 3 in pattern construction?
(quad4  =                    yes) use quadrant 4 in pattern construction?
(mode   =                      q)
```

Figure 3.22: The AOTOOLS PERSISTENCE interface.

this way, the image of the persistent signal is generated without corruption by signal from a star.

3.4.3 Registration of Images

The task POSITION gives the pixel coordinates relative to the guide-star position for a target observation. That is, it gives the coordinates of the centre of the frame for all frames in a set of observations.

During imaging with either MONICA or KIR the AOB WFS pick-off mirror position is written to the file containing the image. A dithered set of images of a bright star provides a calibration between detector and WFS position. Correlation of the star and WFS positions gives a transformation for how many pixels on the detector corresponds to a given offset with the WFS pick-off mirror. The program POSITION is given an image of the guide-star and thus can determine the position of any other frame from the WFS position information contained in that file.

```
                    Image Reduction and Analysis Facility
PACKAGE = aotools
   TASK = position

(trans_a=                  ) matrix (1,1) in arcseconds per step
(trans_b=                  ) matrix (1,2) in arcseconds per step
(trans_c=                  ) matrix (2,1) in arcseconds per step
(trans_d=                  ) matrix (2,2) in arcseconds per step
(wfsx_c =                  ) x-axis sensor offset in steps
(wfsy_c =                  ) y-axis sensor offset in steps
(format =                256) camera format in pixels
(scale  =              0.045) pixel-scale in arcseconds per pixel
(calibra=        calibration) file of input to generate a transformation
(guide  =              guide) guide image
(inlist =             inlist) file of images for which to return offsets
(outlist=            outlist) file containing output list of image offsets
(calcula=                yes) calculate a transformation matrix
(corr_of=                yes) output p.a. and target distance in arcsec
(archive=                   )
(mode   =                  q)
```

Figure 3.23: The AOTOOLS POSITION interface.

3.4.4 Generating Flat-Fields

The task FLATFIELD is designed to output flat-fields based on exposures with bright stars. This is particularly useful for AO observations in the NIR when sky-levels change quickly and bright stars are almost always in the field. The user inputs the list of raw images and their location as well as a location on hard-disk to store the flats. The explicit specification of directories is helpful in maintaining libraries of images and flats on separate disks. This is useful because the program is able to make flat-fields using all of the exposures in, say, a entire run's observations. With larger format detectors this can occupy considerable disk space.

The goal is to extract the bright stars from the individual images and then use these corrected images to generate flat-fields. First, a crude flat-field using all the images through a given filter for a particular target is made. That is, all of those images are median-combined. These images were

probably taken over the course of several hours and consist of, perhaps, a dozen images through a given filter. They would have all been taken at slightly different telescope pointings and, thus, a median (or average) would not suffer as badly from bright pixels under the stars. This would still be inadequate to flat-field the observations. It would be sufficient only as a first-guess for the original dozen images. Thus, after flat-fielding, a simple sigma-level clipping algorithm is used to generate a map of where all the pixels corrupted by stars are located. By omitting these pixels before median-combining all the raw images again, a better quality flat-field is generated.

It was found that an improvement to the method was to subdivide the list of images based on the sky-brightness in each. That is, if the flat-field for each image is generated from images of similar sky-brightness the net result was improved. This is due to the more efficient tracking of the sky-brightness it affords.

Generally, the best way to use this task is to include all of the images through a particular filter for observations of one target. The dithering used to obtain these observations is usually adequate to remove the bright stars from the images. A version of this software that allows for more iterations of this process has been developed but generally one iteration achieves the best results anyway. More iterations have a tendency to 'chase' the wings of the AO PSF further and further away from the core. This can result in poor flat-fields.

```
                    Image Reduction and Analysis Facility
PACKAGE = aotools
   TASK = flatfield

(inlist = )             inlist) list of images for which to make flats
(raw    =                 raw) directory where raw images are located
(work   =               Flats) directory for images working space
(dark   =                dark) name of dark-current image

(level  =                  2.) sigma flux-difference limit: selection
(sigma  =                  1.) sigma-clipping limit: mask generation
(grow   =                  10) growing radius for mask generation

(list   =                   )
(mode   =                  q)
```

Figure 3.24: The AOTOOLS FLATFIELD interface.

3.4.5 Reconstructing the Image Mosaic

The task DITHER is designed to reconstruct a mosaic image based on a dithering pattern. It can perform sky-subtraction automatically but is intended to exploit the FLATFIELD task in flat-fielding of images. The user inputs the list of raw images and the coordinate offsets of the individual images and the program automatically outputs the reconstructed dithered mosaic.

In the event that the coordinate offsets of the individual images are not known this task can be used to provide a first-guess. It will perform a simple flat-fielding (using a median of all the frames) from which bright stars can be centroided using the IRAF task IMEXAM to register the images.

3.4.6 Correcting the Point-Spread Function

The task ONAXIS uses several on-axis PSF observations to determine how the PSF changes with natural seeing conditions. It deconvolves on-axis PSFs by ones taken under better seeing conditions (and with guide-stars of similar

```
                    Image Reduction and Analysis Facility
PACKAGE = aotools
   TASK = dither

(inlist = ▌            inlist) list of raw-images
(work   =              work) directory for images working space
(flats  =              flats) directory where multiple flats are located

(offset =           offsets) list of dither offsets in pixels
(badima=           badpixel) name of bad-pixel image
(darkima=              dark) name of dark-current image
(flatima=         flatfield) name of single input flat-field

(trimima=             [*,*]) trim section of image
(statima=             [*,*]) stats section of image for sky
(combima=           overlap) stats section of images for combining

(outsky =               sky) name of output sky image
(outimag=             image) name of output image

(skysub =                no) perform sky-subtraction
(flatfie=                no) perform flat-fielding with single flat
(superfl=               yes) perform flat-fielding with multiple flats
(smooth =                no) make a set of smoothed images
(image  =               yes) output a final image

(list   =                 )
(mode   =                 q)
```

Figure 3.25: The AOTOOLS DITHER interface.

brightness). An interpolation function that scales with seeing is developed in this way. For example, an interpolation function could be generated by using one on-axis PSF image taken under $\sim$ 1.0″ FWHM and one under $\sim$ 0.6″ FWHM seeing conditions. Thus, a single function is generated that produces the result expected for approximately 1.0″ FWHM seeing when convolved with an image taken during approximately 0.6″ FWHM seeing. Of course, this range could also be broken up into smaller increments and, ideally, it would span a range of seeing experienced during a particular series of exposures of interest.

The program then reads in the on-axis PSF image taken near in time to the target observations. It corrects this observed PSF to the seeing conditions during the target exposures. Because the difference in seeing between PSF and target observations is ideally small - potentially the FWHM of the interpolation function could be less than one pixel - the program does not use it directly. The program first deconvolves the on-axis PSF with the interpolation function to simulate better seeing and then operates on this image, using a function of incrementally larger FWHM until the correct PSF is generated. The best PSF is determined by performing a least-squares fit between the wings of the (usually overexposed) guide-star in the observation and a truncated image of the corrected on-axis PSF. The program then outputs the best fitting on-axis PSF for the target observation.

Of course, all the images should be taken in the same waveband. Also, the program can be run without any special processing of the frames. It requires only flat-fielded (and bias subtracted) frames. The user does not need to normalize the brightnesses of stars. The idea is that the user inputs the

```
                    Image Reduction and Analysis Facility
PACKAGE = degrade
   TASK = onaxis

(gain   =                  2.) detector gain in electrons per digital unit
(noise  =                 30.) readout noise in electrons

(infile =                guide) PSF image
(poorona=            guidepoor) guide image with poor seeing
(goodona=            guidegood) guide image with good seeing
(inimage=           imageguide) image of guide wings in target observation
(xsize  =                  100) number of columns in images
(ysize  =                  100) number of lines in images
(skyback=                   0.) background for PSF image in digital units
(skyback=                   0.) background for guide images in digital units
(xguide =                   50) guide column pos in pix for poor seeing
(yguide =                   50) guide lines pos in pix for poor seeing
(exposur=                   1.) ratio of exposures (over- to under-exposed)
(nonline=               20000.) nonlinearity cutoff level in digital units
(fractio=                  0.4) fraction of cutoff for eliminating bloom

(iterati=                   20) number of iterations in correction
(limit  =                   1.) chi-squared limit for deconvolution
(size   =                   3.) FWHM of deconvolution kernel in pixels
(span   =                   3.) span of FWHM in pixels
(modsize=                   3.) FWHM of convolution kernel in pixels

(kernel =                  yes) generate on-axis atmospheric correction
(calcula=                  yes) calculate a range of corrected PSF fits
(fakeit =                  yes) use a gaussian atmospheric profile
(debloom=                  yes) detect and omit bloomed pixels
(model  =                  yes) generate the best-fit image
(interac=                  yes) display results

(archive=                     )
(mode   =                    q)
```

Figure 3.26: The AOTOOLS ONAXIS interface.

raw frames (complete with background flux) in order for the noise statistics to be calculated correctly.

A second task, OFFAXIS, degrades the on-axis PSF to off-axis target location based on a model of anisoplanatism. The calculation of the required correction is obtained in a straightforward manner using an image of a crowded star-field taken under similar conditions.

The program first performs automatic photometry on the star-field. It finds stars in the field using the IRAF task DAOFIND and replaces them with diffraction spikes of the same brightness. The diffraction pattern is an ideal one and is simply the Fourier transform of a circular aperture with a circular central obstruction. It compares peak real-star signals to the diffraction spikes to find Strehl-ratios.

The software will then extract from the star-field an image of the guide-star excluding the wings of any nearby stars. This extraction of the guide-star image is difficult for a crowded field. The program requires a deep image including the faint wings which may stretch out several arcseconds. In order to combat this the wings of all stars other than the guide are subtracted from the raw image prior to extraction. This is done by generating a diffraction pattern for all the stars other than the guide, median smoothing it with a 50 $\times$ 50 pixel kernel, and subtracting this from the raw image. Then the guide-star image is extracted. Extracting the largest possible guide-star image without including any background stars is best. However, even with these precautions the program will still prompt the user to edit out by hand any faint stars remaining (using the IRAF task IMEDIT).

The way to deal with the issue of varying natural seeing conditions is to

deconvolve the image of the crowded star-field with the image of the guide-star in that field. We would expect, if the full image is deconvolved with a sub-image of just the guide-star until the entire flux is contained within one pixel, re-convolution with that same sub-image will reconstitute the original image. That is, the PSF at each of the star positions is restored. Therefore, we should be able to take the deconvolved image of the star-field and convolve it with the image of the guide-star from a target observation. We would obtain the image of the star-field as if it were observed under the natural seeing conditions at the time of the target observations. In this way, the image of the deconvolved star-field contains the differences between the on-axis and off-axis PSFs. It is, in some sense, a map of the convolution kernel necessary to restore the off-axis PSFs over the field and will be referred to here as the PSF reconstruction map.

In order to handle non-uniformity arising from both signal levels and the random locations of stars, spatially-dependent PSFs are extracted from the reconstruction map using the DAOPHOT task PSF. The result is a corrective function which contains information about the spatial dependence of the PSF, produced by the AOB, the camera, and anisoplanatic effects. Convolution of this reconstruction map with the on-axis PSF will give the original spatially dependent PSFs of the star-field we started with. The effects of aberrations in the camera optics on the reconstruction map are negligible compared to anisoplanatism. Most importantly, it is found that the spatial correction functions extracted from star-fields under different seeing conditions in the same night are similar and thus can be used to correct a given on-axis PSF for the effects of anisoplanatism.

```
                    Image Reduction and Analysis Facility
PACKAGE = degrade
   TASK = offaxis

(focalra=                   8) telescope focal ratio
(obstruc=               0.389) ratio of secondary to primary

(scale  =               0.045) camera pixel scale in arcseconds per pixel
(gain   =                  2.) detector gain in electrons per digital unit
(noise  =                 30.) readout noise in electrons
(bandpas=                1.65) wavelength of observations in microns

(image  =           starfield) starfield to use in the calculations
(expose =                  1.) exposure duration in seconds
(xsize  =                 512) number of columns in starfield
(ysize  =                 512) number of lines in starfield
(skyback=                  0.) starfield background in digital units
(deviati=                  0.) starfield standard deviation in digital units
(xguide =                 216) x position of guide in pixels
(yguide =                 216) y position of guide in pixels
(diamete=                 216) diameter of guide extraction box

(kernel =                  3.) FWHM of convolution kernel
(iterati=                 200) iterations in the deconvolution
(limit  =                  1.) chi-squared limit for convergence

(infile =               guide) observed on-axis PSF image
(offset =                 20.) off-axis distance in arcseconds
(angle  =                 90.) off-axis position angle in degrees
(brightn=                  0.) magnitude difference with on-axis
(outfile=        guideoffaxis) degraded off-axis PSF image or field

(pattern=                 yes) generate telescope diffraction pattern
(magnitu=                 yes) aperture photometry of the starfield
(extract=                 yes) extract guide image from the starfield
(skirt  =                 yes) artificial wings for the guide image
(fakeit =                 yes) artificial guide for deconvolution
(doextra=                 yes) force the extraction of the guide
(forcefe=                 yes) force the use of pre-extracted guide
(deconvo=                 yes) deconvolve optics from starfield
(correct=                 yes) construct an atmospheric correction
(model  =                 yes) calculate diagnostic measurements
(regener=                 yes) regenerate starfield using model
(degrade=                 yes) degrade an on-axis PSF to off-axis
(degmap =                 yes) degrade an on-axis PSF over entire field
(interac=                 yes) display results

(archive=                    )
(mode   =                   q)
```

Figure 3.27: The AOTOOLS OFFAXIS interface.

To return an off-axis PSF of a given offset the program convolves a PSF from the appropriate position in the reconstruction map with an on-axis PSF. As a check, the program regenerates the original image. If the regenerated and original images do not match it is very clear by viewing the result of subtracting one from the other. When the result is poor, generally, it is because the extraction of the spatially variable PSF information (the reconstruction map) was done poorly. This is often the result of having too few stars in the star-field. Good results are obtained with a star-field with at least a few dozen stars uniformly scattered over a $1' \times 1'$ field.

In order to account for the effect of *changing* natural seeing the user can input a *different* on-axis PSF. For example, the program can return an off-axis PSF at an offset of 15″ using a guide-star image obtained under 0.8″ FWHM seeing and a reconstruction map obtained under 0.6″ FWHM seeing. In practice it is found that this will correctly predict the PSF for a 15″ off-axis star observed under 0.8″ FWHM seeing (See Section 5.2). In summary, the tasks ONAXIS and OFFAXIS allow the user to input an on-axis PSF which is coincident in time with a target observation and the programs will output a PSF correct for a specified off-axis offset.

3.4.7 Comparing the Image with the Point-Spread Function

The task PROFILE generates a radial profile of an object in an interface convenient for AO observations. It uses the IRAF task ELLIPSE to determine an elliptical isophotal fit to an object. The program can then be run a second time to generate pure model profiles. For example, if the observation

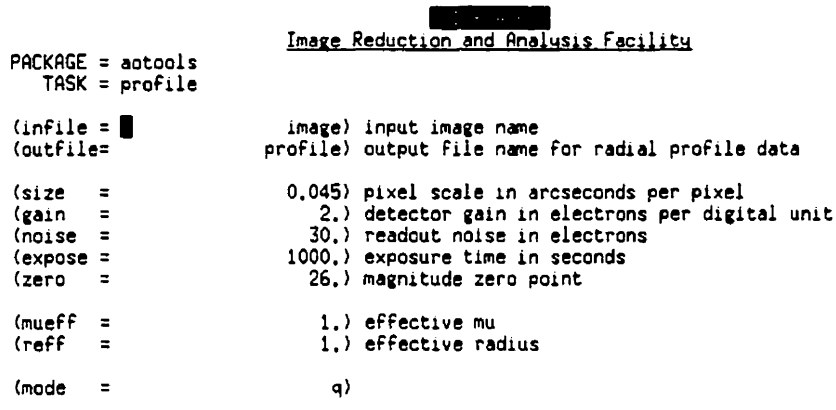

Figure 3.28: The AOTOOLS PROFILE interface.

is of an elliptical galaxy the program will return the profile of the galaxy and a fit based on the deVaucouleurs $r^{1/4}$ law (Equation 2.10). Finally, the program is run one more time on the image of the guide-star from the target observation (or the appropriate off-axis PSF). All three profiles are output to a file which allows direct comparison by the user. Since the profiles are all normalized to have flux of unity this provides a simple means of determining if the galaxy observation was resolved.

3.5 Comparison of Adaptive Optics Bonnette and Wide-Field Planetary Camera Observations

The great advantage of AO systems is that the spatial resolution they afford rivals that obtained from space-based observatories such as the HST. In fact, by virtue of their large aperture, telescopes such as the the CFHT permit resolutions *higher* than for HST. That is, the larger aperture gives a smaller

diffraction limit for the telescope. For correction in the NIR this provides for a diffraction-limited performance of $\sim 0.07''$ FWHM (J-band) for the CFHT while for the HST it is approximately 3.6/2.4 larger or $0.11''$ FWHM.

In order to take full advantage of this higher performance for CFHT AOB the pixel sampling of MONICA and KIR is at Nyquist frequency. This gives pixels that cover only $0.0350''$ on the sky (while for WFPC2 it is $0.0996''$). Now this is only an advantage if sufficient flux is available to all those physically small pixels. In the deep observations of faint objects discussed in this work this is almost never the case. The pixels are photon starved. This is, perhaps, even a drawback to the very fine sampling of the MONICA and KIR cameras since the PSFs in our off-axis observations are seldom narrower than $0.20''$ FWHM.

In order to compare the archival HST data and the CFHT AOB observations directly some means of rescaling the images needs to be found. A simple way of overcoming the disparity of the pixel samplings and also dealing with the issue of noise due to photon starvation for MONICA and KIR is to rebin the latter data to the same sampling as for WFPC2. This is the technique that was adopted.

I created a list of dense globular cluster fields visible from the CFHT's latitude and with a suitable guide-stars for the AOB. From these I found HST WFPC2 imaging of the same field that included the guide-star. For example, the dense core of M 5 is a popular HST WFPC2 target and provided adequate guide-stars for AOB.

Archival HST data were obtained from the Canadian Astronomy Data Centre (CADC) which is operated by the NRC HIA. The data were re-

constructed into a mosaic image using standard IRAF techniques found in the Space Telescope Science-Database Analysis System (STSDAS) package. Afterwards the image was rotated according to the spacecraft attitude information in the header. This means of determining the orientation of the image - based on the HST telemetry - is adequate for astrometric purposes.

By registering several stars in both images of a star-field taken with CFHT AOB and HST WFPC2, the orientation and pixel scale of MONICA and KIR can be determined. This is easily done by selecting several stars and applying a centroid-finding routine such as IMEXAMINE in IRAF. The relative distances of these stars gives the pixel scale of MONICA and KIR. The different aspect of the constellation of stars gives the rotation. With the WFPC2 image rotated and the pixel scale and orientation of MONICA and KIR known it is a straightforward task to register the two images using the IRAF task IMROTATE.

Chapter 4

Simulations of High Resolution Observations

4.1 Gemini North Telescope with Altair

The goal of this work was to determine if there is an advantage of extrapolation over no extrapolation of wavefront sensor (WFS) measurements for the Gemini North Telescope (Gemini) Altitude-Conjugate Adaptive Optics for the Infrared (Altair) system. This was tested with the software Altair-Offaxis which simulates the extrapolation of WFS measurements to operate a deformable mirror (DM) larger than the telescope pupil. To test the consequences of driving part of the DM without feedback (no local WFS measurement) these simulations were done with and without the effect of hysteresis in the DM.

Several simulations of various extrapolation techniques were run. The drop in Strehl-ratio with offset was used to judge the best extrapolation technique. First, a simulation with no extrapolation of WFS signals was used. As with all the simulations to follow, the correction within the pupil

was perfect to 105 Zernike modes. The drop in Strehl with offset was due purely to anisoplanatism. A simulation using the simple extrapolation of the Zernike modes - just assuming that the functions would hold outside the pupil - was run next. Extrapolation of 50 or more modes worked the best here. Extrapolation using slaving of DM voltages was then attempted. All of the possible configurations (as discussed in Section 3.1.2) were tried. The simulations that achieved the least degradation of the off-axis point-spread function (PSF) were ones using slaving. The optimal slaving function used a box of 3×3 actuators with a 1-actuator finger from each side of the box. The best result appeared to provide a net increase of 5% in Strehl-ratio in the extrapolated region over simulations with no extrapolation. Finally, the simulation with the best extrapolation was run again but with hysteresis included in the DM. This had, as expected, a result intermediate between optimal extrapolation and no extrapolation (See Figure 4.1).

As discussed in Section 3.1.2 the resolution of the simulation is limited solely by the number of pixels over the DM. Thus, an estimate of the uncertainty in the *relative* degradation of the PSF with offset can be made by varying this resolution. Reducing the resolution of the DM by 20% has no measurable effect on the relative positions of the lines in Figure 4.1 which suggests that the advantage in extrapolation is a real one.

Note that the Strehl-ratios quoted for all the results are for perfect correction within the pupil. This enables direct comparison of results by setting the intercept of all plots of Strehl-ratio versus separation to be the value for perfect correction of 105 modes. The on-axis Strehl-ratio for the simulations is approximately 75% and the best off-axis result appears to be a net in-

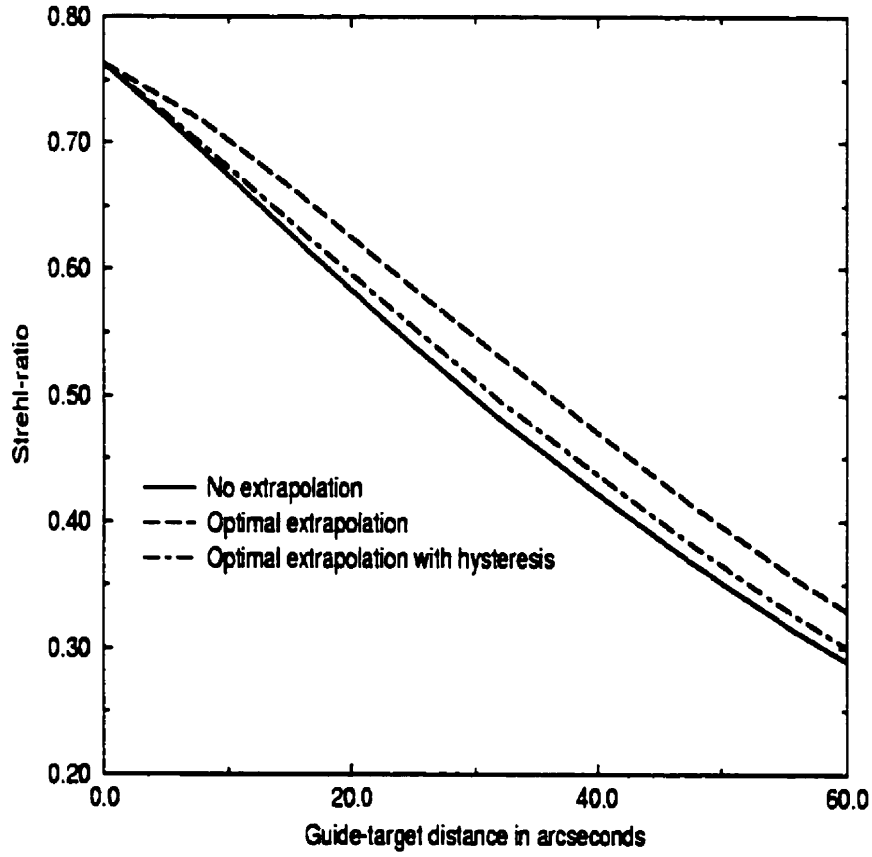

Figure 4.1: A plot of Strehl-ratio as a function of telescope offset for different extrapolation conditions.

crease of 5% in Strehl-ratio over no-extrapolation. The result that includes hysteresis is not strong because the hysteresis model that is implemented is not entirely physical. It is, however, probably an over-estimate and this suggests that hysteresis degrades the gains of extrapolation only somewhat.

My work suggests that it is possible to extrapolate the DM voltages to reduce anisoplanatism and that this advantage is not completely lost due to the effects of hysteresis. I presented these findings in a report to the National Research Council (NRC) Herzberg Institute of Astrophysics (HIA) (Steinbring 1998) and work carried out by Véran (1998) at HIA confirmed this result. The goal of these later simulations, however, was to determine a truly optimal extrapolation method. They suggest that with proper optimization of slaving an advantage of 10-20% in Strehl-ratio in the extrapolated region is possible.

4.2 Next-Generation Space Telescope

The following are the results of simulations of the Next-Generation Space Telescope (NGST) instruments using the software NGST VI/MOS. All of these results were presented in separate reports to the Canadian NGST Integrated Science-Instrument Module (ISIM) groups working on the Multi-Object Spectrograph (MOS) (Steinbring 1999A) and Visible Imager (VI) (Steinbring 1999B). They were also discussed in reports presented to the Canadian Space Agency (CSA) and the National Aeronautics and Space Administration (NASA) (Crampton et al. 1999, Hickson et al. 1999). I also presented my findings at the NGST Science and Technology Exposition in Hyannis (Steinbring 2000).

4.2.1 Visible Imager and Near-Infrared Camera

The goal of this work was to determine the advantage of observing with a dedicated VI imager relative to the NIR camera for wavelengths shorter than 1.0 micron. This is a straightforward experiment for NGST VI/MOS and was investigated using virtual observing runs. Two main tests were carried out. The first was to image high-redshift galaxies and attempt to detect star formation regions and globular clusters. This is similar to the program suggested by Lilly et al. (1998) in their DRM proposal. The second was to attempt to detect the white dwarf sequence in an extra-galactic globular cluster. This is similar to the DRM proposal of Rich and Margon (1998).

A realistic artificial galaxy field was generated. It was purposefully made to be clumpy. That is, the correlation-length parameter was set to 3.0″. This value was chosen because it is the smallest value for which severe overlapping of galaxies is not a problem. Setting this value to, say 0.5″, will cause almost all cloned galaxies to overlap another galaxy. By contrast, a value to 25.0″ produces essentially a random distribution of galaxies on the sky.

Several $H = 20 - 30$ galaxies were selected and imaged with both the VI and NIR camera through R and I filters. In all cases the the VI will have a distinct spatial-resolution advantage over the NIR camera for wavelengths shortward of 1 micron. Here, also, the efficiency advantage of hybrid visible silicon (HyViSi) detectors and mercury-cadmium-telluride (HgCdTe) arrays over indium-antimonide (InSb) arrays is evident. This is advantageous for programs of studying star-formation regions in galaxies with $z > 1$. For example, see Figures 4.2 and 4.3. The smallest structures clearly visible for VI imaging of this z=1 Scd galaxy from the NGST Deep Field vanish with

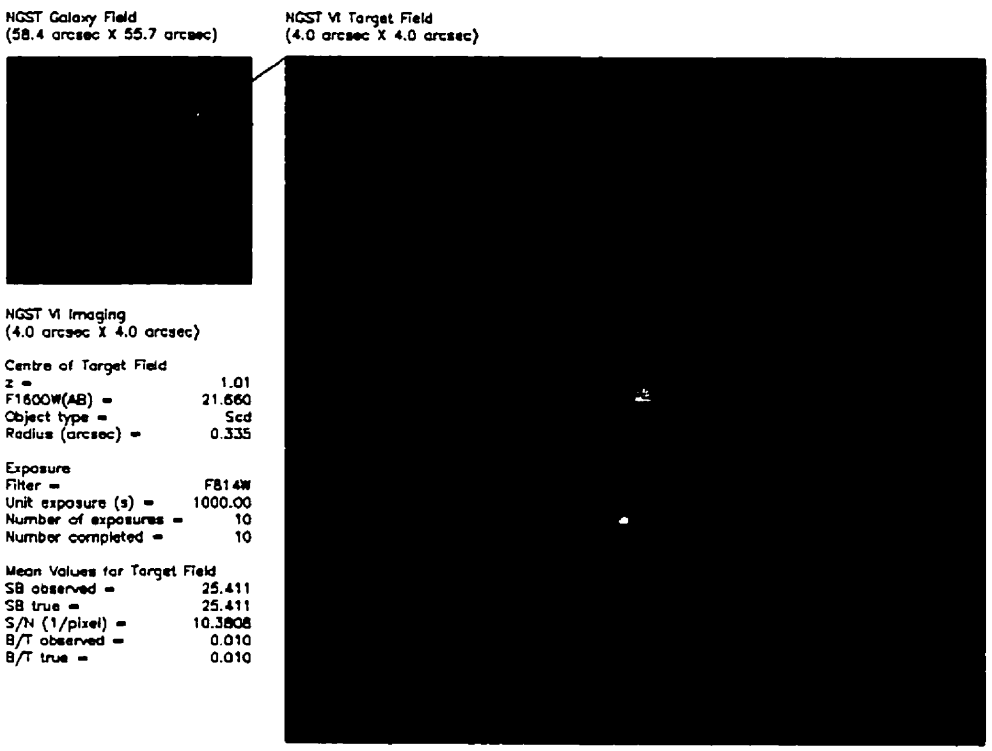

Figure 4.2: An image of a bright, $z = 1$ galaxy with NGST VI. Note the resolved core and numerous bright globular clusters and star-formation regions in the disk.

imaging by the NIR camera. Note that the measurement of bulge-to-total ratio (B/T) is noisier in the NIR camera image. This is typical of simulated observations made with this instrument. The poorer pixel sampling of the NIR camera makes fitting of a bulge function to the image more difficult - and the result is a noisier B/T.

A realistic globular cluster field was generated, similar to those that Rich and Margon (1998) propose to observe. It too was observed with both the virtual VI and NIR cameras in R and I filters. We can see from Figures

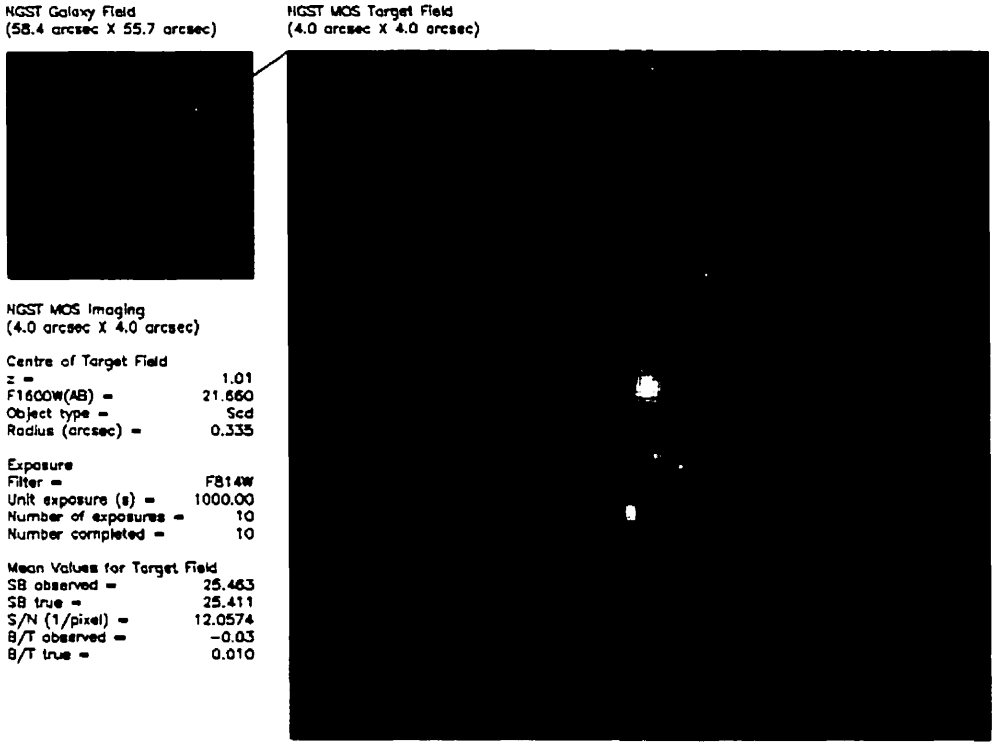

Figure 4.3: The same field as in Figure 4.2 imaged with the NIR camera. Note how the core is now blurred - most of the globulars and star-formation regions are now unresolved. The measurement of B/T is noisier than for the VI as well.

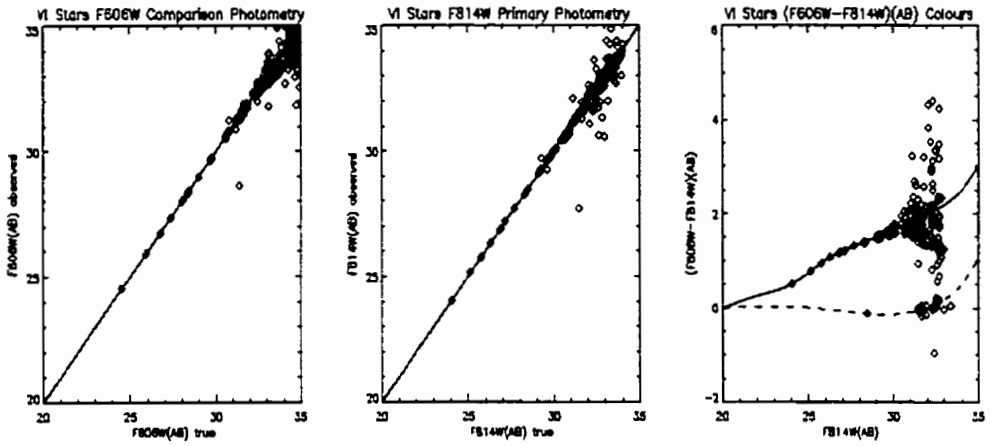

Figure 4.4: The photometry from a simulated NGST VI observation of an extragalactic globular cluster. The left and centre panels show the input versus output photometry through R and I filters and the right hand panel is the resulting CMD. The theoretical main and white-dwarf sequences (assuming they were uniformly populated) are indicated by a solid and dashed line respectively. Note the clearly resolved white dwarf sequence.

4.4 and 4.5 that for photometry of point sources the VI will perform better than the NIR imager for short wavelengths. Here, the distance modulus of M 15 has been increased by 8 and the correlation length set to 1″ during cloning. With faint stars very close together the better sampling and increased throughput of the VI makes detecting faint point sources easier. Imaging with a NIR camera would not detect the faint white dwarfs ($I > 30$) clearly evident in the VI photometry.

4.2.2 Multi-Object Spectrograph

The main goal of this work was to determine the S/N of extracted spectra as a function of galaxy brightness and spectrograph slit size. This is also a

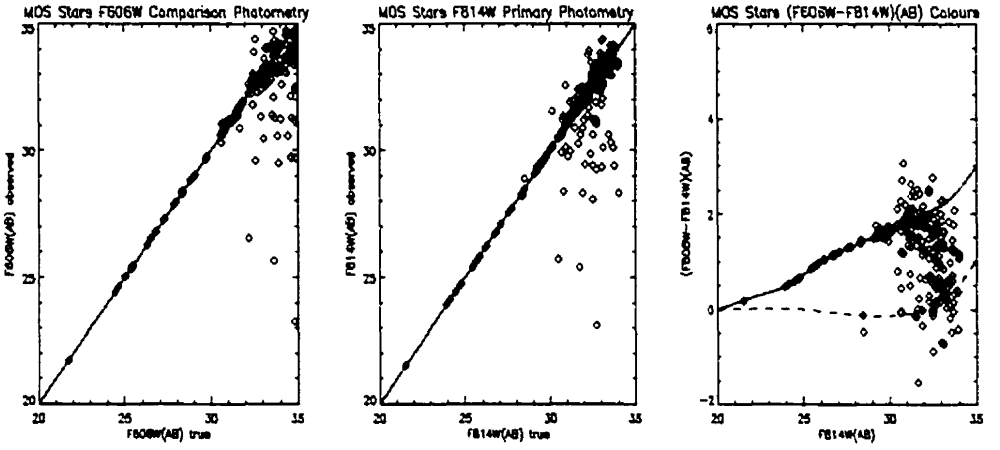

Figure 4.5: The same field as in Figure 4.4 observed with the NIR camera. Note how the white dwarf sequence is no longer detected.

straightforward experiment for NGST VI/MOS and was investigated using more virtual observing runs. Basically, the programs suggested by Lilly et al. (1998) in their Design Reference Mission (DRM) proposal were carried out with the simulation. These call for deep (10^6 s) exposures of galaxy fields. They propose low resolution ($R = 100$) spectroscopy of $H = 30 - 31$ galaxies to extend spectroscopic redshift surveys to the faintest limits possible. They also propose higher resolution ($R = 5000$) spectroscopy of brighter ($H = 26 - 28$) galaxies to determine characteristics of galaxy formation and evolution.

A realistic artificial field was generated, similar to that of the VI simulation. The simulation was run in multiplex mode with various slit widths and lengths. The spectrograph had 50 slits for the $50'' \times 50''$ field. This was based on the assumption of approximately 200 slits for a $2' \times 2'$ field for NGST. The simulation placed slits on the first 50 $H = 30 - 31$ galaxies selected at random, performed spectroscopy and returned the S/N.

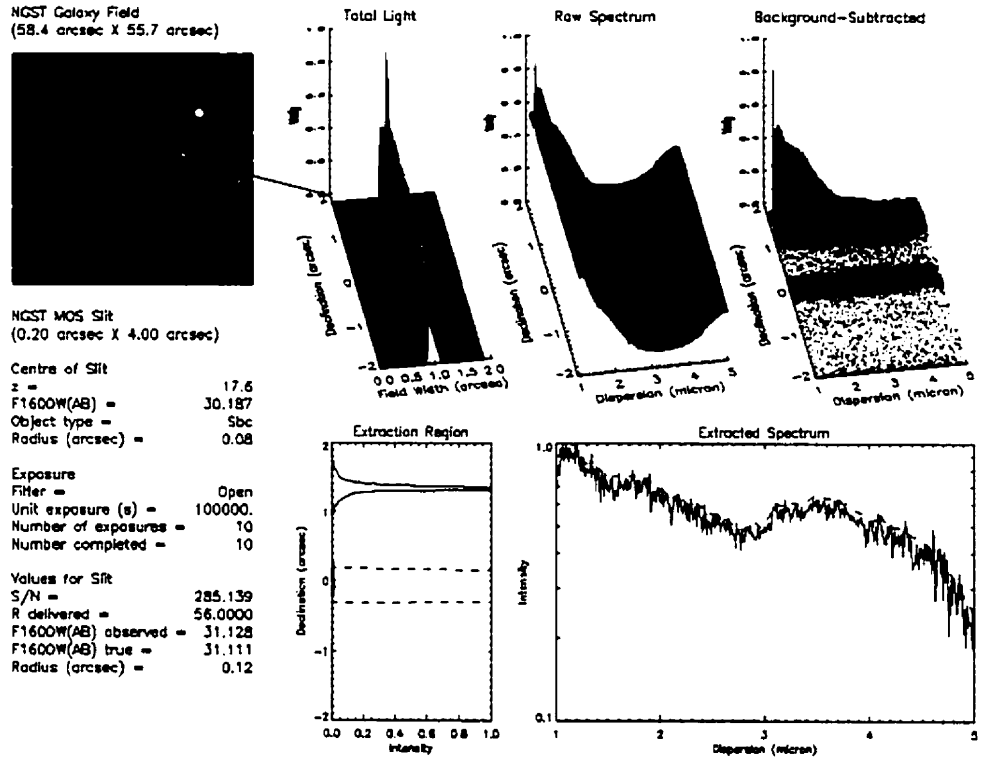

Figure 4.6: An image of the NGST MOS display. Galaxy selection is automated (upper left) as well as background subtraction (upper right) and extraction of the spectrum (lower left). The reduced spectrum is shown at the lower right. The resultant S/N and spectral resolution are displayed along the left-hand column.

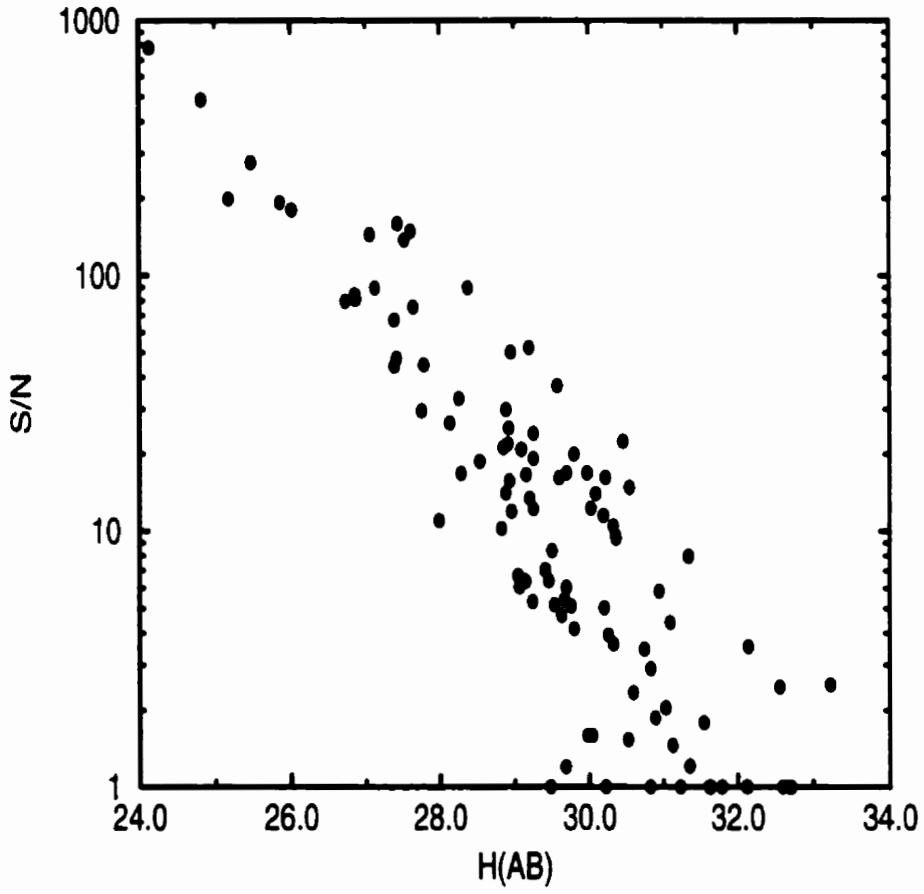

Figure 4.7: A plot of S/N versus H for galaxies in the HST Deep Field South as observed with NGST MOS. Slits were 0.2″ wide and the resolution was $R = 100$. The results are essentially identical for slits 0.5″ wide.

It quickly became clear that for the case of low resolution ($R \approx 100$) spectroscopy, slit width is not a critical factor. Faint galaxies ($H = 30 - 31$) are small - with half-light radii of only about $0.1''$. The small galaxy sizes determine the resolution of the spectra (although the grating resolution must be increased to maintain a resolution of $R = 100$). As long as the slit is not much wider than about $1.0''$ the increase in background light does not adversely affect the S/N of the spectra. This is assuming that *no other galaxy* finds itself in the way of the galaxy of interest. It is found, however, that this is often the case if the slit is wider than $0.5''$. Thus the size of the slit is effectively limited by the galaxy density of the fields. These simulations also suggest that background subtraction is very effective in space. For co-adds of 1000 s exposures a calibration slit placed on the 'sky' will provide excellent subtraction of the background. This is why the slit width can be as large as $1.0''$ in the absence of crowding by other galaxies. These results suggest that $S/N \approx 10$ spectroscopy of $H = 30$ galaxies will be possible with NGST. Although the NGST field is crowded at these depths, roughly 50 $1.0'' \times 0.2''$ slits or fibre-bundles per square-arcminute are possible with no spectral overlap. This configuration is roughly optimal for a low resolution ($R = 100$) deep (integration $\sim 10^6$ s) galaxy survey.

The second DRM proposal investigated was that of surveying relatively bright ($H = 26 - 28$) galaxies at higher resolution. It was clear that there would be no difficulty concerning S/N for these galaxies. Typical values are in the hundreds, if not a decade more than that for exposures of 10^6 s. These brighter galaxies generally have fairly large apparent sizes, typically being larger than $1.0''$ across. A $0.2''$ slit will not cause a problem with

contamination by other galaxies and will still provide ample light for the spectrograph. One concern, however, is that high resolution spectroscopy requires a lot of area on the detector. Each spectrum would be, say, 1.0″ long, and dispersed along 10000 pixels on the detector. Thus even if the blue end of the spectra began at the leading edge of the detector, 50 galaxies would completely cover the detector in spectra. In this case, a fibre-fed spectrograph may be advantageous for resolutions approaching $R = 5000$. A fibre system can maintain 50 1.0″ slits per square-arcminute whereas a slit-mask would always have overlapping spectra.

Although it was determined that 1.0″ × 0.2″ slits were roughly optimal for the MOS there are engineering constraints on the Canadian slit-mask designs which might make 4.0″ slits more desirable. Also, the detector size available for the MOS would limit resolutions to roughly $R = 1500$ for a 3.0′ × 3.0′ field. The two DRM proposals described above were also studied using 4.0″ long slits and assuming that the square-arcminute field of the simulation covered only 1/9 of the MOS field. These results are shown in Figures 4.8 and 4.9. Note that the simulation covers only the lower left-hand square arcminute of the MOS field. At least two more banks of spectra will be possible in the dispersion direction. Also, this is only 1/3 of the total field in the direction perpendicular to dispersion.

Figure 4.8 shows the result of randomly selecting 300 galaxies with H of approximately 30 (This is also roughly how many galaxies of this brightness there are in the field). Low resolution ($R = 300$) spectra have been taken. The efficiencies for a micro-mirror slit mask, fibres, movable bands, and micro-machined shutters are very similar. We can see that the micro-

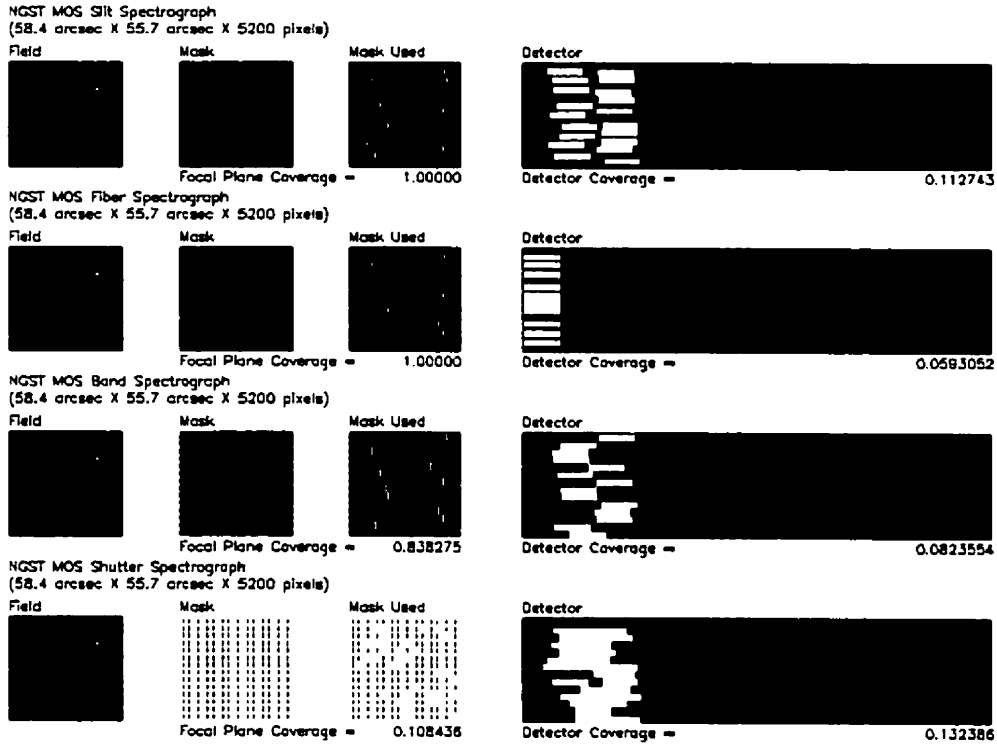

Figure 4.8: A comparison of slit-mask designs for observations of the NGST Deep Field South using 4.0″ long slits and achieving $R = 300$ spectra.

mirror array tends to break up the field into two bands of spectra whereas the fibre array can gain access to the entire field. A second pointing would allow the micro-mirror array to reach the objects in the centre of the field. A second pointing of the fibre mask would allow it to double the number of objects it observes. An advantage for the fibre case is that with the spectra reformatted to start at the leading edge of the detector, higher-resolution spectra will be possible than with the micro-mirror array. It appears that since faint objects are plentiful there is no penalty for the poorer field coverage of the micro-shutter array (although some spectral overlap has been tolerated to achieve this).

Figure 4.9 shows the result of randomly selecting 50 galaxies with H of approximately 25 (This is also roughly the number of galaxies of this brightness in the field). Moderate resolution ($R = 1500$) spectra have been taken. Note how the ability to reformat the spectra allows the fibre mask to cover the detector efficiently. All of the other methods would now suffer from spectral overlap with the neighbouring band of spectra. Perhaps for these methods the problem could be solved (with some cost to efficiency) by using a band-limiting filter.

Confirming the expectations of the Canadian MOS design, an image slicer is a powerful method of obtaining both high spatial and spectral resolution over a selected area. Figure 4.10 shows an example of reformatting the spectra of a bright galaxy with a $2.0'' \times 4.0''$ image slicer using 22 slices. Pixel sampling is $0.03''$ per pixel (perpendicular to dispersion) and the spectral resolution is $R = 1000$. The outline of the spectrum on the detector helps to determine optimal parameters for the image slicer. From this simulation

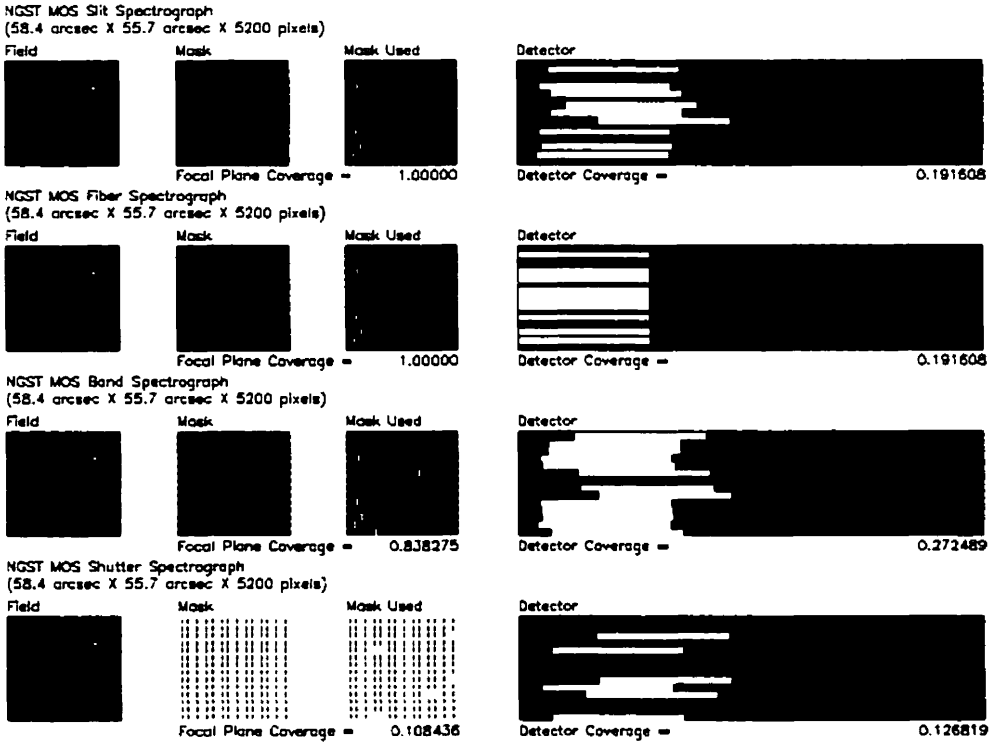

Figure 4.9: A comparison of slit-mask designs for observations of the NGST Deep Field South which use 4.0″ long slits and achieve $R = 1500$ spectra. The top row shows the results for the micro-mirror mask. Below this are the results for fibres, movable bands, and micro-machined shutters.

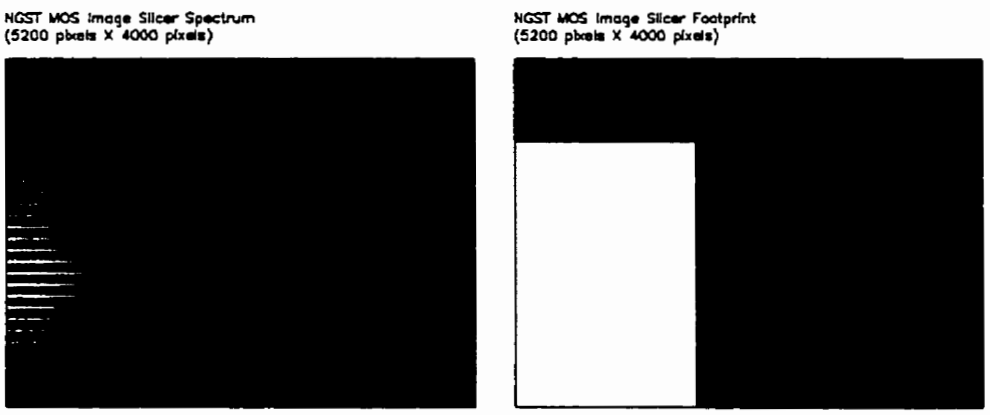

Figure 4.10: The resultant image and detector-coverage for the IFU. It is a $2.0'' \times 4.0''$ image-slicer employing 22 slices, pixel-sampling of $0.03''$ per pixel and $R = 1000$.

we can see that, actually, $0.02''$ per pixel will be possible for 22 slices. Also, spectral resolutions of 2000 to 3000 will take better advantage of available detector area.

Chapter 5

Observations of High-Redshift Radio Galaxies

5.1 Target Selection

Possible radio galaxy (RG) targets were chosen in the following fashion. First, all objects catalogued by the National Aeronautics and Space Administration (NASA) Extragalactic Database (NED) as an RG with $z > 1.0$ and visible from the Canada-France-Hawaii Telescope (CFHT) during our observing runs were found. That is, these were galaxies that were *identified* with an optical component. This yielded a target list including hundreds of candidates. Next, the United States Naval Observatory (USNO) Guide-Star Catalogue (GSC) was used to determine all of those targets within 45″ of a $R < 15$ star. This reduced the target list to only 25 members.

Finally, of the targets remaining, only those with archival Hubble Space Telescope (HST) Wide-Field Planetary Camera 2 (WFPC2) data were included. The last step was applied to ensure that high-resolution optical observations would be available for all the targets. This reduced the sample

to 12 members. We might be concerned that since the HST sample had a different selection criterion (essentially, not being dependent on having a guide-star) this might affect the selection of the sample. However, all but one (TXS 0828+193) of the remaining galaxies in the sample were from either of the 3C and 4C Catalogues of radio sources. These were observed with the HST in snapshot-mode which means that they were observed for short periods upon selection from a large list (all 3C and 4C sources) based on accessiblility and scheduling constraints.

It is not expected that this selection has a strong bias towards, say, highly elongated RGs since the 3C and 4C Catalogues contain both QSOs and RGs. The galaxies are selected with the same radio-flux criteria. We can characterize our sample, then, as selected from all identified RGs from the 3C and 4C Catalogues visible from CFHT with a guide-star suitable for the Adaptive Optics Bonnette (AOB). The redshift distribution of the objects observed from the final target list is uniform over $1 < z < 4$ and, thus, this gives a small but representative sample of high-redshift RGs (HzRGs).

5.2 Calibration

Photometric standard stars from the United Kingdom Infrared Telescope (UKIRT) catalog were observed. Star FS 30 was used as a calibrator in June 1997 using the Montreal Near-Infrared Camera (MONICA). In January 1998 the star FS 21 was used to calibrate the 1024 $\times$ 1024 pixel infrared camera (KIR).

The observations were short (5-20 s) and performed at several telescope pointings within a dithering pattern. These dithered images were registered

Table 5.1: Standard Stars

	Position (J2000)		Magnitude			
Target	α	δ	J	H	K	Date
FS 30	22:41:44.6	01:12:38	11.923	11.979	-	14, 15 June 1997
FS 21	11:37:05.4	29:47:58	12.948	13.031	13.132	18 January 1998

Table 5.2: CFHT AOB Photometric Calibration

	Zero-point (magnitudes)		
Camera	J_0	H_0	K_0
MONICA	22.216	22.141	-
KIR	23.623	23.052	22.450

and averaged to form final images of the standard stars. Synthetic aperture photometry was performed on the final images using the Image Reduction and Analysis Facility (IRAF) task APPHOT. A 3″ diameter aperture was used to ensure that all of the flux was included. This was necessary since, at times, the AOB was not functioning optimally and the point-spread function (PSF) tended to be larger than during the galaxy observations. Table 5.2 contains the calibration information calculated from these stars.

For the archival HST data the photometric zero-points and first-order transformations to the standard Johnson filter set were found in the WFPC2 Instrument Handbook (Biretta 1996). These are listed in Table 5.3.

Synthetic PSFs were generated by wavefront sensor information in order to monitor the natural and delivered seeing during the observations. The latter information is produced in real time by software made available to AOB users by CFHT (Véran et al. 1996).

Table 5.3: HST WFPC2 Photometric Calibration

Zero-point (magnitudes)			
$F675W_0$	$F702W_0$	$F785LP_0$	$F814W_0$
24.34	24.76	23.23	24.13
Transformation (magnitudes)			
$F675W_0 - R_0$	$F702W_0 - R_0$	$F785LP_0 - I_0$	$F814W_0 - I_0$
0.65	0.78	1.13	1.26

Observations of dense star fields were made during commissioning in June 1996 and during the observing runs in June 1997 and January 1998.

In June 1996 and June 1997 observations through J, H, and K filters of the globular cluster M 5 were made. The generation of a wide-field mosaic was made difficult by the small field of view (FOV) of the MONICA camera. A mosaic pattern was used to obtain a roughly 12″ wide by 30″ long strip with the guide-star at one end. The mosaic was composed of 6 individual pointings of the telescope. At each position a dithering pattern was used to build up an image. Since the guide-star appeared in only one of the component images and time lapse of several minutes occured between each pointing a danger with this method was that the PSF would change during the construction of the mosaic. This did not appear to be a problem because stars in overlapping regions in the mosaic were almost identical. In each overlapping region the FWHM of a particular star in both frames was not different by more than 5%

In 1998 the KIR camera was available. Its larger (36″ × 36″) FOV provided for much easier construction of a mosaic. The guide-star was placed in each of the corners of the camera FOV and a dithering pattern was made

Table 5.4: Star-Field Calibration

Target	Position (J2000) α	δ	Guide-star Magnitude (R)	Date
M 5	15:18.5	02:05	10	25 June 1996, 16 June 1997
NGC 4147	12:10.1	18:33	12	16, 17, 18 January 1998

at each position. By registering the guide-star in all the frames a large square-arcminute mosaic was constructed. This proved to be a very effective method of generating a star-field image. Unfortunately, there was a paucity of dense star-fields visible from CFHT during this run. The globular cluster NGC 4147 was used. It was dense enough to permit about half of the FOV in the mosaic to be covered with bright stars. Again, comparison of stars in overlapping regions of the mosaic confirmed that the AO correction did not change during the dithering process. As with the M 5 data, the FWHMs of a particular star in the overlapping regions of both frames did not differ by more than 5%.

These globular cluster field data were compared to HST WFPC2 observations of the same fields in order to determine the plate scale and orientation of the AOB camera. First, the archival WFPC2 images were rotated from the spacecraft orientation given in their header (the $V3$ axis) using the IRAF task IMROTATE. The positions of several of the same stars in both AOB and WFPC2 observations were noted. The plate scale of the WFPC2, the value published in the WFPC2 Instrument Handbook (Biretta 1996), was used to determine a plate scale for the AOB. Using the IRAF tasks IMROTATE and MAGNIFY the AOB images were rotated and rescaled to have

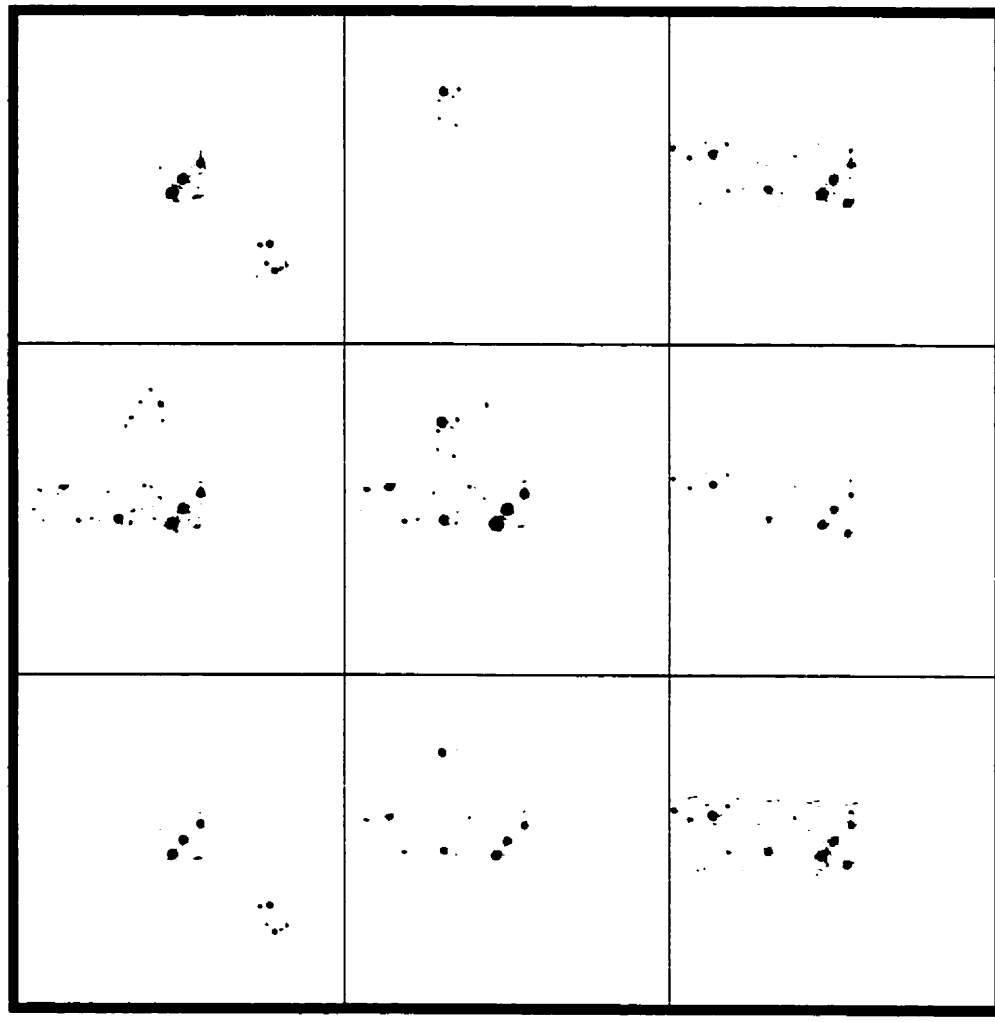

Figure 5.1: Images of the M 5 star-field. The top row is in J-band, middle is H, and bottom is K. The left-hand and middle columns are two series of observations from 25 June 1996 and the right-hand column is from 16 June 1997. The FOV of each image is $1' \times 1'$. North is up and east is left with the guide-star in the centre of each frame.

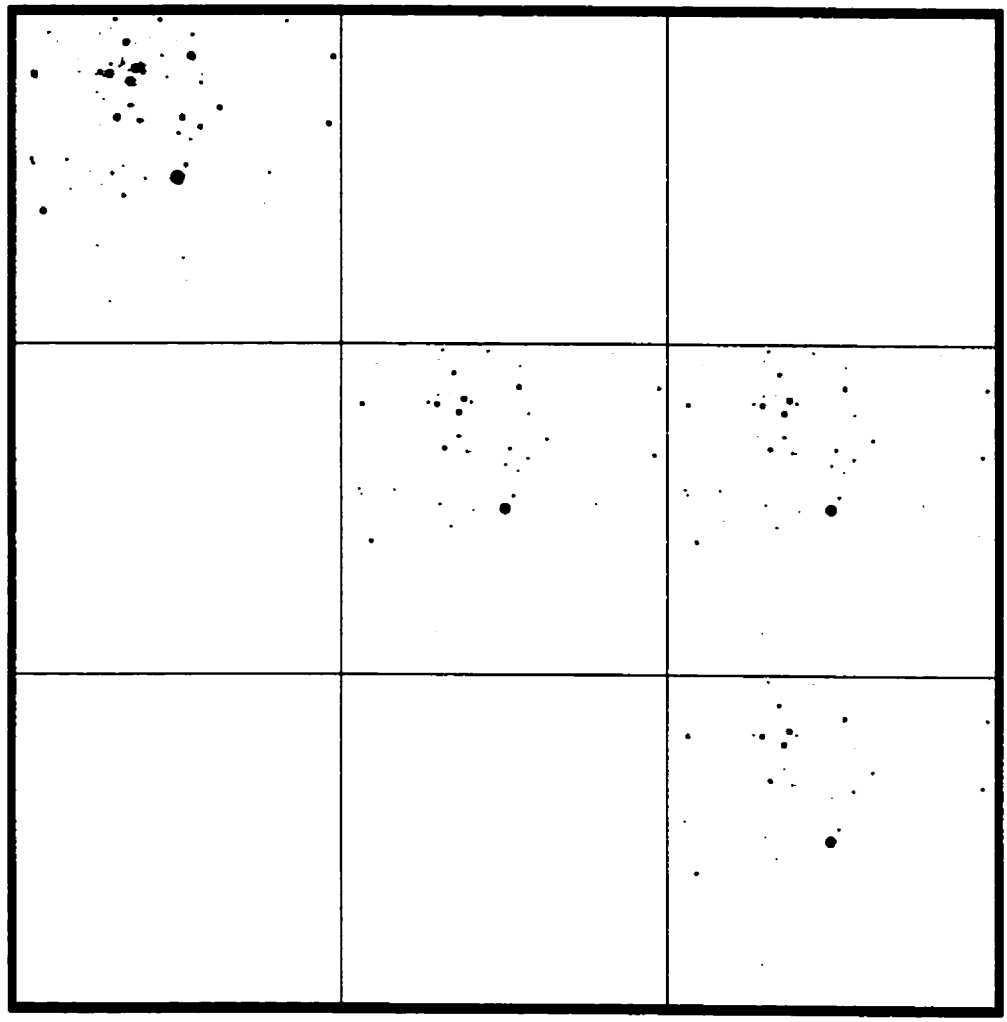

Figure 5.2: Images of the NGC 4147 star-field. The top row is in J-band, middle is H, and bottom is K. The left-hand column is from 16 January 1998, the middle column from 17 January 1998, and the right-hand column from 18 January 1998. Image-scale and orientation are the same as in Figure 5.1. Panels corresponding to observations with a saturated image of the guide-star have been left blank.

Table 5.5: Plate-Scale and Orientation

Instrument	Plate-scale ("/pixel)	Rotation (degrees)
CFHT AOB MONICA	0.0347	101.13
CFHT AOB KIR	0.0350	-0.17
HST WFPC2	0.0996	*V*3-225.00

Table 5.6: Detector Information

Camera	Gain (electrons/ADU)	Readout (electrons)
MONICA	2.0	30
KIR	3.6	20
WFPC2	7.0	5

the same orientation and pixel sampling as the WFPC2 images. Plate-scales and orientations are given in Table 5.5. Also, the gains and readout noise of the detectors are given in Table 5.6.

The second goal of these observations was to determine the AOB PSF over a large FOV in order to determine if the target galaxies were resolved. The use of the large FOV KIR camera allowed the observations of the galaxies to be made while including a nearby star suitable for determining the PSF at the target position. So, in most cases, the PSF analysis task DEGRADE was not critical in the determination of the AOB PSF at the galaxy position. This technique has been applied to the QSO host program and a discussion of the results is available in Hutchings et al. (1998). The discussion there is rather brief and, therefore, a thorough analysis of the star-field observations is provided here.

As discussed in Section 3.4.6, the task DEGRADE is used to determine

the PSF everywhere in the AOB FOV and is based on observations of a dense star-field. An image of a star-field with the guide-star in the centre (and not overexposed) gives the information necessary to determine the spatial variation of the PSF at the time of the observation.

The best means of demonstrating this technique is to reconstruct an off-axis PSF with the use of only an image of the on-axis guide-star and a map of the PSF variation. Then we should compare this reconstructed PSF with a real image of a star at that position relative to the guide-star during the same seeing conditions. It would be convincing, then, if the test were to reconstruct an off-axis PSF correctly based on PSF variation maps produced from star-fields observed, say, earlier in the night or the previous night. It would be very convincing if all of these tests were made with the same star-field and there was an observation of each star for comparison to its reconstructed image.

The first test is to find if the method can reproduce the anisoplanatism in the PSF in a radial direction from the guide-star. The goal here is to show that a map generated with different on-axis seeing conditions can be used to find the variation in the off-axis PSF. The long-strip observations of M 5 serve this purpose well. Two observations were taken on the same night under very different natural seeing conditions - during 0.6″ FWHM and 0.9″ FWHM seeing. A third observation was taken almost exactly a year later. The second test is designed to find if the azimuthal change in the anisoplanatism can be modelled with this method. The observations of NGC 4147 serve here because they cover a wide field and not just a strip. The natural seeing conditions during these observations were similar. In all

cases the star-fields were observed at similar altitudes and azimuths with the telescope - in effect they are in the same spot in the sky. The choice of guide-star was maintained in the M 5 and NGC 4147 observations. See Figures 5.1 and 5.2. This had the effect of ensuring that there were no uncontrolled variables in the experiment. The tests are simple - reproduce the star-field based on a PSF variation map generated from an earlier observation of that same star-field.

The first test is for the correct modelling of radial anisoplanatism. The M 5 data are used. Figure 5.3 shows the azimuthally averaged PSF of the guide-star and stars in the field at radial distances from the guide-star of approximately 5″, 15″, 20″, and 25″ in H-band. The filled circles represent the second mosaic data from June 1996. The solid line is the PSF for that location reconstructed from the PSF variation map using the first mosaic data obtained in June 1996. The dotted line is simply the raw PSF data taken from that first field *without* correcting for the difference in the on-axis PSFs. In a sense, the dashed line is what we would predict the PSF would be at a later point in the night if all that was available was the mosaic from earlier in the night.

The solid line represents a prediction based on *knowing* the on-axis PSF at any given point in the night. The fit of the solid line to the data indicates how well the method predicts the PSF during a single night. How poorly the dashed line fits the data demonstrates how important it is to know the on-axis PSF at the time of a given observation. This is made even more clear by looking at the model fit to the guide-star data (upper-left). the dashed line represents the guide-star data taken from the star-field obtained earlier in the

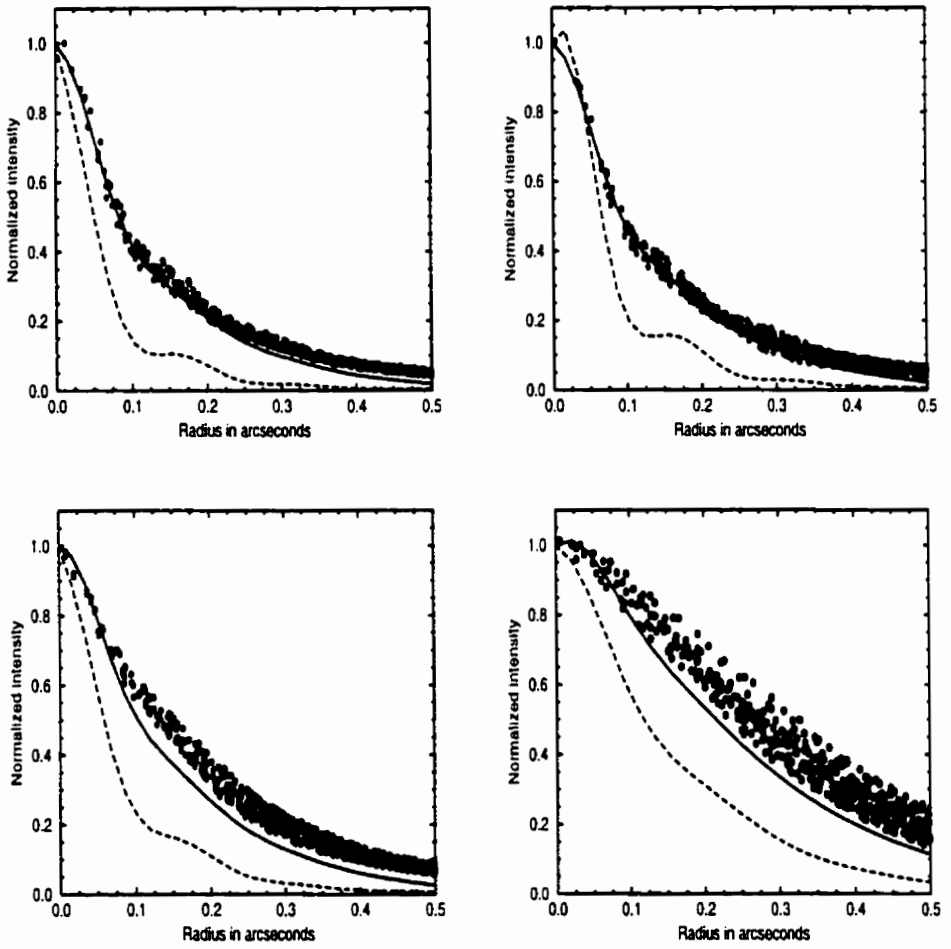

Figure 5.3: A plot of the PSFs of M 5 in image 2 restored with the image 1 reconstruction map. Shown are offsets of 0″ (upper-left), 5″ (upper-right), 15″ (lower-left), and 25″ (lower-right). The filled circles are the data from image 2. The dashed curves represent the normalized radial profiles of the PSFs from image 1 and the solid curves represent the model PSFs.

night. Clearly, the seeing has changed dramatically. The model, as one might expect, recovers the guide-star PSF but also recovers the anisoplanatism of the other off-axis PSFs.

Figure 5.4 is similar to Figure 5.3 but in this case the raw data are from June 1997. the dot-dashed line represents the data from the first mosaic of June 1996, the dashed line that of the second mosaic of that night. The solid line is the PSF reconstructed using the PSF reconstruction map generated from the second mosaic of June 1996.

If we had simply used the star-fields from the previous year's run to predict the PSF, the prediction would be either too narrow or too broad. This is true at all radii from the guide-star (although the S/N is rather low for the 25″ radius position). Comparison with Figure 5.3 suggests that this is due to different natural seeing during these observations of M 5. Again, as we might well expect, the model correctly recovers the guide-star PSF for the June 1997 data. The fact that the model also correctly predicts the off-axis PSFs suggests that the PSF reconstruction maps from a *previous year's* run are adequate. This also suggests - although it is not proof - that the atmospheric conditions above the telescope do not change dramatically from year to year.

Now that it is established that the model can predict the radial dependence of anisoplanatism a logical question is whether it can detect any azimuthal dependence. The NGC 4147 data are used to test this.

Figure 5.5 shows data and their model fits at radial distances of 10″ from the guide-star at azimuthal directions centred on the guide-star of east, northeast, north, northwest, and west. The raw data, represented by filled

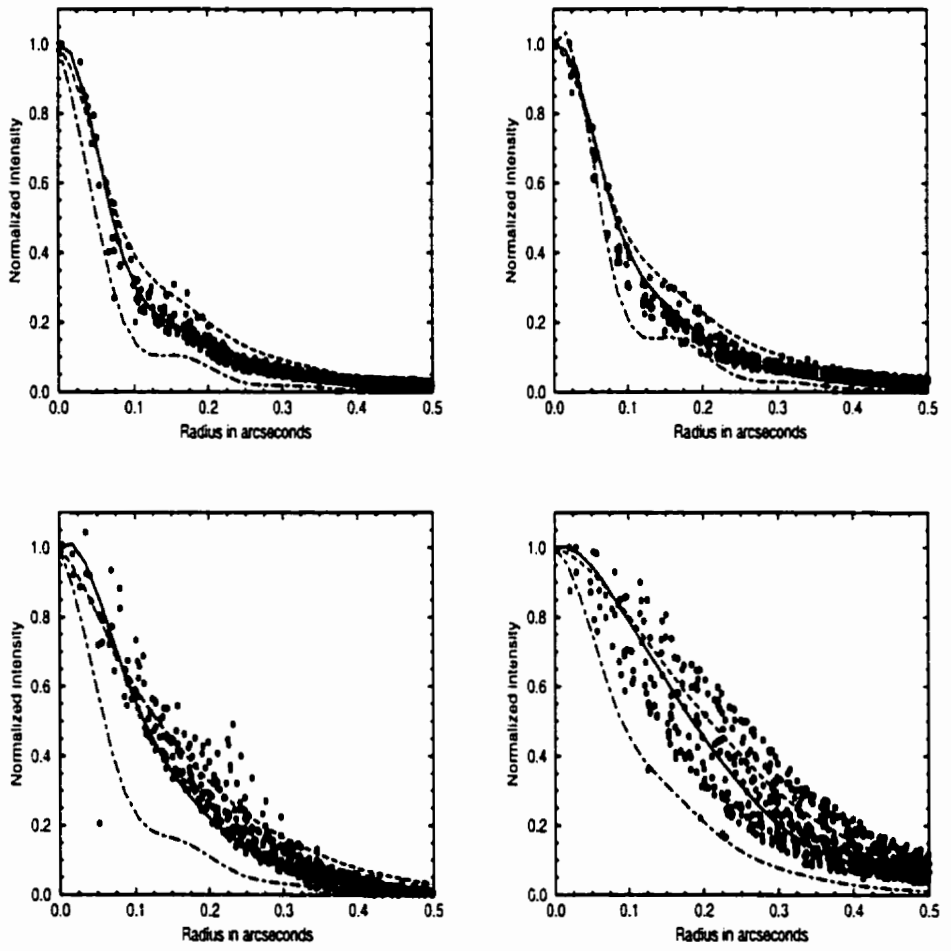

Figure 5.4: A plot of the PSFs of M 5 in image 3 restored with the image 2 reconstruction map. Shown are offsets of 0″ (upper-left), 5″ (upper-right), 15″ (lower-left), and 25″ (lower-right). The filled circles are the data from image 3. The dot-dashed curves represent the normalized radial profiles of the PSFs from image 1. The dashed lines represent the normalized radial profiles from image 2 and the solid curves represent the model PSFs.

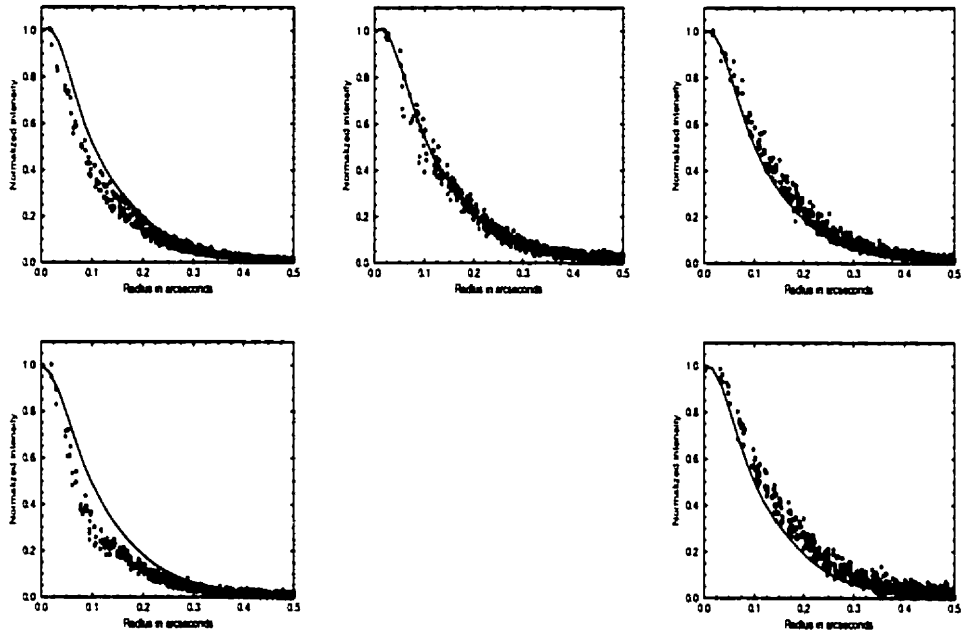

Figure 5.5: A plot of PSFs at an offset of 10″ in the NGC 4147 image 2 restored with the image 1 reconstruction map. Clockwise from lower left are east, northeast, north, northwest, and west. The filled circles are the data from image 2 and the solid curves represent the model PSFs.

circles, are from the January 1998 run. The solid line is the model PSF reconstructed from the PSF variation map generated from the January 1998 star-field data. Clearly, the model is unable to predict the PSF for the eastern and northeastern positions but does predict northern and northwestern ones. Again, the model does not correctly predict the PSF in the western position.

A similar situation is true for stars at radial distance from the guide-star of 20″ (Figure 5.6). The prediction at the eastern and northeastern positions is a poor fit to the data but the prediction at the northern, northwestern,

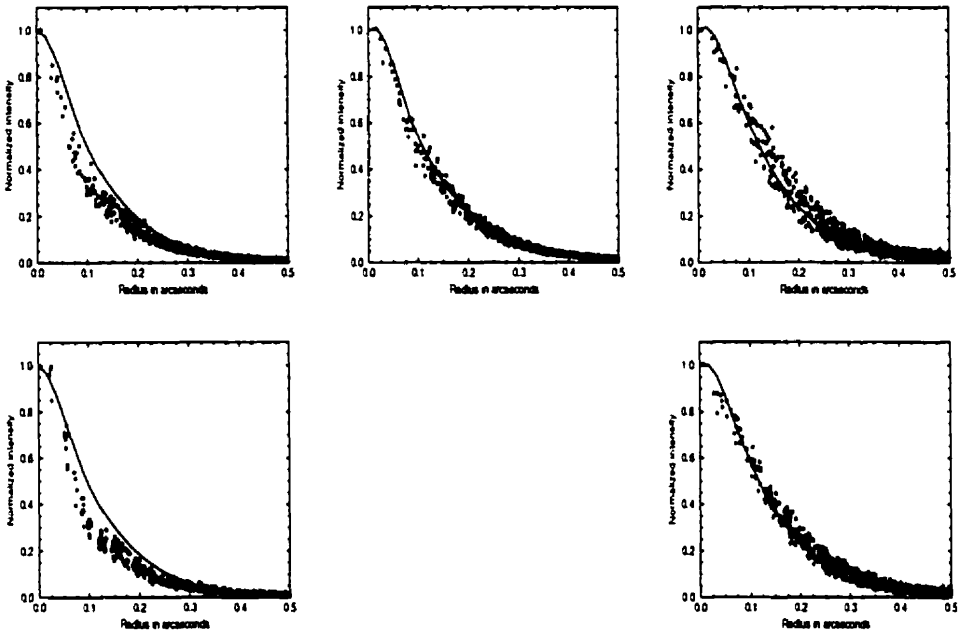

Figure 5.6: A plot of PSFs at an offset of 20″ in the NGC 4147 image 2 restored with the image 1 reconstruction map. Clockwise from lower left are east, northeast, north, northwest, and west. The filled circles are the data from image 2 and the solid curves represent the model PSFs.

and western positions is quite good.

All of the 10″ offset PSF data is shown in Figure 5.7. Overplotted are all the fits for the same stars. This is also shown for the case of a 20″ offset (Figure 5.8). These plots suggest that the model can predict *on average* what the PSF will be at a given radial offset from the guide-star. It does not, however, accurately predict the difference that depends on the azimuthal angle centred on the guide-star. This is perhaps not surprising since the PSF reconstruction map was generated from a star-field image obtained on a previous night. The images were of the same target field at the same

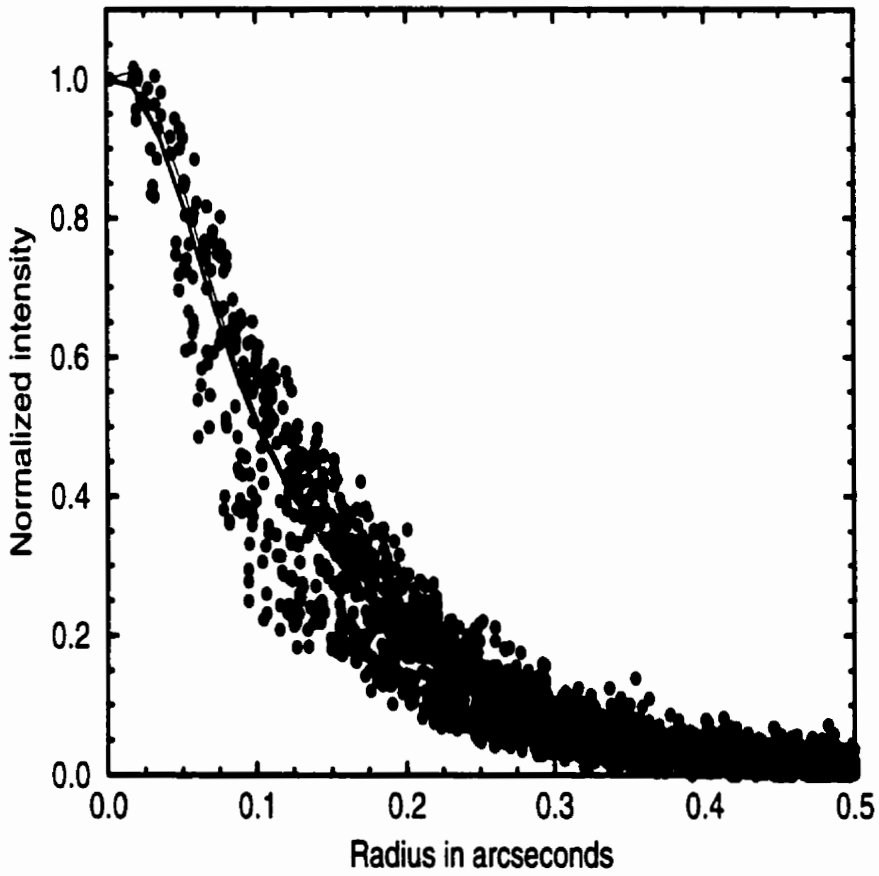

Figure 5.7: All of the stellar PSF data for offsets of 10″ in the NGC 4147 field. The model PSFs are overlaid as solid lines.

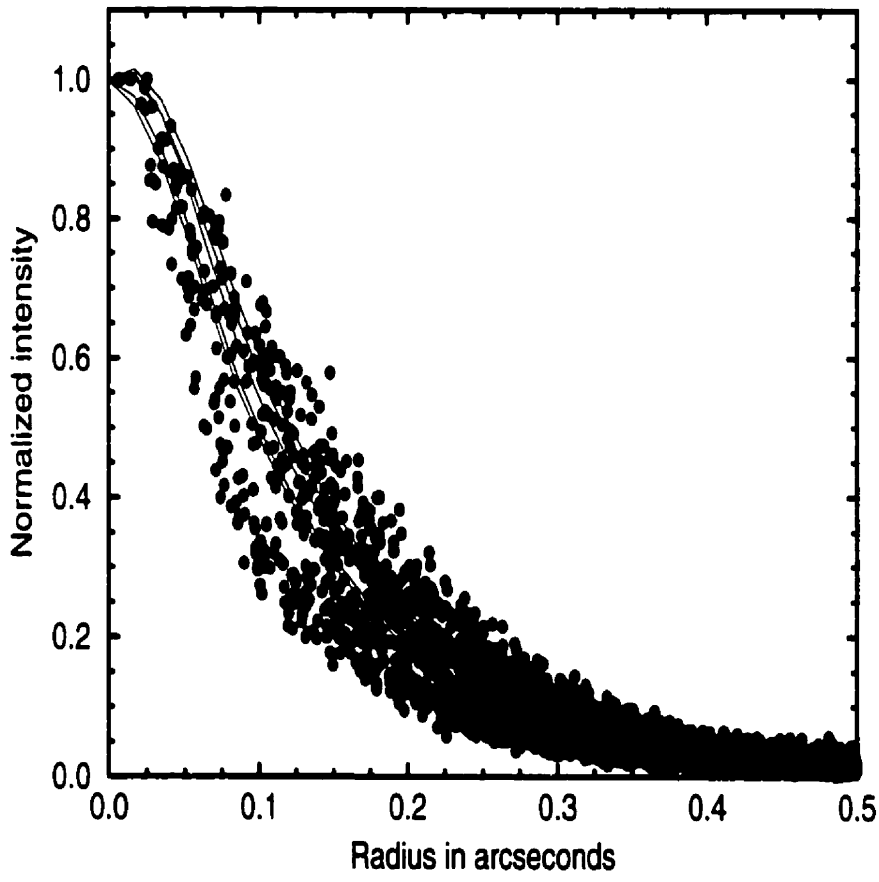

Figure 5.8: All of the stellar PSF data for offsets of 20″ in the NGC 4147 field. The model PSFs are overlaid as solid lines.

time of night and the seeing was also similar in the two cases. However, it is highly improbable that all atmospheric conditions were identical during both observations.

One possible explanation would be that the wind directions were different in the two cases. This speculation is suggested by the fact that the star-field data - the observations made during 18 January 1997 - have a narrower PSF towards the east than the previous night's data. Perhaps a westerly wind was 'moving' the isoplanatic patch off to the east (see Section 2.3.1). That is, the time delay between wavefront-sensing and correction with the AOB would degrade correction upwind. The western edge of the pupil would be presented a region of wavefront different from that which the wavefront sensor had measured.

The only way to determine if this is the cause would be to have many observations of star fields and record the wind speed above the dome. Although wind speed and direction measurements at ground level were available during these observations (from the weather tower on the CFHT site) they were not recorded. The prevailing upper atmospheric ($\sim$ 8000 m) wind over Hawaii was westerly during these observations. This was determined from comparing successive archival IR observations (showing atmospheric water vapour) from the Geostationary Operational Environmental Satellite 10 (GOES-10) using an internet based animation tool for that purpose (see the National Oceanic and Atmospheric Administration (NOAA) website). I estimate that this wind speed was approximately 8 ± 4 m s^{-1} during the run and, thus, a change in direction of this wind is not likely to be the cause of the change in correction (see Equation 2.34).

Future star-field observations should be complemented with recordings of wind speed and direction at the dome (now available from CFHT) and, perhaps, satellite imaging as well. The real-time numerical atmospheric models based on satellite observations which were developed by the National Centers for Environmental Prediction (NCEP) might also be incorporated.

Overall, the observations of M 5 and NGC 4147 suggest that the task DEGRADE is capable of predicting the radial variation in the PSF. It is unclear if it can predict any azimuthal variation in anisoplanatism. A more intense campaign of observations of globular clusters - with many observations of the same field in one night - should be able to tackle the azimuthal variation problem.

5.3 Adaptive Optics Imaging

We obtained CFHT AOB data during observing runs in June 1997 and January 1998. In all observations a $12 < R < 15$ guide-star was used to guide the AOB. During the 1997 run only the 256×256 pixel camera MONICA was available. Its poor sensitivity hampered our efforts to obtain deep exposures of the RG fields. The small field ($9'' \times 9''$ with $0.0347''$ pixels) meant that neither the guide-star nor any star suitable for determining the PSF was included in the target field. The 1024×1024 pixel dedicated NIR imager KIR was used in our 1998 run and its greater sensitivity ($\sim 4\times$ that of MONICA) provided much deeper exposures. The larger format ($0.0350''$ pixels giving a field of $36'' \times 36''$) also included either the guide-star or some other stars suitable for PSF analysis.

For the observations reported here the natural seeing was between $0.5''$

Table 5.7: Target List

		Position (J2000)		Guide-star	
Target	z	α	δ	Magnitude (R)	Offset ($''$)
3C 340	0.78	16:29:38.0	+23:20:38	14.9	11
3C 356	1.08	17:24:19.4	+50:57:36	15.0	16
3C 368	1.13	18:05:06.4	+11:01:32	14.8	46
3C 437	1.48	21:45:01.0	+15:06:36	14.3	45
3C 230	1.49	09:51:58.8	-00:01:27	14.7	4
3C 68.2	1.58	02:34:23.8	+31:34:17	14.2	14
3C 294	1.78	14:06:44.0	+34:11:25	11.7	9
TXS 0828+193	2.57	08:30:53.4	+19:13:16	12.7	38
4C +41.17	3.80	06:50:52.1	+41:30:31	14.1	24

and $0.9''$ with good transparency. We made observations primarily through standard H, and K filters. A few observations through standard J were also made. A K' filter would have been preferred because of the lower resultant sky-noise but none was available for our runs. We were unable to obtain any K data during the 1997 run due to problems with the filter-wheel assembly. Exposures of 300 s each were made in a non-repeating rectangular dither pattern with $1''$ steps for MONICA and $4''$ steps for KIR.

Due to the poor sensitivity of MONICA only 2 of the 5 objects observed in June 1997 had $S/N > 5$ for the RG. A lower S/N is insufficient for the purpose of detecting substructure in the RG and these objects will not be discussed further. The two targets with good S/N (3C 356 and 3C 368) had total exposures of over 10^4 s. The large offset needed to reach 3C 368, however, provided very poor correction ($> 0.45''$ FWHM), also insufficient to resolve substructure, and it too was omitted from the analysis. Only the H-band image of 3C 356 had both sufficient S/N and PSF correction to be

Table 5.8: CFHT AOB Journal of Observations

Target	Date	Camera	Exposure time (s)		
			J	*H*	*K*
3C 340	16 June 1997	MONICA	-	4800	-
3C 356	14, 15, 16 June 1997	MONICA	3600	14400	-
3C 368	14, 15 June 1997	MONICA	9600	4800	-
3C 437	16 June 1997	MONICA	4800	4800	-
3C 294	14 June 1997	MONICA	-	9600	-
3C 230	17 January 1998	KIR	-	1200	3600
3C 68.2	17, 18 January 1998	KIR	-	2400	4800
3C 294	18 January 1998	KIR	-	2400	4800
TXS 0828+193	17 January 1998	KIR	3600	1200	6000
4C +41.17	18 January 1998	KIR	1200	3600	10800

included in the sample.

Much better results were obtained in January 1998 with KIR. All of the images with the exception of the *J* image of 4C +41.17 provided good *S/N*. The correction in all of the images was consistently better than 0.3″ FWHM with the exception of the *J* and *H* images of TXS 0828+193 (at a large guide-star offset of 38″). These last two, with 0.45″ FWHM and 0.35″ FWHM respectively, are considered marginal but were not excluded from the sample. Thus the final sample consisted of 6 fields with imaging in both *H* and *K* (with the exception of 3C 356 with no *K* image) and one *J* image of TXS 0828+193.

5.4 Archival Space-Telescope Images

As discussed in Section 5.1, our targets were, in part, selected based on the availability of archival HST WFPC2 data. These data were obtained

Table 5.9: HST WFPC2 Archival Data

	Exposure time (s)			
Target	F675W	F702W	F785LP	F814W
3C 356	-	600	-	1700
3C 230	-	560	-	-
3C 68.2	-	600	3400	-
3C 294	-	1120	-	-
TXS 0828+193	4000	-	-	-
4C +41.17	-	21600	-	-

through the Canadian Astronomy Data Centre (CADC) which is operated by the National Research Council of Canada (NRC) Herzberg Institute of Astrophysics (HIA). They were processed in a similar manner to the globular cluster data. The archival images were combined using standard Space Telescope Science-Database Analysis System (STSDAS) tasks and rotated to the proper orientation based on information contained in the image headers.

5.5 Combined Dataset

In all cases the MONICA or KIR data were resampled to match the pixel sampling of the WFPC2 data.

For both the WFPC2 and KIR images the PSF FHWM at the galaxy position was determined by measuring a bright but unsaturated star in the field. For WFPC2 images this was the star nearest the RG and for KIR it was a star at a similar offset from the guide-star. In the case of 3C 294 no such PSF star was available and no guide-star calibration observations were

made but the galaxy is within 9″ of a $V = 12$ magnitude star. The target PSF was established from the calibration observations of NGC 4147, also observed with a $V = 12$ guide-star (see Figures 5.2 and 5.7). For MONICA no PSF star was available due to its small FOV. However, for the MONICA observations exposures of the guide-star were available. These were taken immediately before each set of galaxy exposures and were combined to determine an average on-axis PSF. The PSF reconstruction technique of Véran et al (1996) was also employed to determine an on-axis PSF and this agreed with the observed one. The PSF at the target position was then determined using the task OFFAXIS and the PSF reconstruction map from 16 June 1997. The results are presented in Table 5.10.

The per-pixel S/N for bright knots within the RGs is approximately 10 for both the CFHT and HST data. For the fainter knots and potential RG companions this drops to $S/N \approx 3$. As a final step the CFHT and HST data were combined for each target in order to create an image with the total flux of all available bands. This increased the S/N in the final image which was helpful in locating faint RG companions in the fields.

In the remainder of the analysis the HST WFPC2 F675W and F702W filters are assumed to be approximately equivalent to R and the F785LP and F814W filters also roughly equivalent to I. Only a first order transformation from the local to standard Johnson filter set has been made for these and the CFHT data (Tables 5.2 and 5.3).

Table 5.10: Image Resolution

	FWHM (″)				
Target	*R*	*I*	*J*	*H*	*K*
3C 356	0.21	0.21	-	0.21	-
3C 230	0.20	-	-	0.24	0.24
3C 68.2	0.21	0.21	-	0.23	0.26
3C 294	0.21	-	-	0.21	0.24
TXS 0828+193	0.23	-	0.45	0.35	0.27
4C +41.17	0.23	-	-	0.25	0.29

5.6 Photometry

The composite image of all the data for a particular target was searched by eye to find stars, knots, and faint objects in the field. Also, individual images for the different bands were examined to ensure that no objects were missed. Finally, the software package SExtractor (Bertin and Arnouts 1996) was used to find objects in the field but it was determined that this generally selected the same objects as those found by eye. Coordinate lists of objects in the fields were generated and synthetic aperture photometry was performed for all of these objects in the CFHT and HST images.

The IRAF task APPHOT was used employing a 3.0″ aperture on all objects in the field. This aperture was large enough to encircle all the flux for each of the targets. For the RGs themselves rectangular apertures were determined that separated the individual knots without overlap. This was always done in the restframe visible band for each galaxy (see Section 5.8) and the same apertures were maintained for the other bands. The dividing line between apertures was determined by the procedure that will be discussed

Table 5.11: Galactic Extinction

	Extinction (magnitudes)				
Target	*R*	*I*	*J*	*H*	*K*
3C 356	0.140	0.063	-	0.019	-
3C 230	0.210	-	-	0.046	0.029
3C 68.2	0.376	0.273	-	0.081	0.052
3C 294	0.038	-	-	0.008	0.005
TXS 0828+193	0.093	-	0.031	0.020	0.013
4C +41.17	0.348	-	-	0.075	0.048

in Section 6.2.1 (the '50% rule'). The quoted 1-σ photometric errors are due to Poisson statistics from sky-flux. In some cases the formal errors were somewhat less than 0.1 magnitude but uncertainties in flatfielding, extinction, and photometric zero-points suggest a lower limit on the photometric uncertainty of 0.1 magnitude.

Each RG field was corrected for galactic extinction with values from the extinction map of Schlegel et al. (1998); see Table 5.11. Again, the HST WFPC2 F675W and F702W filters are assumed to be approximately equivalent to *R* and the F785LP and F814W filters also roughly equivalent to *I*.

5.7 Projected Physical Size of Fields

The imaged fields are not identical in FOV. Also, the redshifts of the targets are different. This means the volume of space sampled at each redshift by projecting it into 2 dimensions differs for each target. This difference is not great, however, and a simple correction for the true projected area was calcu-

lated from Equation 2.4. Thus the number of detected objects in each field is corrected to give the number of objects per 0.01 Mpc^2. This relationship will also serve to determine the projected physical distances between the various components of the RG.

5.8 Restframe Bandpasses

Along with a description of the physical scale at each redshift we must also consider the changing bandpass of restframe light sampled by a given filter on the telescope. Roughly the same restframe bandpass should be sampled for each RG in order to compare carefully any differences in morphology with redshift. Otherwise, any difference may simply be due to, say, observing one galaxy longward and one shortward of the 4000 Angstrom break. It is, however, possible to provide a straightforward comparison of deep imaging in 3 restframe 'bandpasses' for our sample. One is an ultraviolet (UV) band from 1000 to 4000 Angstroms, another is visible light from 4000 to 7000 Angstroms, and a third is a near-infrared (NIR) band from 7000 to 10000 Angstroms (see Figure 6.1). This is possible because the longest total integrations for the targets at $z < 3$ were, typically, through R and H filters. The longest NIR integrations for the only $z > 3$ target, 4C +41.17, were taken through a K filter. A minor exception to our bandpass divisions is presented by 3C 356 since the central wavelength of I falls at 3913 Angstroms in its restframe; slightly below the cutoff for our 'visible' band. This is acceptable because the R-band central restframe wavelength is 3375 Angstroms - well into our 'UV' band.

Another consideration is emission-line contamination of the broadband

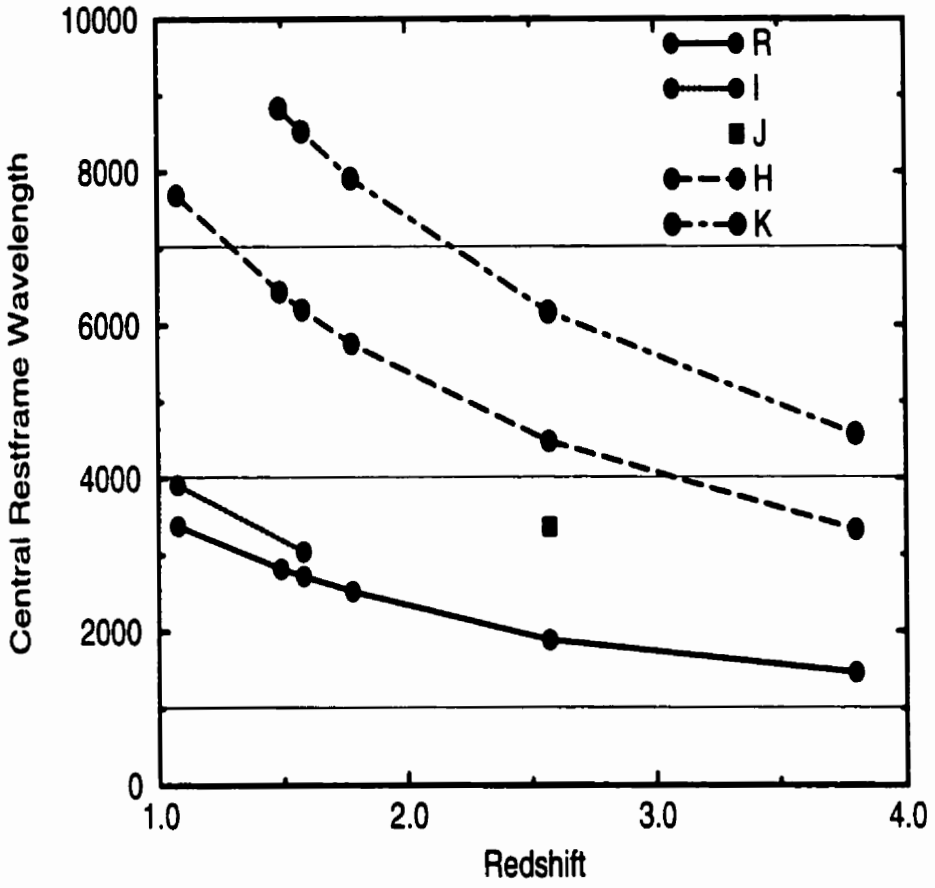

Figure 5.9: A plot of the shifting observed bandpasses in our dataset. These define 3 broad restframe 'bandpasses' for our sample. One is a UV band from 1000 to 4000 Angstroms, another is visible light from 4000 to 7000 Angstroms, and a third is a NIR band from 7000 to 10000 Angstroms. The convention used here to denote the different observed passbands will be maintained throughout the rest of the text.

Table 5.12: Emission Line Contamination

	Contamination (%)				
Target	*R*	*I*	*J*	*H*	*K*
3C 356	-	18[c]	-	-	-
3C 230	-	-	-	13[d]	-
3C 68.2	-	7[c]	-	14[d]	-
3C 294	-	-	-	-	-
TXS 0828+193	5[a]	-	-	-	17[d]
4C +41.17	15[b]	-	-	-	-

[a] CIII]; Pentericci et al. (1999)
[b] SiIV, CIV; Dey et al. (1997)
[c] [NeV], [OII], [NeIII]; Best et al. (2000)
[d] Hα

fluxes. These emission lines are the products of ionization by the hidden AGN and it is important to know if they will seriously interfere with what should be measurements of stellar continuum light. The following are strong lines redshifted into the observed bandpasses: H$\alpha\lambda$6563, [NeIII]λ3869, [NeV]λ3426 [OII]λ3727, CIII]λ1909, CIVλ1549, and SiIVλ1403. If a spectrum was available the contamination was estimated by comparing the FWHM of the filter bandpass and the equivalent width of the emission lines. No spectra of the targets were available for NIR wavelengths so the equivalent widths here were estimated from a photoionization calculation carried out by McCarthy (1993). This calculation uses the CLOUDY model of Ferland and Osterbrock (1986) to predict accurately a composite RG spectrum constructed from observations of galaxies with $0.1 < z < 3$. The results are given in Table 5.12. The contamination is always less than 20% so it is not expected that this will have a significant effect on the photometric results.

5.9 Descriptions of Each Field

The HST and CFHT images follow, along with photometry for each field. First, the composite of all data is given. This is an image that shows a region of contiguous coverage in all bandpasses. Artifacts and scattered light from bright stars (ghost images) are indicated by an 'A'. Stars are indicated by an 'S', the guide-star by 'GS', and the calibration star by 'PSF'. All detected extended objects of similar brightness to the RG or fainter are indicated by a number. Some well-resolved galaxies brighter than the RG were detected and these are indicated by 'FG' for foreground galaxy. The RG itself is denoted by 'RG' with other objects believed to be associated with the RG denoted by an upper-case letter in brackets. When a component is considered to be at the same redshift as the RG its absolute H magnitude is quoted assuming $H_0 = 70$ km s^{-1} Mpc^{-1} and $q_0 = 0.5$. The peaks of emission of the radio lobes are denoted by 'X's.

For each enlarged field showing the RG itself the labelling of individual sub-components is done in the restframe visible band discussed in Section 5.7. Each field is $4'' \times 4''$ with north up and east left.

Detailed discussion of determination of companions as well as sub-structure in the RGs will follow in Chapter 6.

5.9.1 3C 356

This is a $z = 1.08$ radio bright (11.3 Jy at 178 MHz) RG that has a very extended double radio lobe morphology. The projected separation of the lobes is just over an arcminute or about 250 kpc in physical size (the axis of the radio lobes is denoted by the solid lines in Figure 5.10). There are

also two unresolved radio sources located roughly midway along the radio axis. These correspond to the two brightest components - RG and C - in the optical imaging (see Figure 5.10).

The northern object is brightest in the WFPC2 images but it is not clear if it is the host galaxy of the radio source. High-resolution (0.18″ FWHM) radio observations have been obtained at 8.4 GHz by Best et al. (1997) and at 5.0 GHz by Fernini et al. (1993) using the Very Large Array (VLA). Best et al. (1997) have compared these radio maps to the same WFPC2 data discussed here. The positions of the radio sources quoted here are from their astrometry - based on registration of the bright radio cores to the peaks of the optical emission. At 8.4 GHz the southeastern component centred on C, is actually brighter (flux density 0.95 mJy) than the northern component (0.22 mJy), centered on knot a of the RG (see Figure 5.10). The northern radio source has the steep spectral index ($\alpha \approx 1.1$ from 8.4 GHz to 5 GHz) typical of compact steep spectrum sources while the southeastern source is flatter ($\alpha \approx 0.1$) (Best et al. 1997).

The best previous NIR imaging was obtained through non-AO ground-based observations using UKIRT (Best et al. 1997). Both components were unresolved. These two objects are resolved in our NIR imaging and have about the same brightness. See Table 5.13 for the photometry of images given in Figures 5.10 and 5.11.

The morphology of the northern object in the *H* image is more typically that of the RGs of the 3C Catalogue so it is assumed here that it is the AGN host. Figure 5.10 shows the RG to be extended in the direction of knot b 0.5″ to the northwest seen in the optical images. Object C is more diffuse

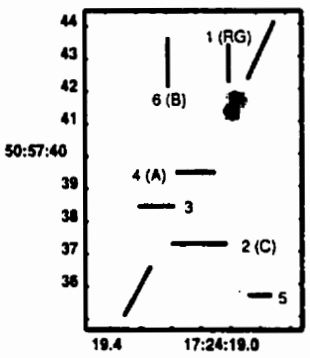

Figure 5.10: An image of the 3C 356 field. This is the co-addition of all optical and NIR data. See text for details.

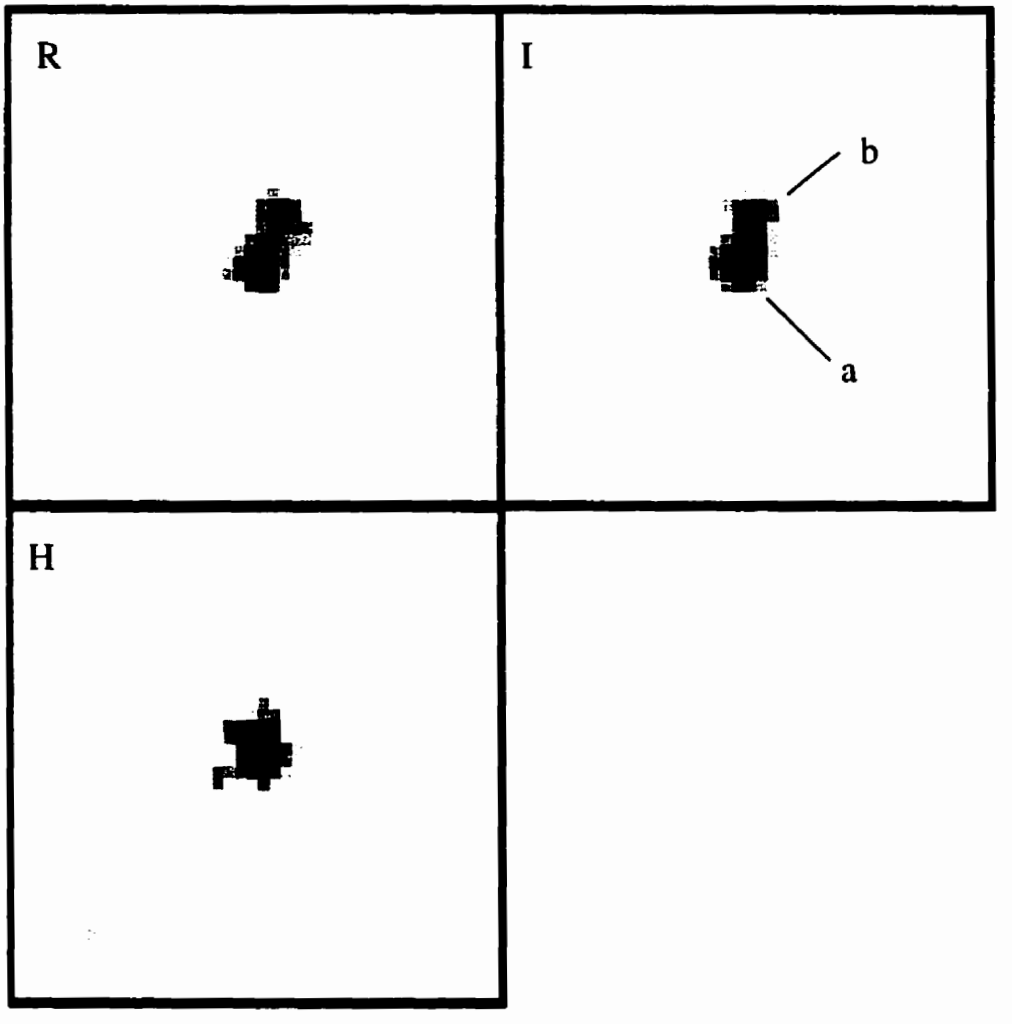

Figure 5.11: Images of the RG in the 3C 356 field. The FOV is 4″ × 4″ with north up and east left. See text for details.

Table 5.13: Photometry of 3C 356

Object	R	I	H	$R-I$	$I-H$	M_H
1 (RG)	20.9 ± 0.2	19.9 ± 0.1	17.5 ± 0.2	1.0 ± 0.3	2.4 ± 0.3	-26.3 ± 0.2
(a)	21.2 ± 0.2	20.4 ± 0.1	17.6 ± 0.2	0.8 ± 0.3	2.8 ± 0.3	-26.2 ± 0.2
(b)	22.1 ± 0.3	21.1 ± 0.2	18.8 ± 0.5	1.0 ± 0.5	2.3 ± 0.7	-25.0 ± 0.5
2 (C)	21.5 ± 0.3	21.3 ± 0.2	17.4 ± 0.2	0.2 ± 0.5	3.9 ± 0.4	-26.4 ± 0.2
4 (A)	-	22.4 ± 0.4	-	-	-	-
5	24.1 ± 1.5	-	-	-	-	-
6 (B)	24.0 ± 1.5	22.7 ± 0.6	-	1.3 ± 2.1	-	-

and extended in both the optical and NIR. There are several other objects visible in the field. The extended emission to the south of the RG (labelled A) appears in both the R and I images but not in our H image. The colour of A is similar to another object to the northeast of the RG (B) which also does not appear in the H image.

Keck Telescope optical spectropolarimetry by Cimatti et al. (1997) reveals that both components are polarized in restframe UV (observed 4000-9000 Angstroms) with $P \approx 8\%$ and an electric vector approximately orthogonal to the radio axis (Figure 5.12). This continuum polarization rises towards the blue, reaching $P \approx 15\%$ for the northern component. A broad and strongly polarized MgIIλ2800 emission line ($P = 6.8 \pm 1.2\%$ continuum subtracted) is observed in the northern component as well as numerous *unpolarized* narrow emission lines (e.g., $P = 1.8 \pm 0.7\%$ [OII]). The MgII line is also seen as a narrow line in unpolarized light. Observations with the UKIRT by Leyshon and Eales (1998) show that both components are also probably polarized in restframe visible light (observed K-band) at the 10% level as well. These observations suggest an obscured AGN as a likely source of scat-

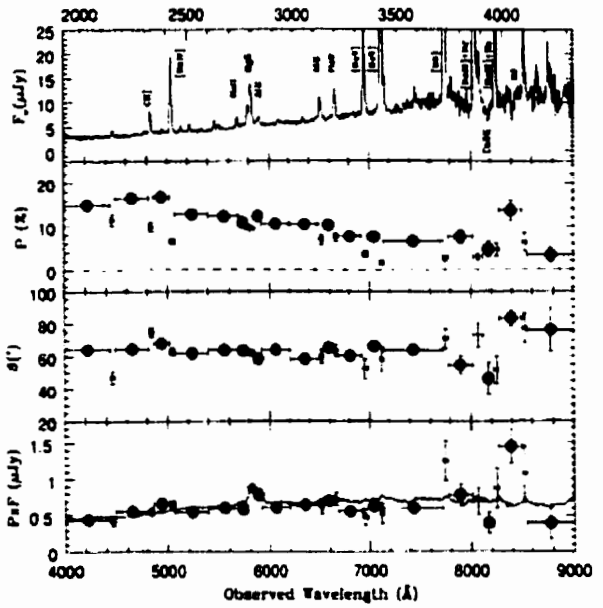

Figure 5.12: Deep Keck Telescope optical spectropolarimetric observations of 3C 356 taken from Cimatti et al. (1997).

tered non-stellar light. The broad polarized MgII emission is as expected for an obscured quasar nucleus within a narrow-line RG. Since MgII is also seen in unpolarized light Cimatti et al. (1997) estimate (by comparing the equivalent widths) that nonstellar radiation contributes perhaps as much as 80% of the total flux in the UV. This certainly suggests that there might be pollution of our R-band photometry with AGN light.

This field has been observed in X-rays by Crawford and Fabian (1993) using the Roentgen Satellite (ROSAT). The emission is extended over a region 0.5 Mpc long roughly aligned with the radio axis. Deep follow up observations at higher resolution by the same authors detected no point sources at either of the potential RG hosts (Crawford and Fabian 1996). Based on this, they suggest that the source of the emission cannot be from the AGN or a jet-cloud interaction but, rather, originates from the intracluster medium itself (the most distant yet detected in X-rays). This seems to confirm the interpretation that HzRGs reside in cluster environments. By scaling the X-ray luminosity to that of nearby clusters Crawford and Fabian (1996) suggest 3C 356 could reside in a moderately rich cluster like Virgo.

5.9.2 3C 230

This is a $z = 1.487$ radio-bright (19.2 Jy at 178 MHz) RG. Rhee et al. (1996) obtained VLA radio observations of 3C 230 at 8.4 GHz and 4.8 GHz. No core object was detected but the positions of the peaks of the radio lobes from these moderate resolution (0.4″ FWHM) maps are marked as Xs in Figure 5.13.

Previous attempts to obtain ground-based NIR imaging of this field were

Table 5.14: Photometry of 3C 230

Object	R	H	K	$R-H$	$H-K$	M_H
1 (RG)	21.2 ± 0.1	17.7 ± 0.1	17.5 ± 0.1	3.5 ± 0.2	0.2 ± 0.2	-26.7 ± 0.1
(a)	21.2 ± 0.1	17.8 ± 0.1	17.4 ± 0.1	3.4 ± 0.2	0.4 ± 0.2	-26.6 ± 0.1
(b)	22.7 ± 0.5	19.2 ± 0.3	19.0 ± 0.4	3.5 ± 0.8	0.2 ± 0.7	-25.2 ± 0.3
(c)	22.7 ± 0.5	19.2 ± 0.3	19.4 ± 0.5	3.5 ± 0.8	-0.2 ± 0.8	-25.2 ± 0.3
2	-	20.0 ± 0.6	18.2 ± 0.3	-	1.8 ± 0.9	-
3 (A)	23.2 ± 0.8	19.2 ± 0.3	18.4 ± 0.3	4.0 ± 1.1	0.8 ± 0.6	-25.2 ± 0.3
4	21.7 ± 0.2	19.2 ± 0.3	18.7 ± 0.4	2.5 ± 0.5	0.5 ± 0.7	-
5	-	19.1 ± 0.3	17.7 ± 0.2	-	1.4 ± 0.5	-
6 (B)	21.5 ± 0.2	18.2 ± 0.1	17.7 ± 0.2	3.3 ± 0.3	0.5 ± 0.3	-26.2 ± 0.1
7	20.3 ± 0.1	17.6 ± 0.1	17.0 ± 0.1	2.7 ± 0.2	0.6 ± 0.2	-
8	21.1 ± 0.1	17.6 ± 0.1	17.2 ± 0.1	3.5 ± 0.2	0.4 ± 0.2	-
9 (C)	22.6 ± 0.5	18.8 ± 0.2	18.6 ± 0.4	3.8 ± 0.7	0.2 ± 0.6	-25.6 ± 0.2

hampered due to the proximity of the bright ($R = 14.7$) star 4″ to the west. This star provided an excellent guide for AO observations and the H and K images are shown in Figure 5.14 along with the HST R-image.

Several other objects are detected in the field. Objects 7 and 8 are brighter than the RG and are probably foreground galaxies. No knots are detected at the positions of the radio lobes but the faint extended objects denoted by A, B, and C have colours similar to the RG. The RG itself is composed of 3 knots in our H band image. Interestingly, the fainter central region of the RG in R (southeast of knot a) is also the location of the brightest component in H (the filter for which apertures were selected - see Section 5.6). This is especially apparent in the K image and is perhaps due to obscuration by dust in the galaxy. See Table 5.13 for the photometry of images shown in Figures 5.13 and 5.14.

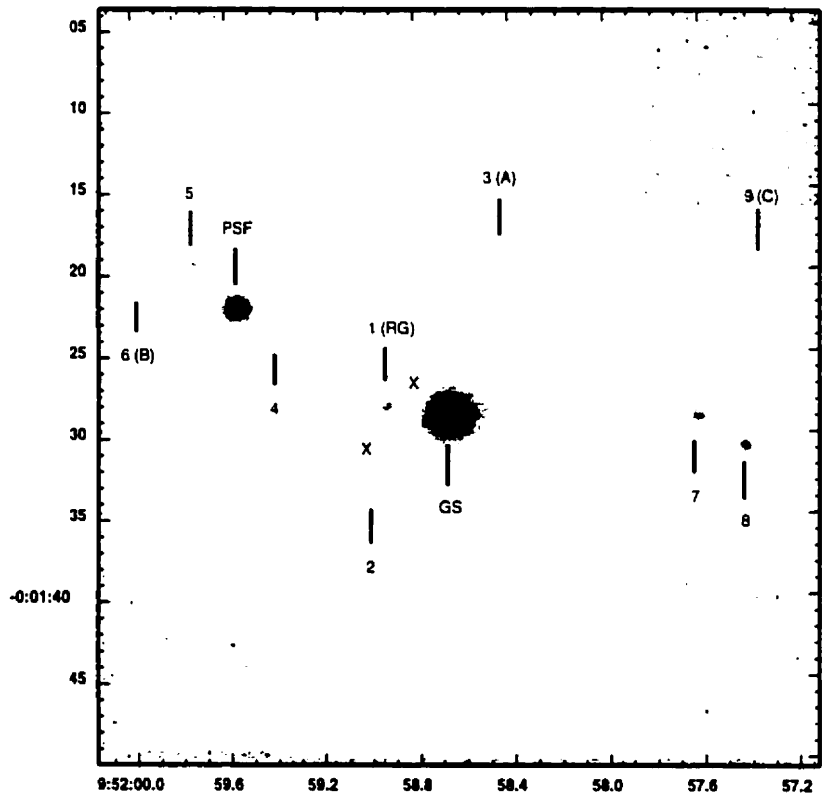

Figure 5.13: An image of the 3C 230 field. This is the co-addition of all optical and NIR data. See text for details.

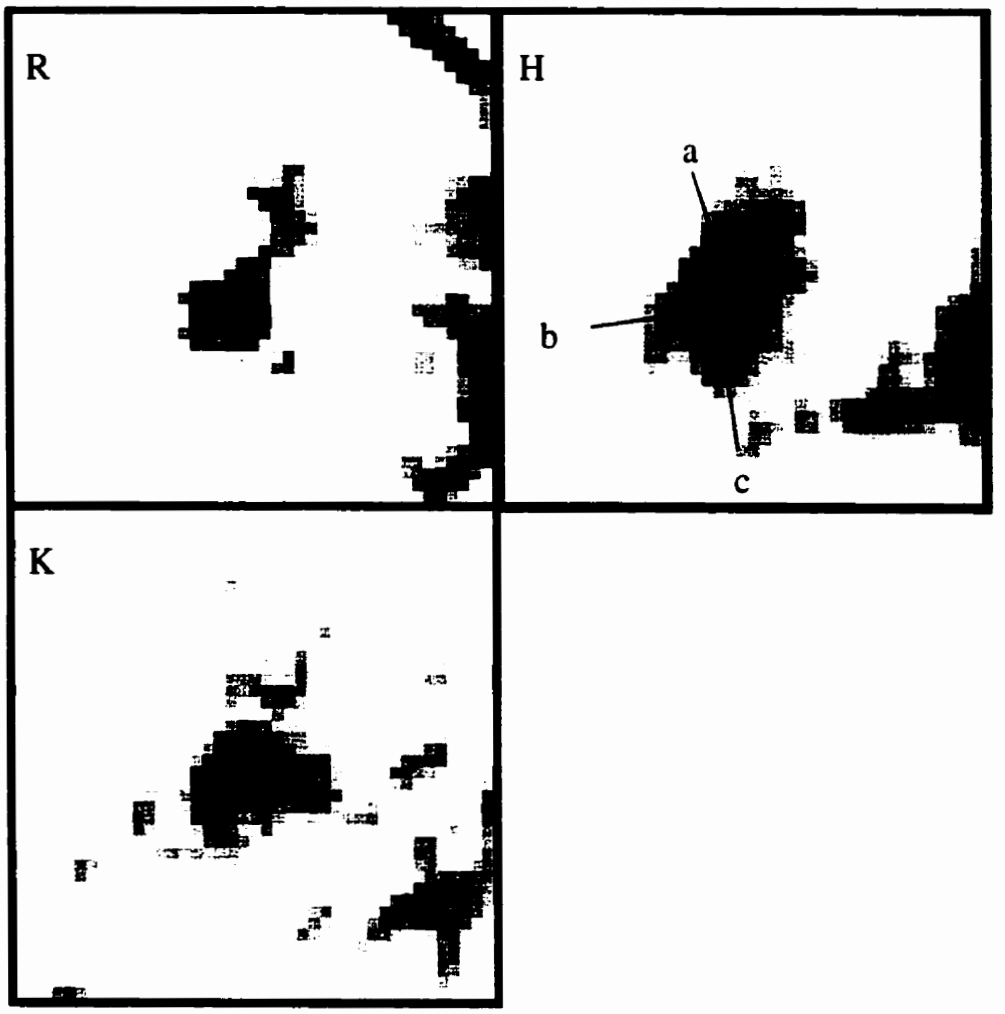

Figure 5.14: Images of the RG in the 3C 230 field. The FOV is 4″ × 4″ with north up and east left. See text for details.

5.9.3 3C 68.2

This is a radio bright (10.0 Jy at 178 MHz) RG at $z = 1.575$. A high resolution (0.18″ FWHM) VLA radio map at 8.4 GHz was obtained by Best et al. (1997). The radio emission has the classic extended double lobed morphology with an axis running roughly southeast to northwest. No core is detected to a 3-σ flux limit of 0.13 mJy.

The combined visible and NIR data (Figure 5.15) shows that the galaxy is extended and misaligned with the radio axis by about 30 degrees. Several other objects are detected in the field. Component A is within 2″ of the southern radio hotspot based on astrometry from Best et al. (1997) using the same WFPC2 data discussed here. Component B is more diffuse and also lies roughly along the axis of the radio emission. The photometry can be found in Table 5.15. The RG itself is composed of 2 knots separated by 0.5″ - denoted by a and b - in the H image. A third faint knot another 0.5″ to the south is apparent in the I image.

5.9.4 3C 294

This is a $z = 1.78$ radio bright (10.0 Jy at 178 MHz) RG with a double lobed morphology along an axis from northeast to southwest. A moderate resolution (0.4″ FWHM) VLA map at 5.0 GHz has been obtained by McCarthy et al. (1990) and the peaks of the radio lobes are marked in Figure 5.17. The astrometry is based on registration of the guide-star in our K image with their radio map and corresponding Kitt Peak National Observatory (KPNO) 4 m K image.

The combined visible and NIR image is given in Figure 5.17. The RG is

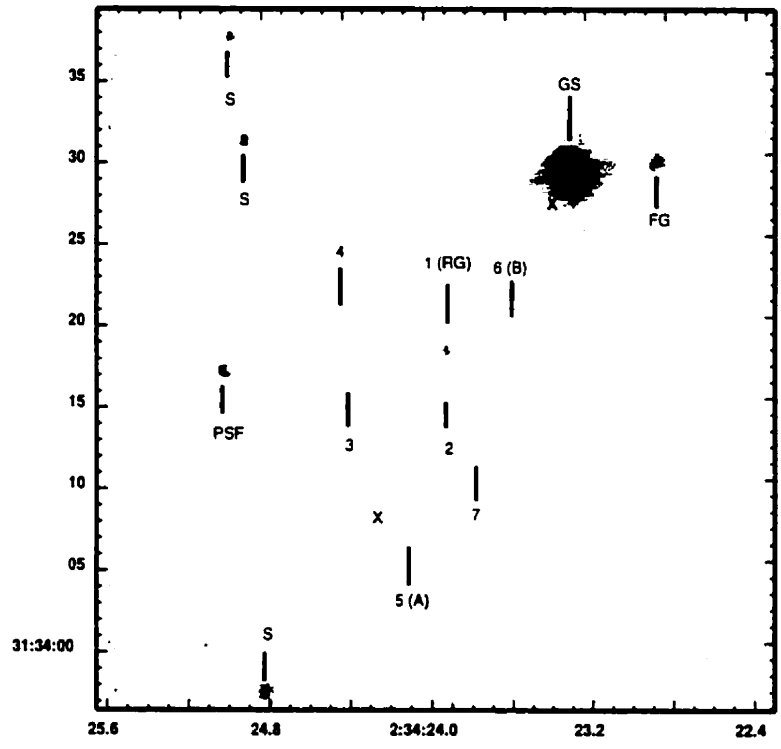

Figure 5.15: An image of the 3C 68.2 field. This is the co-addition of all optical and NIR data. See text for details.

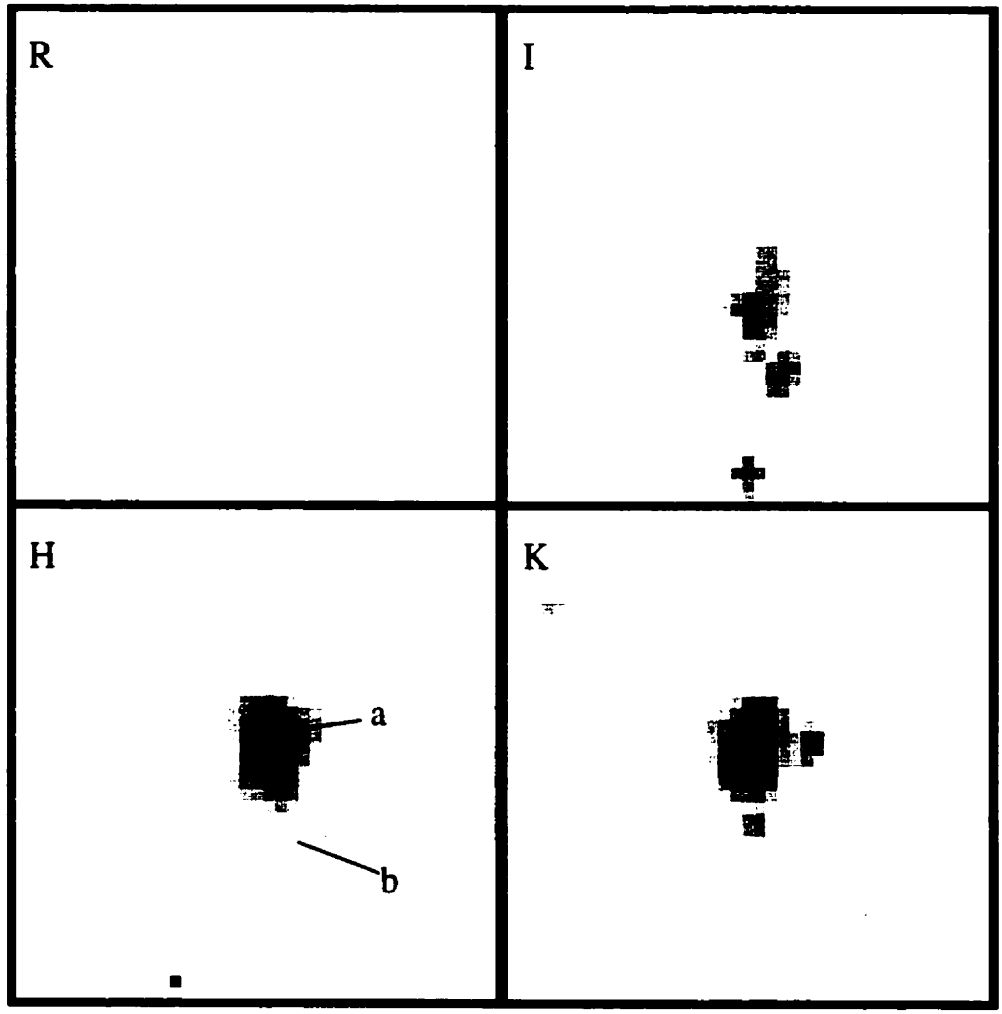

Figure 5.16: Images of the RG in the 3C 68.2 field. The FOV is 4″ × 4″ with north up and east left. See text for details.

Table 5.15: Photometry of 3C 68.2

Object	R	I	H	K	$R-I$	$R-H$	$I-H$	$H-K$	M_H
1 (RG)	22.1 ± 0.2	21.9 ± 0.2	18.2 ± 0.1	17.5 ± 0.1	0.2 ± 0.4	3.9 ± 0.3	3.7 ± 0.3	0.7 ± 0.2	-26.5 ± 0.1
(a)	22.2 ± 0.2	21.8 ± 0.2	18.4 ± 0.1	17.7 ± 0.1	0.4 ± 0.4	3.8 ± 0.3	3.4 ± 0.3	0.9 ± 0.2	-26.3 ± 0.1
(b)	22.9 ± 0.3	22.4 ± 0.3	20.5 ± 0.5	19.6 ± 0.8	0.5 ± 0.6	2.4 ± 0.8	1.9 ± 0.8	0.9 ± 1.3	-24.2 ± 0.5
2	22.8 ± 0.3	22.7 ± 0.4	20.8 ± 0.6	18.9 ± 0.5	0.1 ± 0.7	2.0 ± 0.9	1.9 ± 1.0	1.9 ± 1.1	-
3	21.9 ± 0.1	21.1 ± 0.1	19.5 ± 0.2	18.0 ± 0.2	0.8 ± 0.2	2.4 ± 0.3	1.6 ± 0.3	1.5 ± 0.4	-
4	-	22.3 ± 0.3	20.1 ± 0.3	-	-	-	2.2 ± 0.6	-	-
5 (A)	22.0 ± 0.1	21.7 ± 0.1	19.6 ± 0.2	19.0 ± 0.6	0.3 ± 0.2	2.4 ± 0.3	2.1 ± 0.3	0.6 ± 0.8	-25.1 ± 0.2
6 (B)	22.8 ± 0.3	22.2 ± 0.2	19.4 ± 0.2	19.1 ± 0.6	0.6 ± 0.5	3.4 ± 0.5	2.8 ± 0.4	0.3 ± 0.8	-25.3 ± 0.2
7	-	22.5 ± 0.3	19.3 ± 0.2	18.3 ± 0.3	-	-	3.2 ± 0.5	1.0 ± 0.5	-

in the centre of the field. The two other bright objects in the northeast seem to be positioned along the axis of the radio emission although they are far outside the northeastern radio lobe. The photometry is given in Table 5.15; the colours of these objects are similar to those of the RG.

Previous attempts to obtain NIR images of the RG have been hampered by the bright ($R = 12$) star 9″ to the west. This proximity was an asset for our imaging. The structures seen in the H and K images of the RG itself (Figure 5.18) are not aligned with the radio axis. The main component is elongated along a north-south axis with a companion about 2″ to the east of the southern tip. The unresolved core (flux density 0.56 mJy) from the McCarthy et al. (1990) 5.0 GHz radio map does not correspond directly with any of the knots in our images. It is at a position 0.7″ due south of the peak of knot b. The uncertainty in this position is about 0.2″. This is because in this case the guide-star is double with a separation of 0.13″ and the positional error quoted by McCarthy et al. (1990) for their radio map is 0.05″.

The WFPC2 image had previously been viewed as a nondetection. With the position of the galaxy now known in the NIR it is possible that the visible counterpart in the WFPC2 image is discernible. This is the faint nebulosity partially obscured by the diffraction spike of the star seen in Figure 5.18. Other AO observations of 3C 294 were obtained by Stockton et al. (1999) using the University of Hawaii AO system on CFHT. Their K' image is of comparable depth and shows the RG to be very similar to our K image.

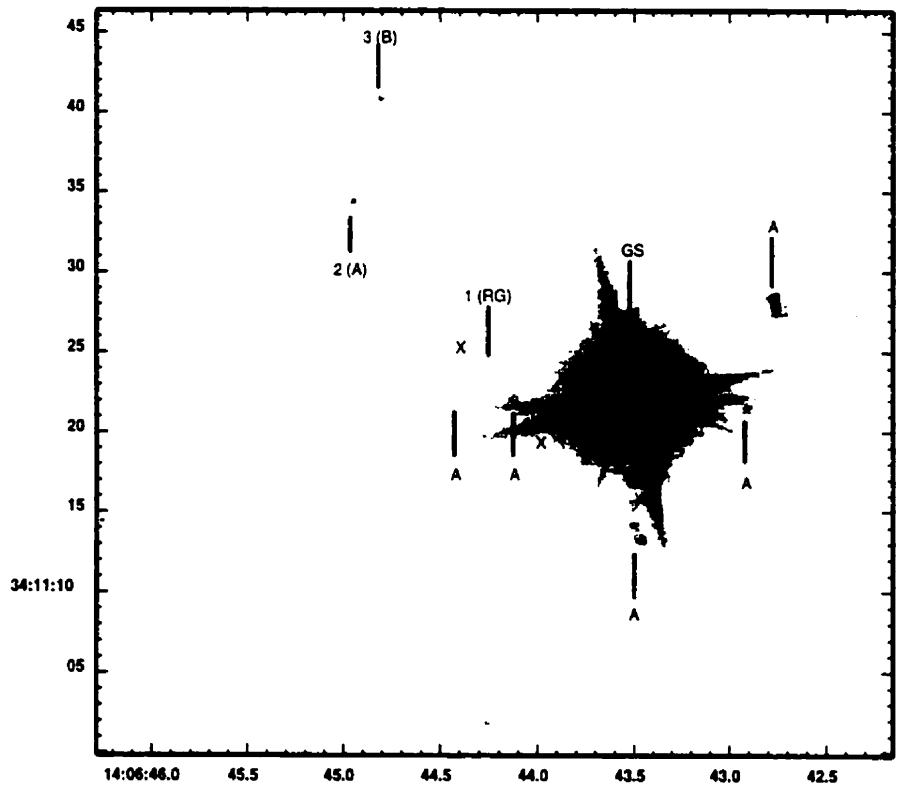

Figure 5.17: An image of the 3C 294 field. This is the co-addition of all optical and NIR data. See text for details.

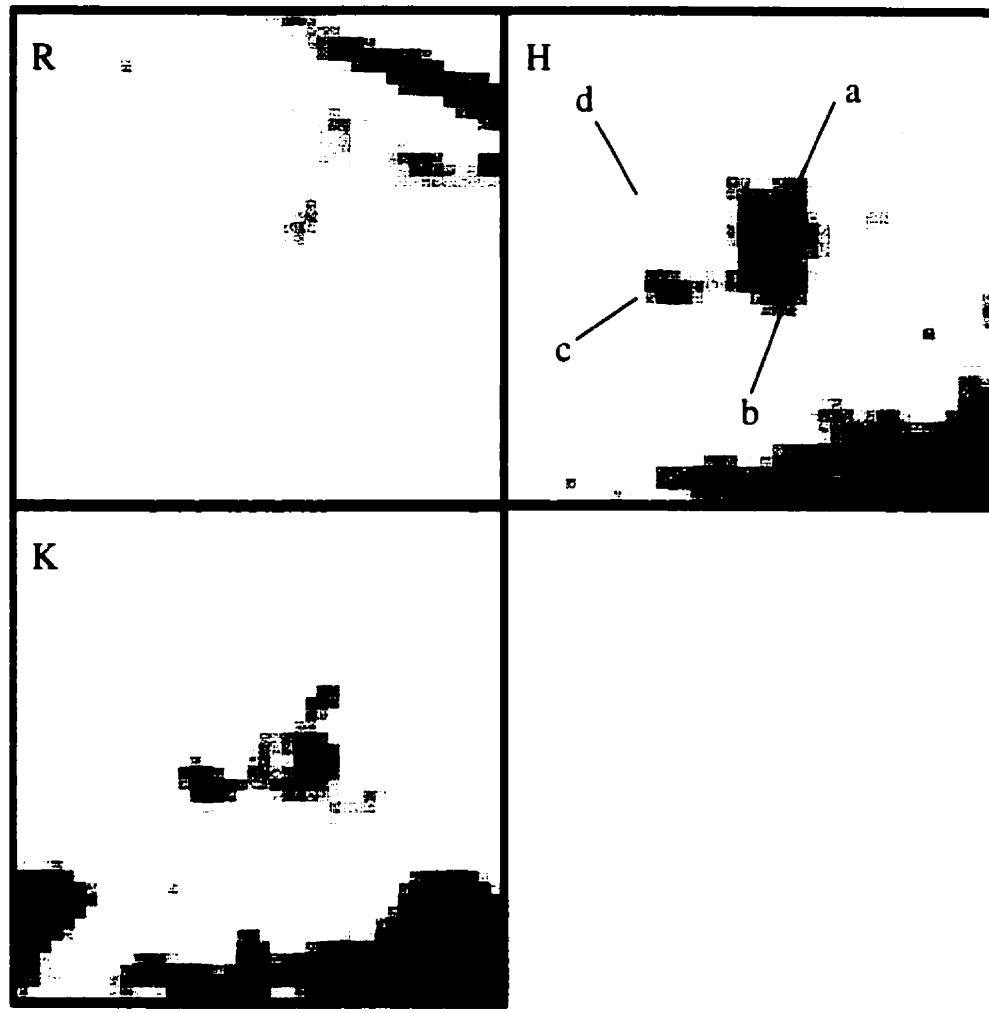

Figure 5.18: Images of the RG in the 3C 294 field. The FOV is 4″ × 4″ with north up and east left. See text for details.

Table 5.16: Photometry of 3C 294

Object	R	H	K	$R-H$	$H-K$	M_H
1 (RG)	23.3 ± 0.8	18.6 ± 0.1	18.1 ± 0.3	4.7 ± 0.9	0.5 ± 0.4	-26.2 ± 0.1
(a)	23.4 ± 0.8	19.0 ± 0.1	18.7 ± 0.4	4.4 ± 0.9	0.3 ± 0.5	-25.8 ± 0.1
(b)	24.7 ± 0.9	19.5 ± 0.2	18.4 ± 0.4	5.2 ± 1.1	1.1 ± 0.6	-25.3 ± 0.2
(c)	-	20.2 ± 0.2	19.3 ± 0.8	-	0.9 ± 1.0	-24.6 ± 0.2
(d)	-	20.2 ± 0.2	20.2 ± 0.8	-	0.0 ± 1.0	-24.6 ± 0.2
2 (A)	23.9 ± 0.6	18.9 ± 0.1	18.3 ± 0.3	5.0 ± 0.7	0.6 ± 0.4	-25.9 ± 0.1
3 (B)	24.0 ± 0.6	19.1 ± 0.1	18.6 ± 0.4	4.9 ± 0.7	0.5 ± 0.5	-25.7 ± 0.1

5.9.5 TXS 0828+193

This is a radio bright (0.549 Jy at 365 MHz) RG at $z = 2.57$. Moderate resolution (1.5″ FWHM) VLA radio maps at 1.5 GHz by Röttgering et al. (1994) indicate that it has a double lobed morphology. No core is detected but the peaks of the lobes are indicated by Xs in Figure 5.19.

Apart from the RG, several objects are detected in the field. Components A and B to the north of the RG are misaligned with the radio axis. Component A is slightly extended towards the RG.

The RG itself is spectacular in both optical and NIR imaging (Figure 5.20). It is composed of 5 knots in our H image with corresponding knots in the R image. The brightest knot in the K image does not correspond exactly with the brightest emission in the other images. Since K corresponds roughly to restframe R for this redshift the bluer light may be supressed which might indicate internal reddening for this galaxy. See Table 5.17 for the photometry of images in Figures 5.19 and 5.20.

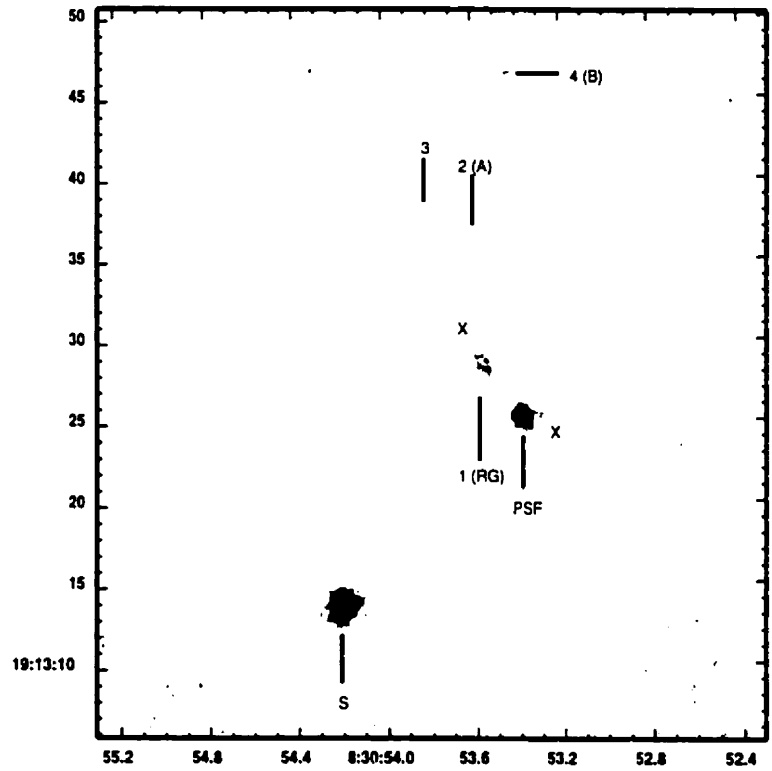

Figure 5.19: An image of the TXS 0828+193 field. This is the co-addition of all optical and NIR data. See text for details.

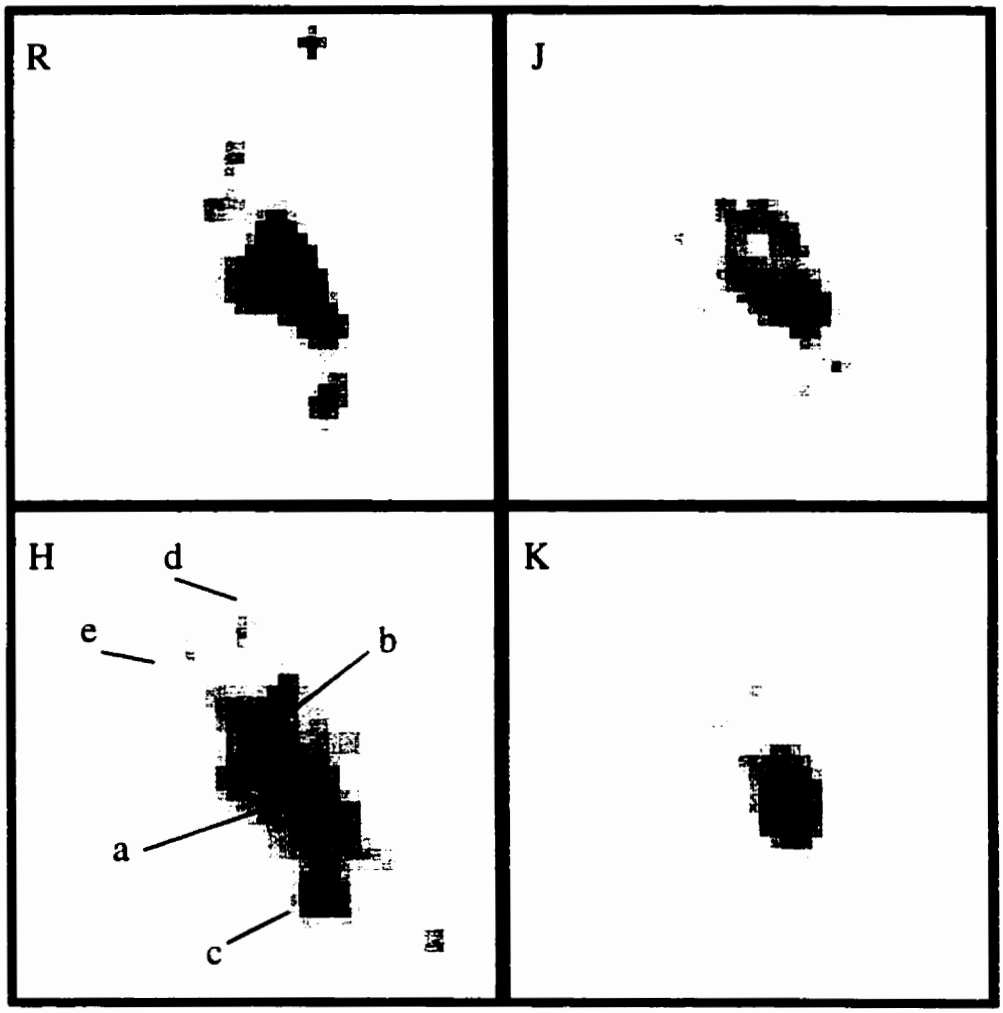

Figure 5.20: Images of the RG in the TXS 0828+193 field. The FOV is 4″ × 4″ with north up and east left. See text for details.

Table 5.17: Photometry of TXS 0828+193

Object	R	J	H	K	$R-H$	$J-H$	$H-K$	M_H
1 (RG)	22.4 ± 0.1	19.4 ± 0.1	17.9 ± 0.1	17.2 ± 0.1	4.5 ± 0.2	1.5 ± 0.2	0.7 ± 0.2	-27.9 ± 0.1
(a)	23.2 ± 0.1	20.0 ± 0.1	18.6 ± 0.1	17.7 ± 0.1	4.6 ± 0.2	1.4 ± 0.2	0.9 ± 0.2	-27.2 ± 0.1
(b)	23.5 ± 0.1	20.4 ± 0.1	18.9 ± 0.1	18.4 ± 0.2	4.6 ± 0.2	1.5 ± 0.2	0.5 ± 0.3	-26.9 ± 0.1
(c)	24.3 ± 0.2	21.2 ± 0.3	19.4 ± 0.3	19.4 ± 0.5	4.9 ± 0.5	1.8 ± 0.6	0.0 ± 0.8	-26.4 ± 0.3
(d)	24.5 ± 0.3	21.3 ± 0.3	20.2 ± 0.8	19.3 ± 0.4	4.3 ± 1.1	1.1 ± 1.1	0.9 ± 1.2	-25.6 ± 0.8
(e)	25.2 ± 0.6	21.8 ± 0.5	20.2 ± 0.8	19.9 ± 0.7	5.0 ± 1.4	1.6 ± 1.3	0.3 ± 1.5	-25.6 ± 0.8
2 (A)	23.9 ± 0.2	21.3 ± 0.3	19.6 ± 0.3	18.3 ± 0.2	4.3 ± 0.5	1.7 ± 0.6	1.3 ± 0.5	-26.2 ± 0.3
3	24.2 ± 0.2	22.1 ± 0.6	-	-	-	-	-	-
4 (B)	23.7 ± 0.1	20.4 ± 0.1	18.7 ± 0.1	18.0 ± 0.2	5.0 ± 0.2	1.7 ± 0.2	0.7 ± 0.3	-27.1 ± 0.1
5	24.6 ± 0.3	21.4 ± 0.3	21.3 ± 1.5	19.6 ± 0.6	3.3 ± 0.6	0.1 ± 1.8	1.7 ± 2.1	-
6	25.3 ± 0.6	22.0 ± 0.6	-	19.2 ± 0.4	-	-	-	-
7	25.9 ± 1.0	21.3 ± 0.3	-	-	-	-	-	-

5.9.6 4C +41.17

At $z = 3.80$ this is the highest-redshift object in the sample. Indeed it is one of the RGs with highest known redshift. It is a radio loud object with a 178 MHz flux of 2.7 Jy. Moderate resolution (1.2″ FWHM) VLA radio maps at 1.5 GHz, 4.9 GHz, and 15.0 GHz have been obtained by Chambers et al. (1996). The axis of the radio emission is roughly northeast to southwest and is double lobed. The lobes are marked as Xs in the total image of optical and NIR data (Figure 5.21). Two very faint objects are detected at positions roughly orthogonal to the radio axis to the south of the RG. The object closest to the RG is labelled A. and the southern object is labelled B.

The K image of the RG itself is very complex (see Figure 5.22). It is composed of 6 distinct structures which are compact knots. The morphology of the RG in R is less complicated and composed of 3 knots which do not exactly register with the knots in the K image. This is not surprising because, in the restframe, the 4000 Angstrom break separates R and K. Chambers et al. (1996) have compared the R-band HST data to their radio maps. A compact unresolved radio source roughly corresponds to a position 0.7″ west of the brightest emission in R. A second source approximately 6× fainter corresponds to a position 0.5″ south and 0.5″ west of component d. They quote an internal positional uncertainty of 0.5″ so it is possible that the radio sources correspond to the two optical knots. The photometry of the field is found in Table 5.18.

Using deep Keck Telescope spectropolarimetry observations Dey et al. (1997) find that the restframe UV continuum radiation is unpolarized (a 2-σ limit of $P < 2.4\%$). This suggests that scattered light from an obscured AGN

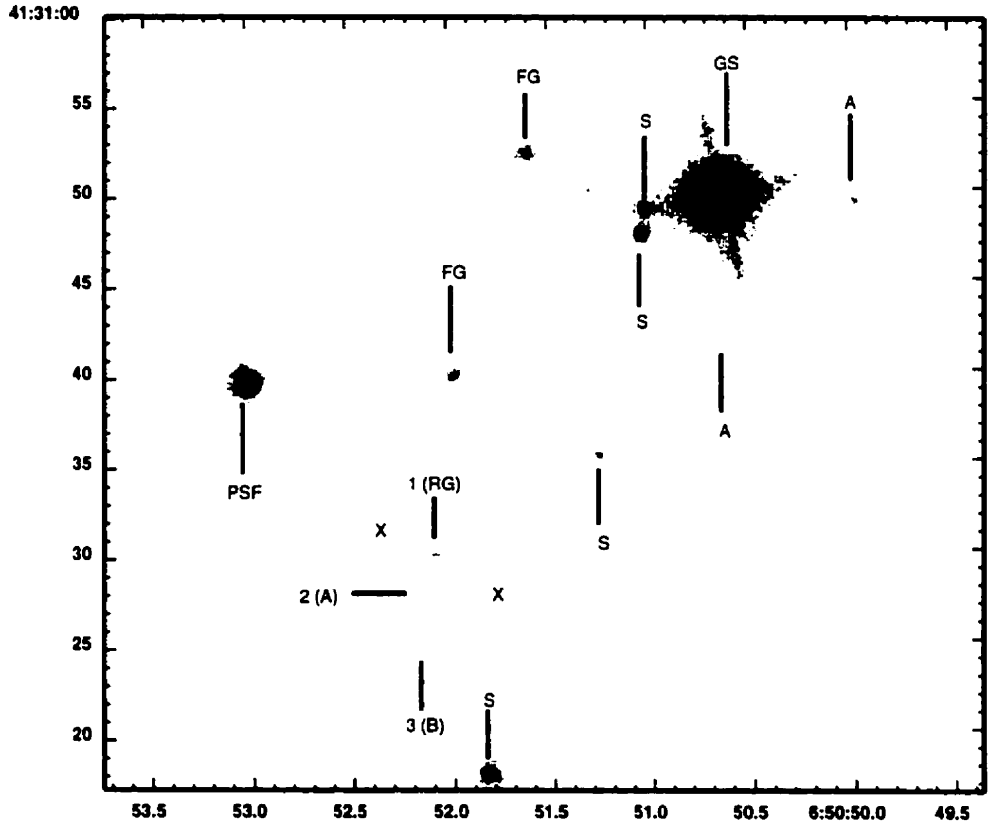

Figure 5.21: An image of the 4C +41.17 field. This is the co-addition of all optical and NIR data. See text for details.

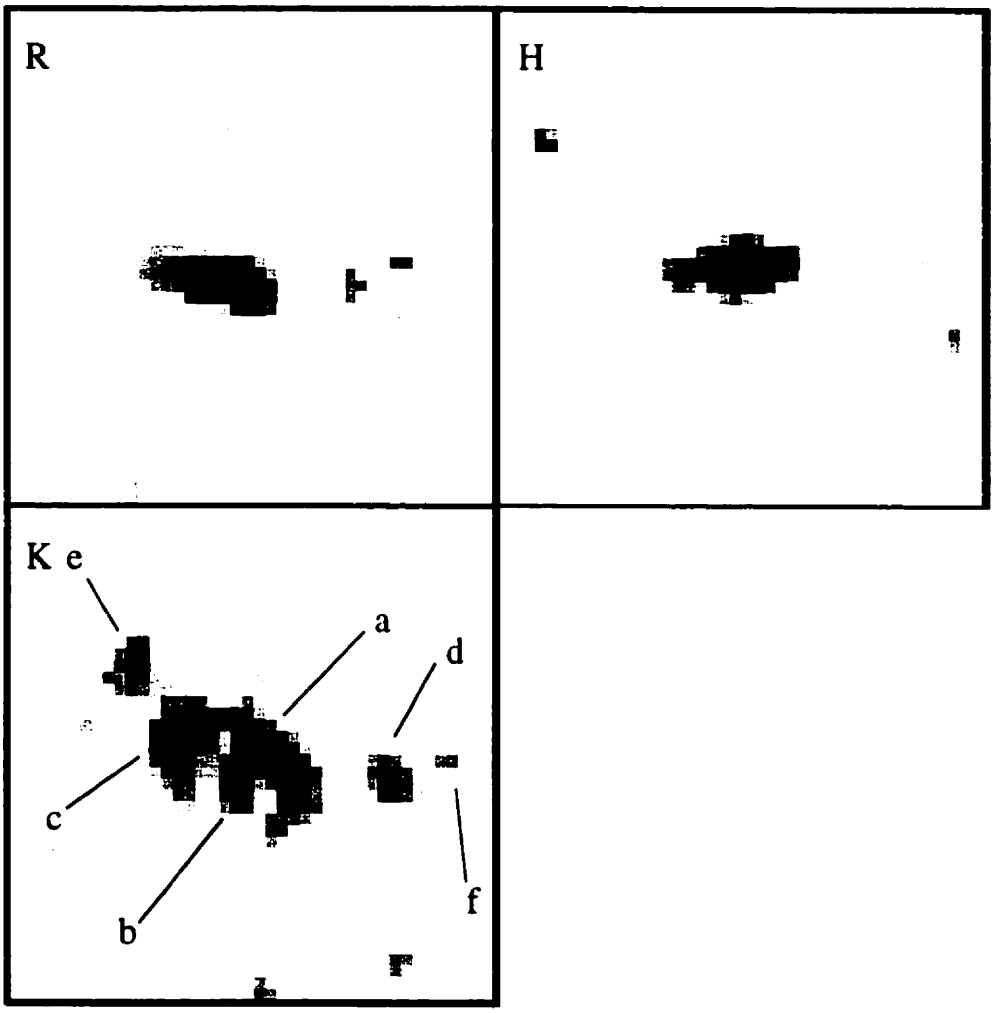

Figure 5.22: Images of the RG in the 4C +41.17 field. The FOV is 4″ × 4″ with north up and east left. See text for details.

Table 5.18: Photometry of 4C +41.17

Object	R	H	K	$R-H$	$H-K$	M_H
1 (RG)	22.1 ± 0.1	19.9 ± 0.4	18.0 ± 0.1	2.2 ± 0.5	1.9 ± 0.5	-26.9 ± 0.4
(a)	23.0 ± 0.1	20.2 ± 0.5	19.0 ± 0.2	2.8 ± 0.6	1.2 ± 0.7	-26.6 ± 0.5
(b)	23.0 ± 0.1	21.1 ± 1.2	20.2 ± 0.5	1.9 ± 1.3	0.9 ± 1.7	-25.7 ± 1.2
(c)	23.0 ± 0.1	21.0 ± 1.2	19.2 ± 0.2	2.0 ± 1.3	1.8 ± 1.4	-25.8 ± 1.2
(d)	23.8 ± 0.3	-	20.0 ± 0.5	-	-	-
(e)	25.3 ± 1.2	-	19.9 ± 0.5	-	-	-
(f)	-	-	21.0 ± 1.2	-	-	-
2 (A)	23.7 ± 0.3	20.4 ± 0.6	20.7 ± 1.0	3.3 ± 0.9	-0.3 ± 1.6	-26.4 ± 0.6
3 (B)	22.9 ± 0.1	-	20.0 ± 0.5	-	-	-

is not to be likely the source of this emission. Furthermore, the absorption line UV spectrum is similar to that of star-forming regions in nearby galaxies. This is evident in Figure 5.23 where the similarities are apparent between the absorption features of 4C +41.17 and a star-forming knot in the starburst galaxy NGC 1741. This, along with the low polarization, suggests that the UV emission is due to star formation.

Because at $z = 3.8$ the CO $J = 1 - 0$ transitional line is redshifted to 23 GHz this object has also been the target of intensive searches for molecular gas. All have been unsuccesful (e.g., Ivison et al. 1996, Barvainis and Antonucci 1996, and van Ojik et al. 1997) but have constrained the dust content to be below $4 \times 10^{11}\ M_{\odot}$.

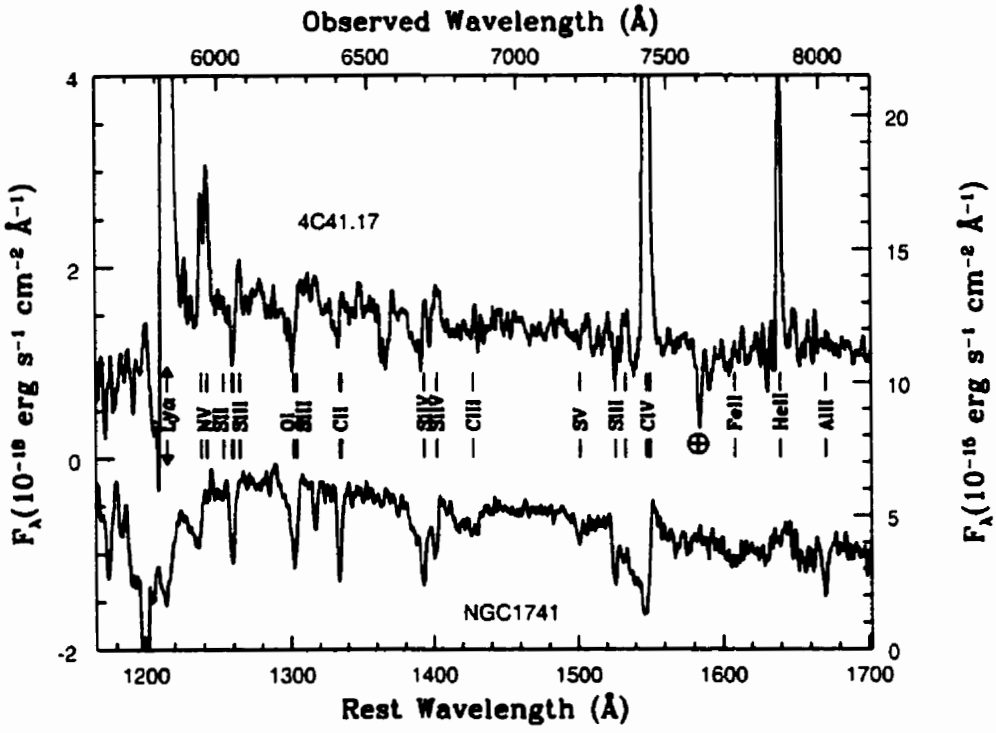

Figure 5.23: Deep Keck Telescope visible spectrum of 4C +41.17 taken from Dey et al. (1998).

Chapter 6

Environments of High-Redshift Radio Galaxies

6.1 Stellar Populations

The spectral synthesis models of Bruzual and Charlot (1993) were used to estimate the ages of potential stellar populations in the radio galaxy (RG) fields. These yield the Galaxy Isochrone Synthesis Spectral Evolution Library (GISSEL) isochrones. By experiment with the parameters of their code it was determined that very simple models of star formation and galaxy evolution were sufficient to match the observed colours of the objects in the fields within the errors.

The GISSEL approach is to start with an initial mass function (IMF), star-formation rate, and a set of stellar evolutionary tracks to predict the evolution of a population of stars. That is, an initial distribution of masses of stars in the model is assumed (based on observations of local stars in our Galaxy). At each time-step for a given mass of star the position along its stellar evolutionary track is determined. A library of stellar spectra is available

which represents increments along the stellar evolution tracks. The composite spectrum of the evolving population of stars is calculated by adding the spectra of the individual stars from that library and weighting these according to the IMF. By convolving the resulting spectral energy distribution (SED) with functions for reddening and observational passbands (much as discussed in Section 3.2) observed galaxy colours can be predicted.

In Figures 6.1 through 6.8 either $R - I$ versus $I - H$, $R - H$ versus $H - K$, or $J - H$ versus $H - K$ colours for all the objects in the fields are overplotted with isochrone predictions corresponding to three main models. The first model is a single burst of star formation lasting 1 Gyr followed by passive stellar evolution. The second is the same as the first, except that strong reddening, $A_V = 2.0$, is introduced. This is due to the evidence for obscuration in $R - K$ colours, specifically in 3C 230 and TXS 0828+193 (see Section 5.9). The third model is one of continuous star formation at a rate of 100 $M_\odot$ yr^{-1}. This high rate of star formation was purposefully chosen to 'saturate' the blue colours. That is, a higher rate of star formation cannot make the measured colours of the galaxy any bluer. These particular models were chosen because they bracket the extremes of expectations for evolution for these galaxies. In general the isochrones from the reddened passive evolution model are too red to match the observed colours. The predictions from the continuous star formation model are, likewise, too blue.

In each plot a solid line indicates the isochrone for a galaxy at $z = 1$. That is, it is a track giving the expected *observed* colour of a galaxy at $z = 1$ given the chosen model evolution (the bandpasses in the restframe of the model galaxy have been shifted accordingly). The epoch is indicated by

open circles at 1, 2, 5, and 20 Gyr after the onset of star formation. A dotted line indicates the isochrone for the same model galaxy if it were at $z = 2$, a short-dashed line for $z = 3$, and a long-dashed line for $z = 4$.

The GISSEL models suggest that the colours of all the RGs and their companions in the sample are blue and well fitted by a young or bursting stellar population. In the case of 3C 356 some reddening would be necessary to explain the $R - I$ versus $I - H$ colours of the RG. In all cases the errors in the colour measurements make it difficult to make any strong distinction between ages of the individual components of the RG and its companions. All of the colour information is consistent with stellar populations younger than 5 Gyr for all of the RGs.

6.2 Cluster Membership

Cluster membership was based on the available colour information on detected objects in the target fields and the GISSEL models. It was found that 2 to 5 objects fainter than the RG were found in the fields. In each case objects were rejected as cluster members only if they were brighter than the RG or had colours strongly inconsistent with the GISSEL predictions for a galaxy at the redshift of the RG. This is, of course, not sufficient proof of cluster membership for the remainder of objects. Spectroscopy would be needed to confirm the redshift of each object.

Figure 6.9 shows the results for the number of cluster members in a projected area of 0.01 Mpc^2. This has been corrected by assuming a uniform distribution of objects within the field and multiplying by the fraction of 0.01 Mpc^2 that each field samples (see Section 2.1). No correction has been made

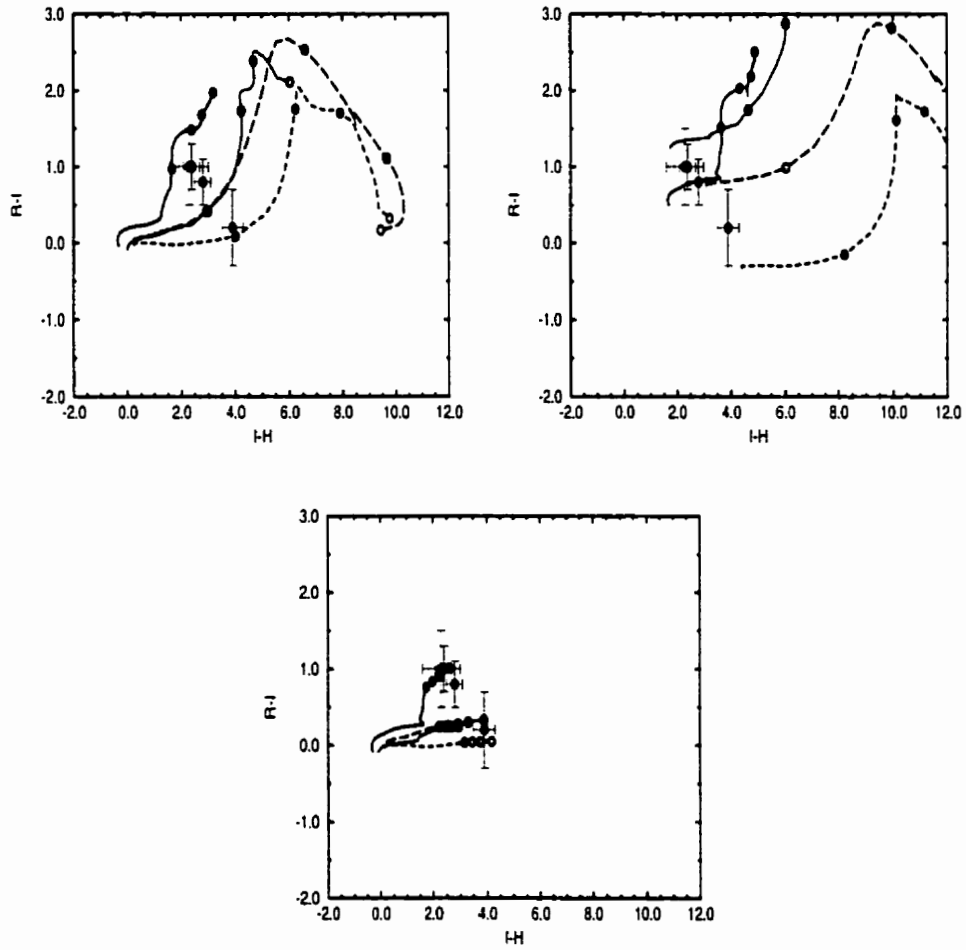

Figure 6.1: An $R - I$ versus $I - H$ colour-colour plot for objects in the 3C 356 field. The overplotted lines are the galaxy isochrones described in the text. At top-left is a model with a single burst of star formation of 1 Gyr duration. At top-right is the same with internal reddening of $A_V = 2.0$ for the galaxy. A model of continuous star formation is shown below.

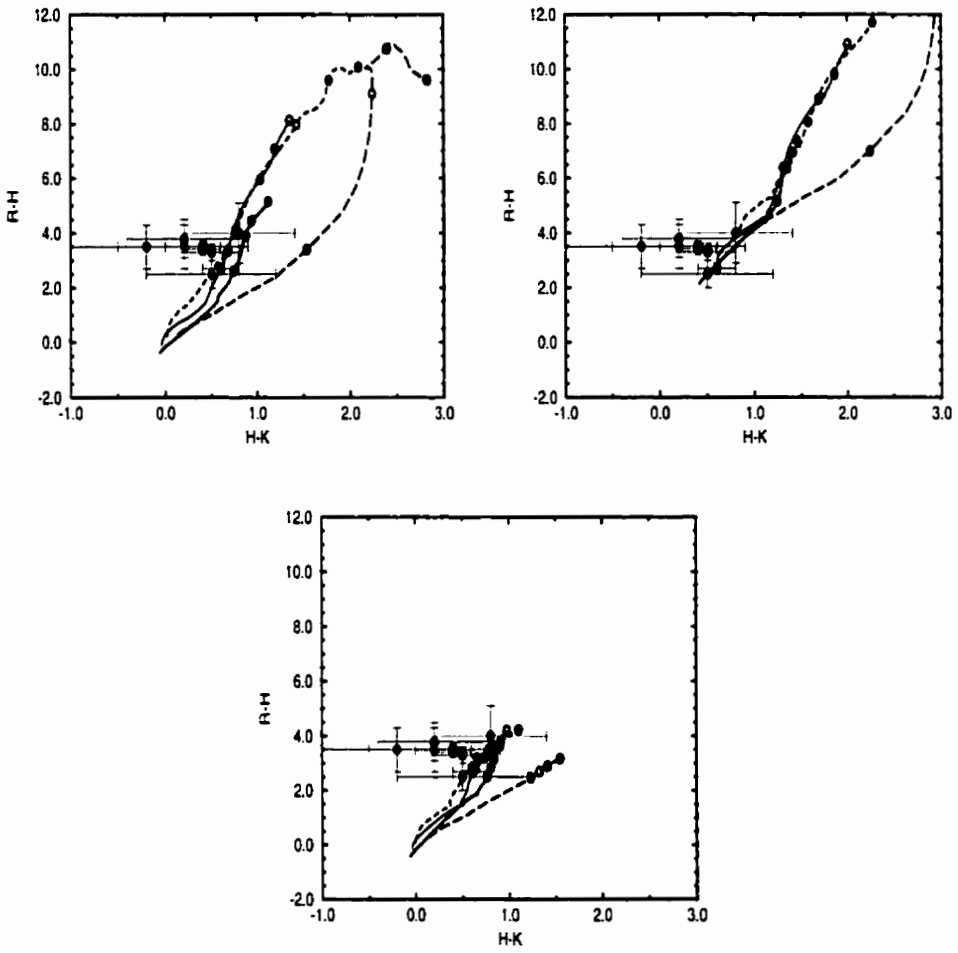

Figure 6.2: An $R-H$ versus $H-K$ colour-colour plot for objects in the 3C 230 field. The overplotted lines are the galaxy isochrones described in the text. The models are the same as in Figure 6.1.

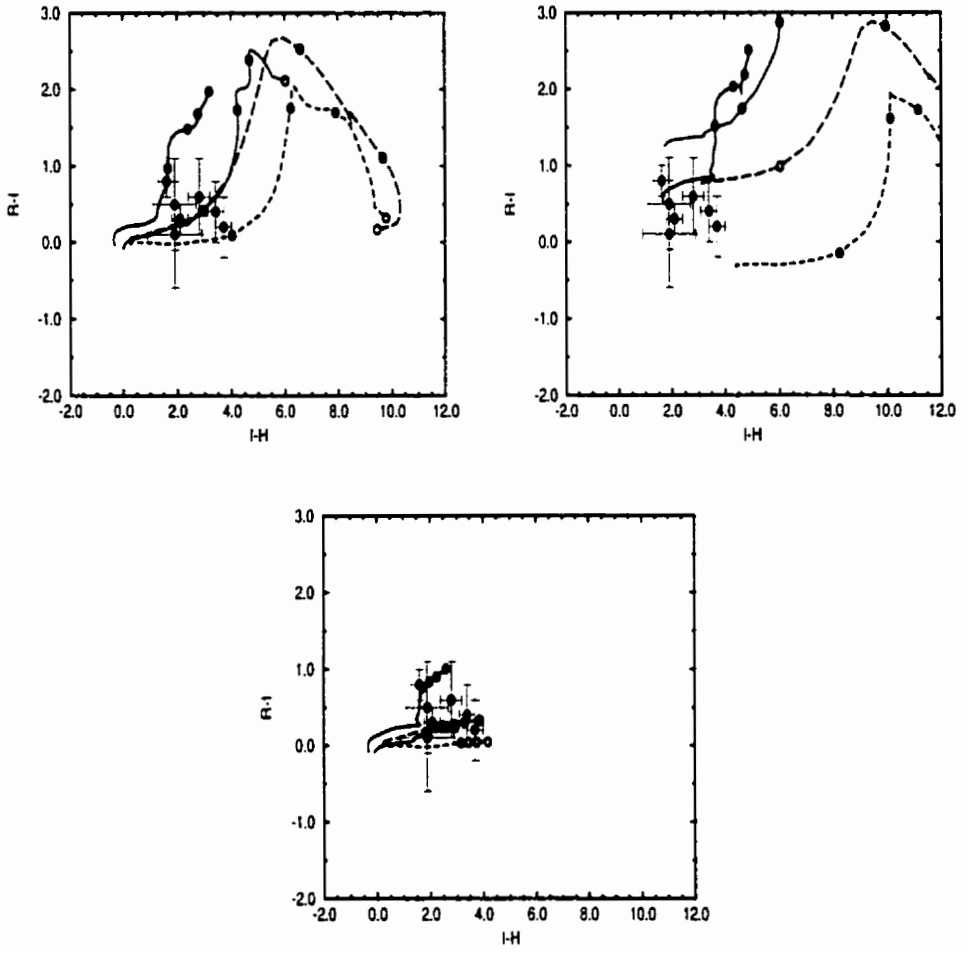

Figure 6.3: An $R - I$ versus $I - H$ colour-colour plot for objects in the 3C 68.2 field. The overplotted lines are the galaxy isochrones described in the text. The models are the same as in Figure 6.1.

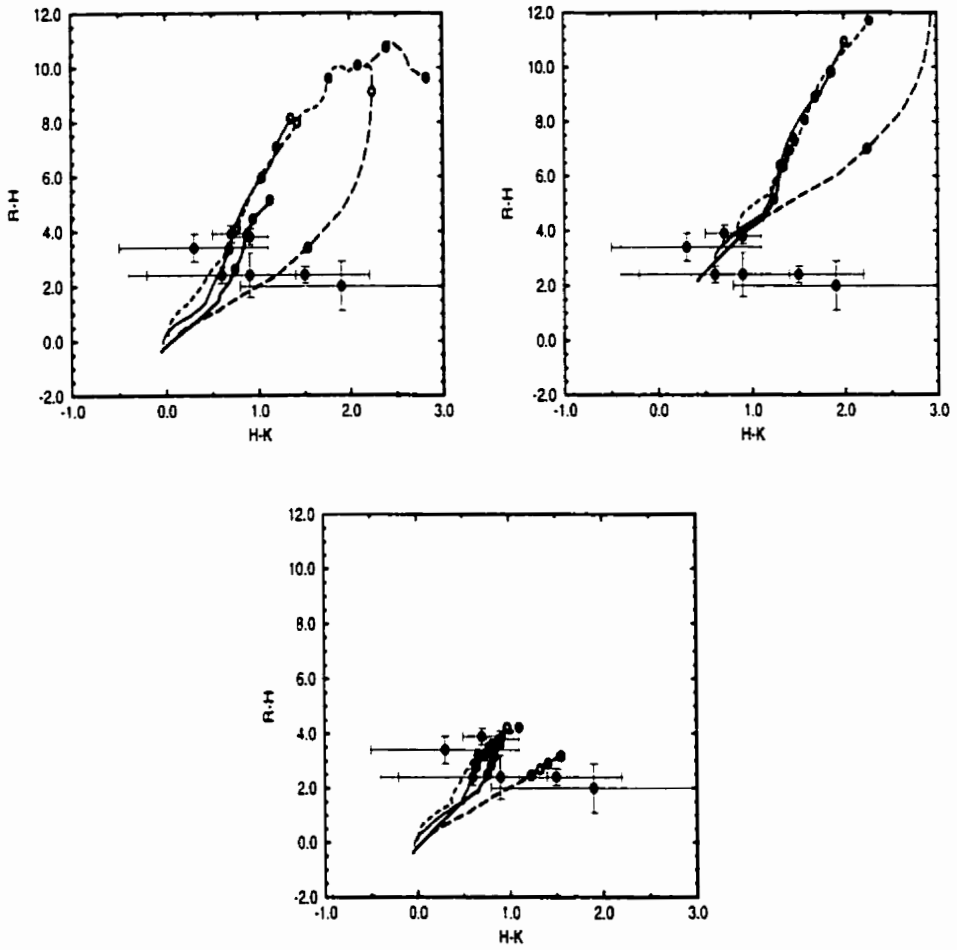

Figure 6.4: An $R-H$ versus $H-K$ colour-colour plot for objects in the 3C 68.2 field. The overplotted lines are the galaxy isochrones described in the text. The models are the same as in Figure 6.1.

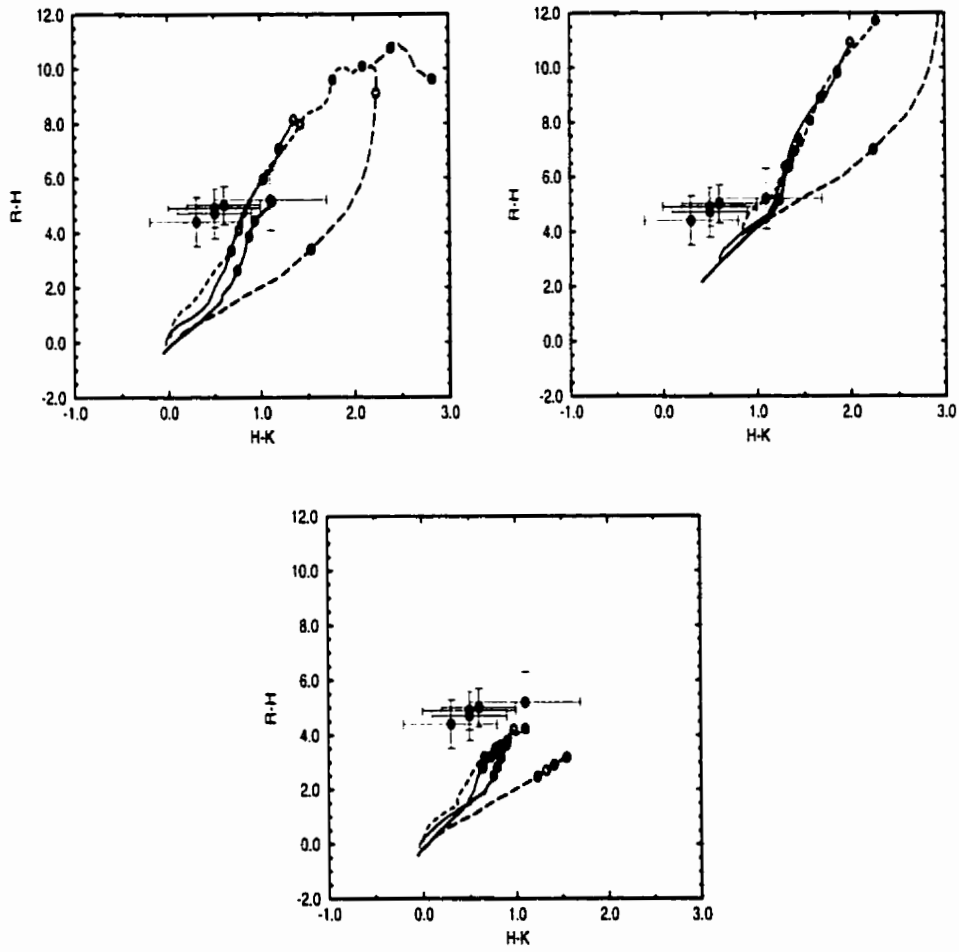

Figure 6.5: An $R-H$ versus $H-K$ colour-colour plot for objects in the 3C 294 field. The overplotted lines are the galaxy isochrones described in the text. The models are the same as in Figure 6.1.

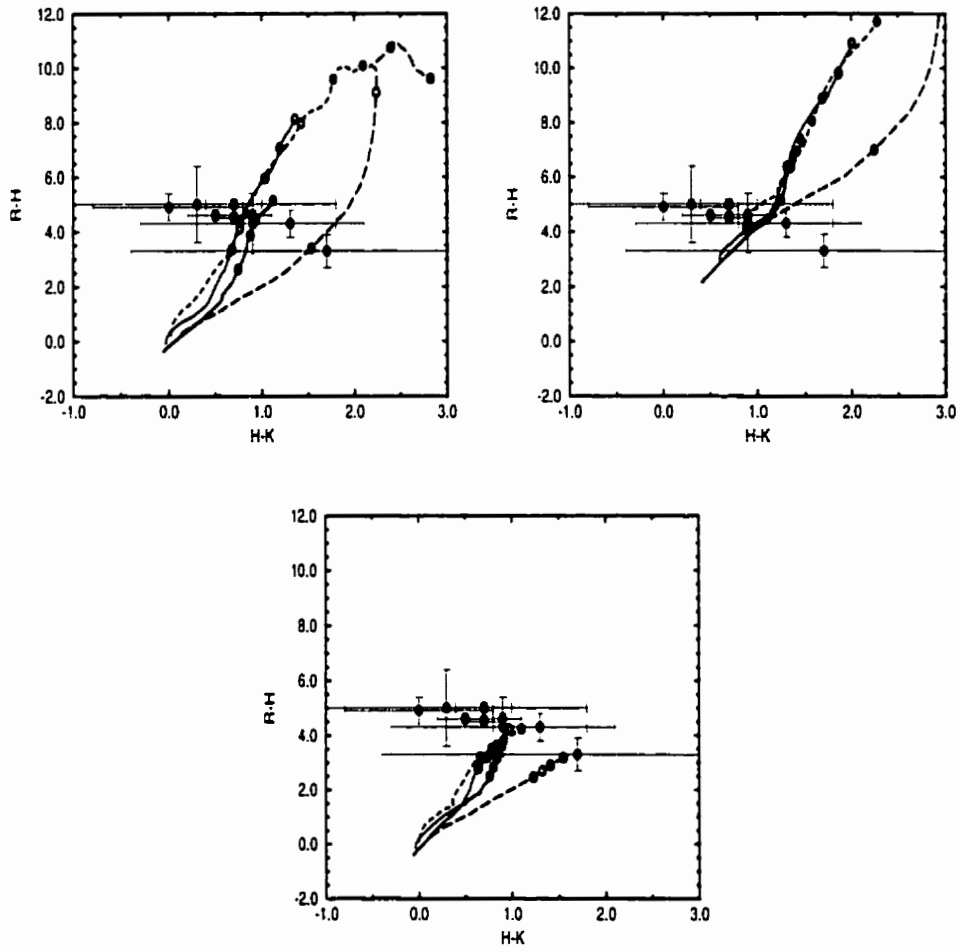

Figure 6.6: An $R-H$ versus $H-K$ colour-colour plot for objects in the TXS 0828+193 field. The overplotted lines are the galaxy isochrones described in the text. The models are the same as in Figure 6.1.

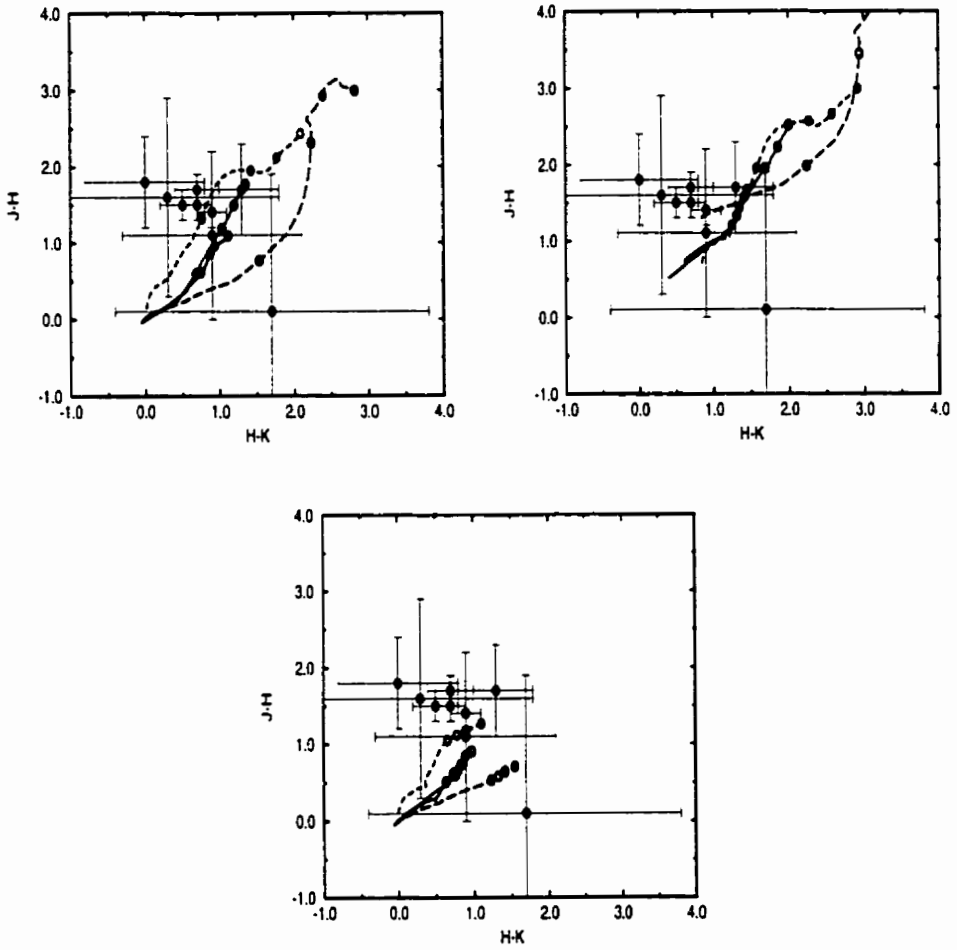

Figure 6.7: A $J-H$ versus $H-K$ colour-colour plot for objects in the TXS 0828+193 field. The overplotted lines are the galaxy isochrones described in the text. The models are the same as in Figure 6.1.

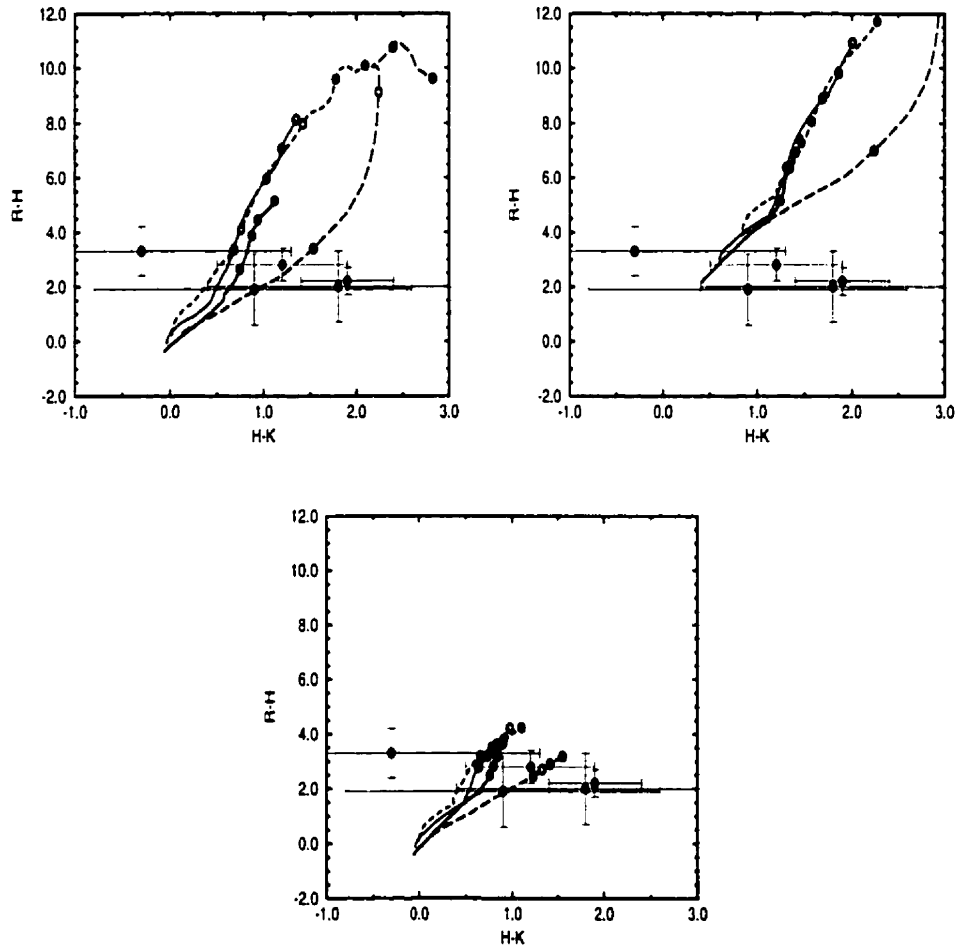

Figure 6.8: An $R - H$ versus $H - K$ colour-colour plot for objects in the 4C +41.17 field. The overplotted lines are the galaxy isochrones described in the text. The models are the same as in Figure 6.1.

for regions corrupted by bright stars but this is, typically, less than 5% of the total area so it was ignored. Also, the shape of the mosaiced fields are not uniform and sometimes are influenced by the radio morphology of the HzRGs (being elongated slightly along the axis of the radio lobes). For the most part the fields are square and since there does not seem to be a strong trend towards objects in the field (excluding the RG itself) being found along the axis of the radio lobes for this sample this effect is not considered to affect the results adversely.

The detection limit in all of the fields is about 22.5 magnitudes in H. From Figure 3.9 we can see that the number counts of galaxies in the Hubble Deep Field South (HDFS) in H is very steep. At $H = 21$ it is 1×10^4 deg^{-2} mag^{-1}. This is the number of galaxies per square degree fainter than $H = 20.5$ and brighter than $H = 21.5$ in a randomly selected field. For a field of approximately 30×30 arcsec^2 this corresponds to 0.7 galaxies. Even assuming 1×10^4 deg^{-2} mag^{-1} at $H = 19.5$ gives an expectation of finding only 1-2 galaxies with $19.5 > H > 21.5$ in a randomly chosen field of 30×30 arcsec^2. Thus, with an average of 3.3 ± 0.5 galaxies per 30×30 arcsec^2 we find an excess of 1 to 2 galaxies over the expected number of field galaxies for our sample.

6.3 Morphology

A simple analysis by eye of the images in Figures 5.11, 5.14, 5.16, 5.18, 5.20, and 5.22 reveals that the RGs are more complex at redshifts of $z > 2$ then at redshifts of $z < 2$. That is, there seems to be more knots of roughly equal brightness in the restframe visible bandpass (see Figure 5.9)

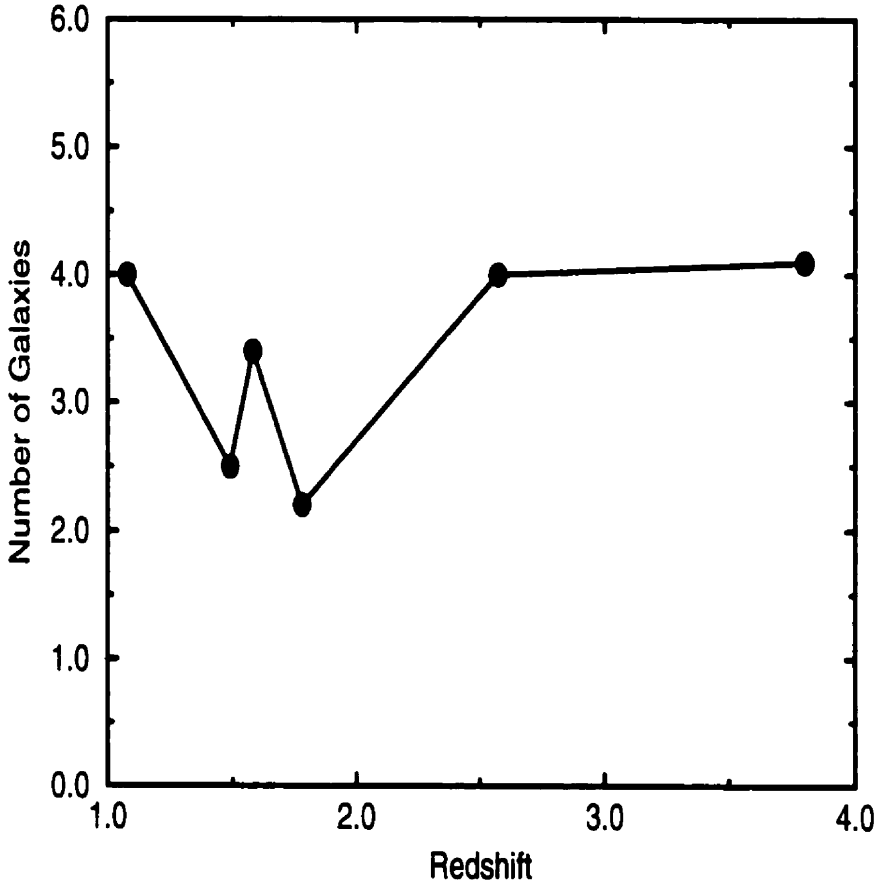

Figure 6.9: A plot of the number of galaxies in the cluster as a function of redshift.

Table 6.1: Galaxy Counts in the Fields

Name	z	Total	Fraction	Cluster (Corrected)
3C 356	1.08	4	0.12	-
3C 230	1.49	4	1.61	2.5
3C 68.2	1.58	3	0.89	3.4
3C 294	1.78	3	0.74	2.2
TXS 0828+193	2.57	3	1.34	4.0
4C +41.17	3.80	3	1.37	4.1

for HzRGs at $z > 2$. We will be careful only to make comparisons between different fields after accounting for the shifting bandpasses of our filters. The limiting magnitudes of the images from each of the three restframe bandpasses described in Section 6.1.2 are similar and since the imaging is most sensitive to bright compact objects the comparison of the number of knots in different fields is valid.

6.3.1 Counting Distinct Structures

In order to quantify the complexity of the RGs better a selection criterion was used to count the number of compact objects. The method was simply to count the number of peaks in the RG image. A peak was defined as a bright region of connected pixels that was separated from any other region by a trough of pixels with flux lower than half of the maximum brightness. This task was accomplished by analyzing the image of the RG with a display interface that permitted the flux in any pixel to be displayed when the cursor was pointed at it. By scanning the cursor over pixels radiating from a local maximum in the image it was straightforward to determine which peaks were

connected and which were isolated. Since all of the peaks were of roughly the same brightness the definition of the region of 50% brightness of the peak separating one peak from another worked consistently to locate isolated knots. Of course, this definition is not optimal but its intent is merely to quantify the morphology of the RG. No claim is made that this definition has a physical basis. There is no special significance to the '50% rule' other than that the S/N of the faintest detectable peaks is roughly 3 to 5 assuming it is a point-source. At half of the peak the flux in any pixel has, essentially, a S/N of unity.

Quantifying galaxy morphology cannot be described as an exact science so it is probably sufficient to state the definition of a knot used here. The net result is the number of bright compact components making up the RG. From Section 6.2 we suspect this light is from bright star-formation regions or their evolved products. Thus we are effectively counting the number of star-formation regions in the galaxies, and saying that this definition determines the morphology of the stellar component of RGs.

The results of this analysis are given in Table 6.2 and Figure 6.10. It is not surprising that this confirms the result of inspecting the RGs by eye. All of the galaxies would be classified as irregulars in both restframe UV and visible light in the standard Hubble sequence. The irregular 'chain galaxies' of the Hubble Deep Field (see Section 3.2.1) have similar clumpy morphologies in R and I imaging. A notable case is HDFS 318 ($z = 2.2$, Gwyn (2000)) which is composed of several bright knots within a diffuse nebulosity of $\sim 2''$ diameter. Another sample of galaxies at a similar redshifts (approximately $3 < z < 3.5$) with which to compare morphologies are the Lyman continuum

Table 6.2: Knot Counts in the Radio Galaxies

Name	z	Ultraviolet	Visible	Near-Infrared
3C 356	1.08	2	2	2
3C 230	1.49	2	3	1
3C 68.2	1.58	3	2	3
3C 294	1.78	1	4	3
TXS 0828+193	2.57	5	5	-
4C +41.17	3.80	3	6	-

break selected galaxies of Steidel et al. (1996). Imaging with the Hubble Space Telescope (HST) Wide-Field Planetary Camera 2 (WFPC2) in R, Giavalisco et al. (1996) show that most of these have a small but resolved core of about 0.7″ in radius and show a high degree of symmetry. That is, they are not irregulars.

6.3.2 Model Galaxy Profiles

The previous analysis suggests that the RGs are inconsistent with a population of relaxed evolved elliptical galaxies at these redshifts. It is interesting to consider if the removal of the knots from the images might reveal an underlying galaxy which *is* consistent with this picture as suggested by Pritchet (2000). To investigate this possibility I developed a method to model the profiles of the galaxies and subtract the knots.

For each RG an image of approximately the size shown in the enlarged views was extracted for each filter and rotated to a common alignment along the axis of the greatest elongation. For each image the pixel values were summed along a direction perpendicular to this axis. In effect, the images

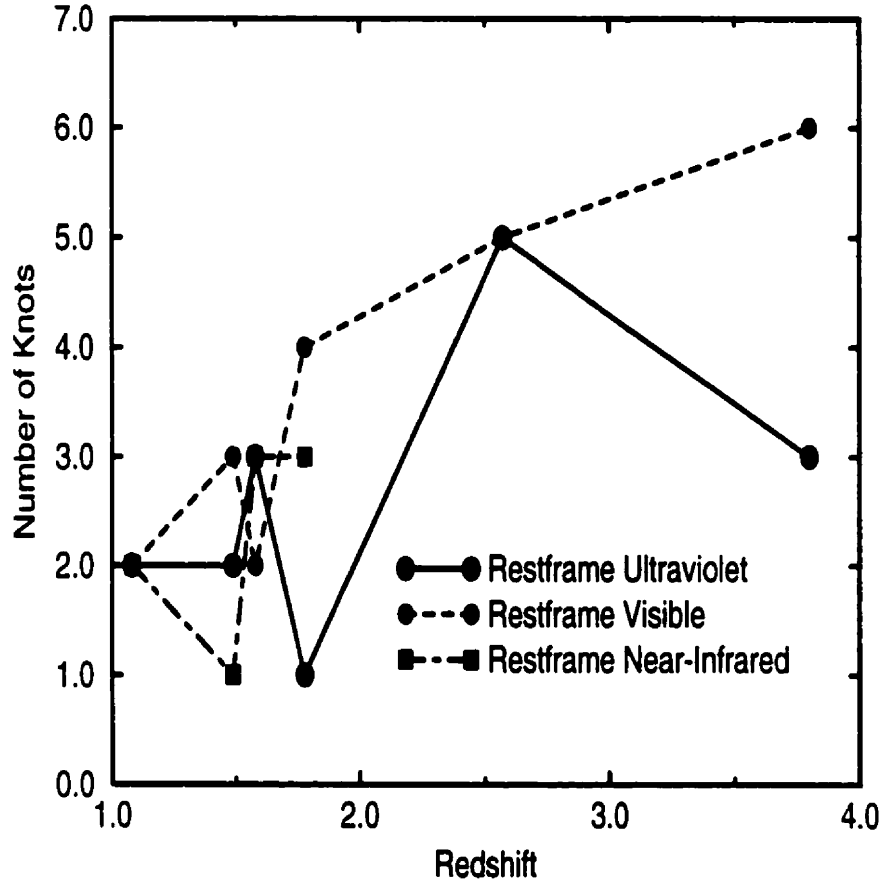

Figure 6.10: A plot of the number of objects in the RG as a function of redshift.

were compressed to slices along the axis of the RG. These profiles were normalized to have peak fluxes of unity.

The results in Section 6.1 would suggest that the galaxies are composed entirely of bright unresolved regions of young stars. Thus a model of each RG for each filter was generated as a composition of Gaussian profiles. The Gaussian had a FWHM given by the image resolution in Table 5.10. The model galaxy was built up by starting with a blank image the same size as the RG image and adding a Gaussian with peak flux and position determined from the photometry in Section 5.6. This image was then summed in the same manner as for the real data and normalized to a peak flux of unity.

For each RG and each filter the model galaxy was subtracted from the data. The results can be seen in Figures 6.11 trough 6.16. The data are shown at top, the model at lower-left, and the residuals at lower-right. These show that the model galaxies account for almost all of the light in the data. In some cases the residuals show a sharp peak (for example at -0.25″ in *H* for 3C 68.2). This peak is always of the same FWHM as the imaging resolution for that bandpass. This can only suggest that an unresolved knot was missed by the method of Section 6.3.1. Accounting for these missed knots leaves residuals in each band for all the RGs that are random and have $\sigma < \pm 0.3$ in normalized flux to the peak of the original image. This is consistent with the noise in the images.

The net result, then, is that a model of unresolved knots can account for all of the flux in the RG images. To the detection limit of the imaging none of the galaxies can be fitted with a de Vaucouleurs' $r^{1/4}$ profile (See Section 2.2).

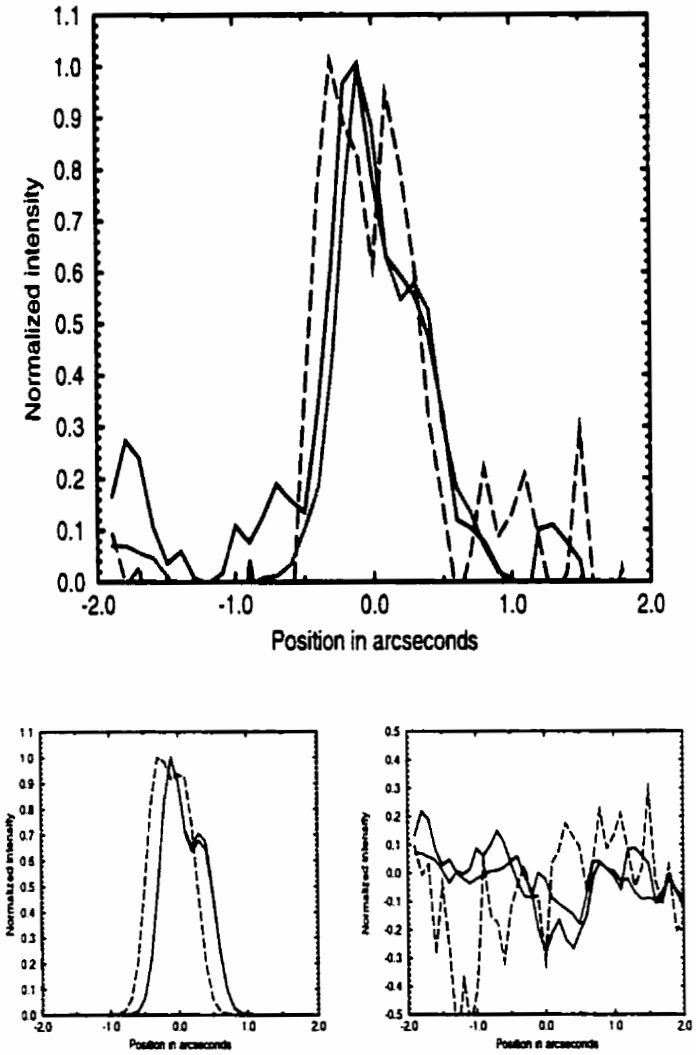

Figure 6.11: Plot of the profile of the RG for 3C 356 (top). The lines have the same sense as in Figure 5.9. That is, a solid line for R, a dotted line for I, a short-dashed line J, and long-dashed line for H, and a dot-dashed line for K. The model is shown as lower-left and the residuals at lower-right.

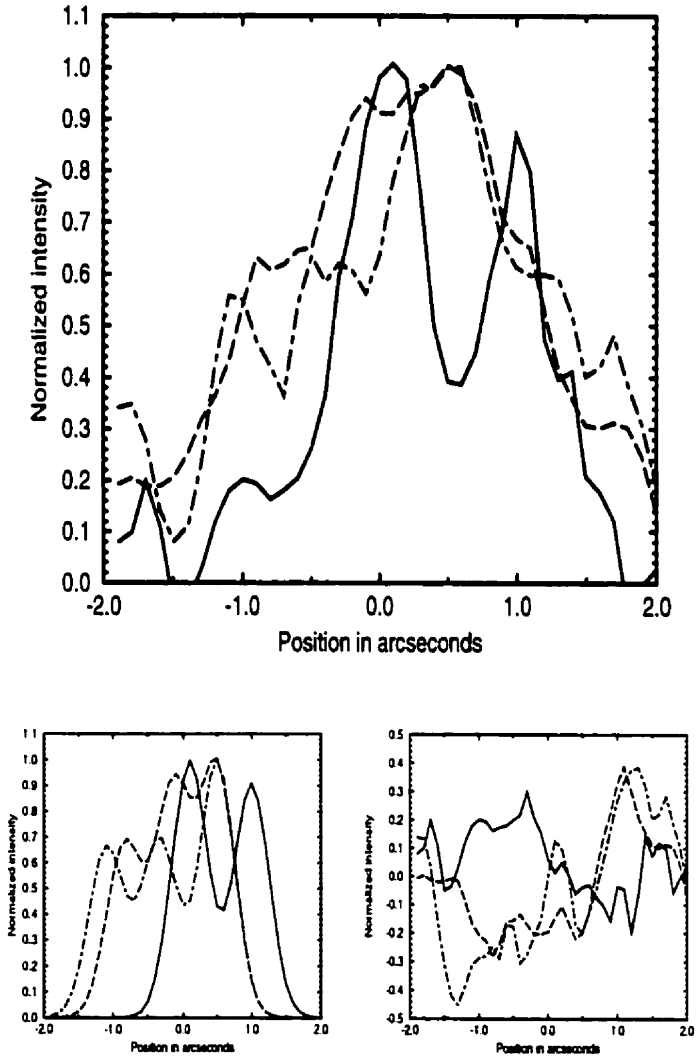

Figure 6.12: Plot of the profile of the RG for 3C 230. See the caption of Figure 6.11 for details.

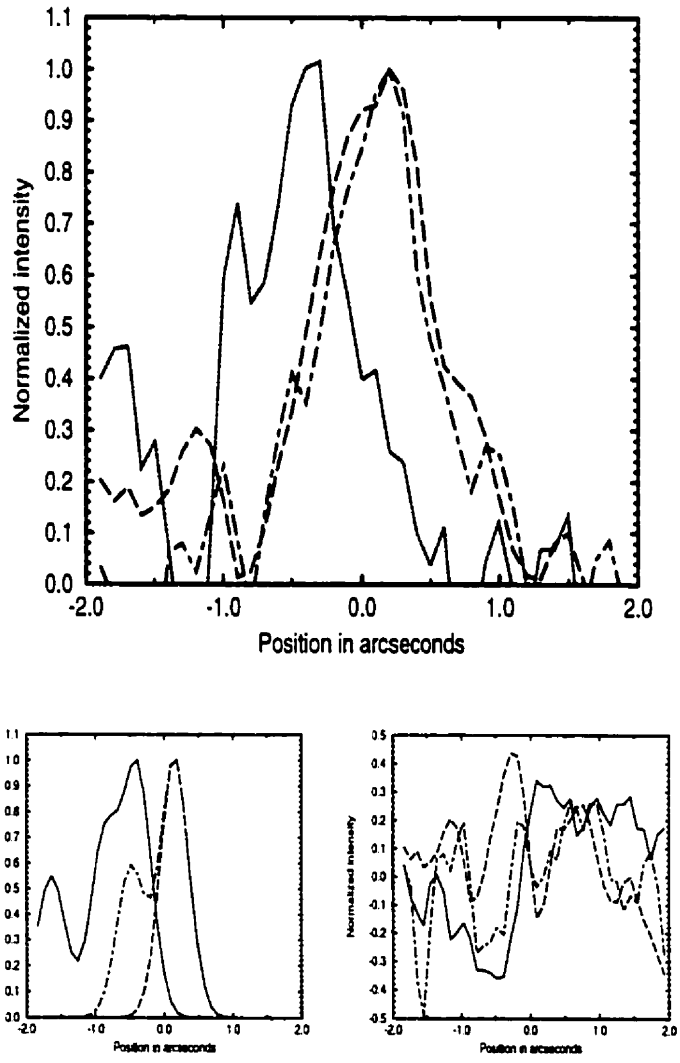

Figure 6.13: Plot of the profile of the RG for 3C 68.2. See the caption of Figure 6.11 for details.

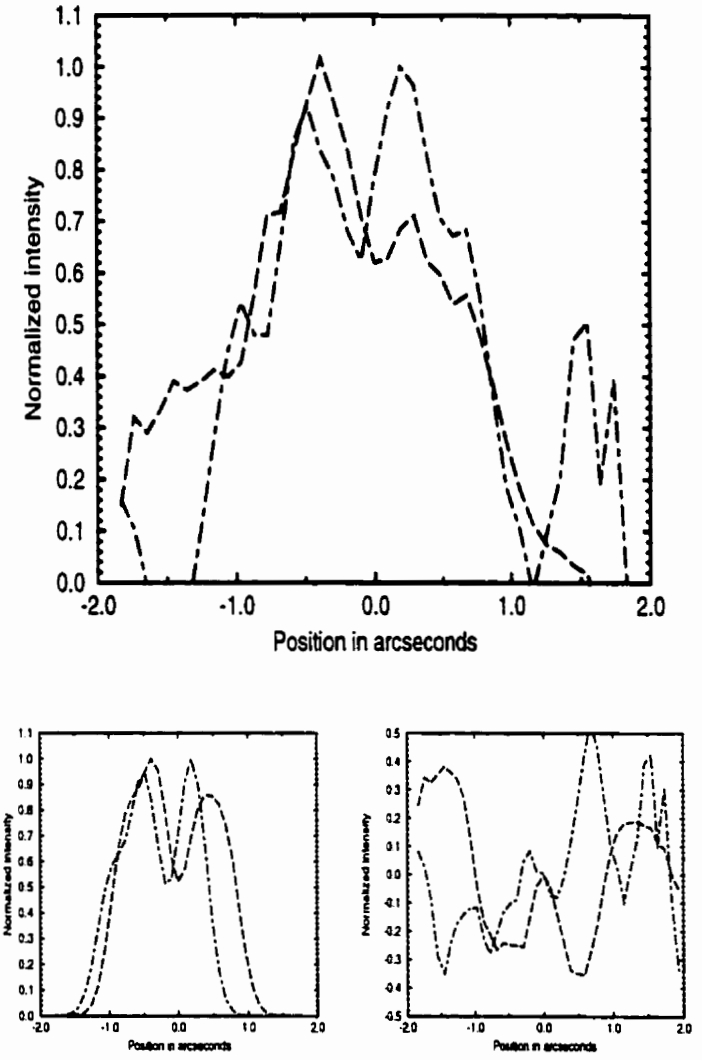

Figure 6.14: Plot of the profile of the RG for 3C 294. See the caption of Figure 6.11 for details.

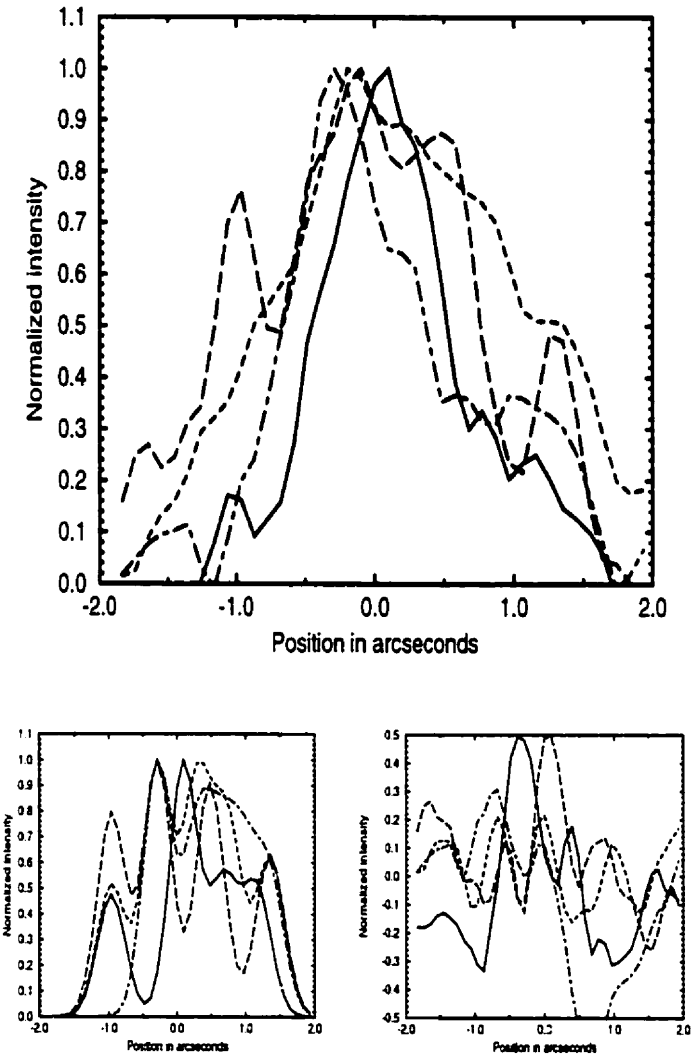

Figure 6.15: Plot of the profile of the RG for TXS 0828+193. See the caption of Figure 6.11 for details.

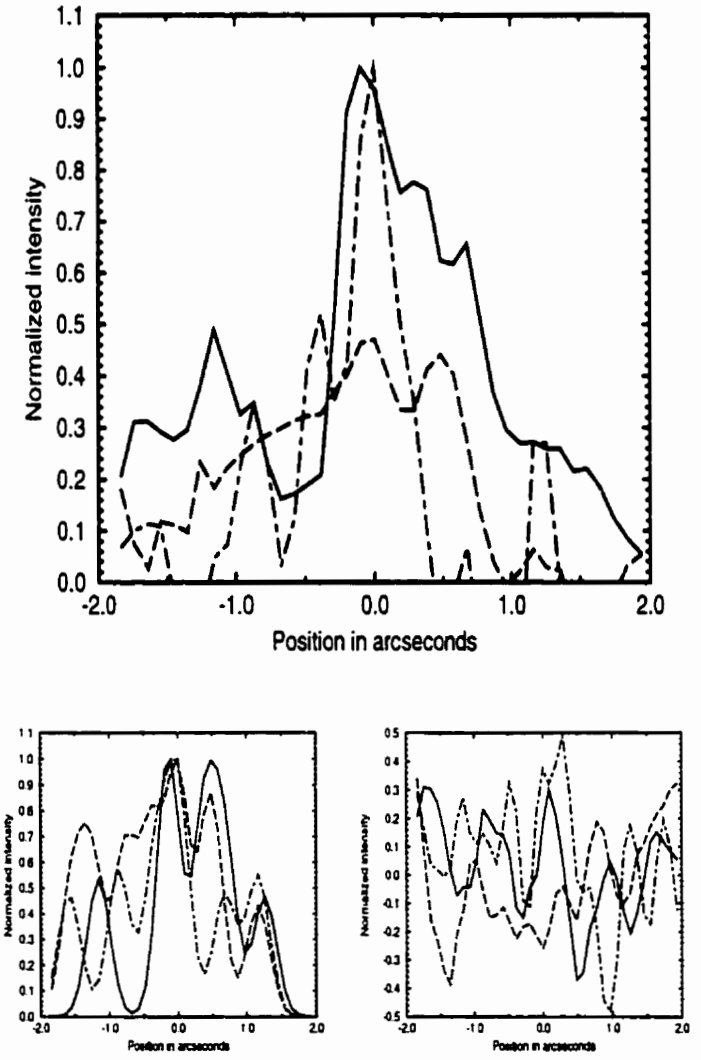

Figure 6.16: Plot of the profile of the RG for 4C +41.17. See the caption of Figure 6.11 for details.

Table 6.3: Physical Size of the Radio Galaxies

Name	z	M_H	Area (kpc^2)
3C 356	1.08	-26.3	25.2
3C 230	1.49	-26.7	61.6
3C 68.2	1.58	-26.5	56.0
3C 294	1.78	-26.2	74.1
TXS 0828+193	2.57	-27.9	71.8
4C +41.17	3.80	-26.9	86.2

6.4 Physical Size and Brightness

Other than the complexity of the morphology of the RGs another aspect that appears to change with redshift is their physical size. In order to estimate this size a rectangular box was constructed which enclosed all of the connected pixels selected by the 50% rule. I assumed $H_0 = 70$ km s^{-1} Mpc^{-1} and $q_0 = 0.5$ and estimated the projected physical size of the RGs for the sample. The results are given in Table 6.3. There seems to be a trend to smaller physical size towards lower redshift. The absolute brightness of the RGs, however, is roughly constant with redshift and consistent with values for cD galaxies at low redshift (McCarthy 1993). It is possible that the decrease is an apparent change in size and that the galaxy is still physically large. This might be the result of stellar evolution. Stars redden and dim and, perhaps, only the brightest star formation regions are still visible by redshifts of $z = 1$.

6.5 Results

In all cases for this very small sample of RGs the AGN host galaxy is seen to be residing in a poor cluster environment. There is typically an excess of 2 or 3 objects over expectations for randomly selected fields of the same FOV and depth. The RGs themselves are found to have perhaps only 2 or 3 distinct components in the restframe visible and UV at $1 < z < 2$, but, for $2 < z < 4$ the HzRG seems to be composed of twice to three times as many components.

The colours of these knots (as well as companions) are consistent with young stellar populations and the decrease in the number of knots but not the brightness of the RGs can be simply explained as the assembly or merging of these components with time. None of the RGs looks like a typical low redshift RG.

These main results were presented at the American Astronomical Society Conference in Austin, Texas (Steinbring et al. 1998).

Comparison of these results with the AO study of QSO host environments (8 QSOs with $0.85 < z < 4.16$, Hutchings et al. 1999) reveals no evidence to suggest a difference between it and HzRG environments. That is, a similar number of companion objects is detected in images of similar depth and FOV centred on the AGN host. The number of detected companions from that study has more scatter than for the HzRGs (ranging from 2 to 9 objects) but also shows no trend with redshift. The mean number of objects (QSO host and companions) with 1-σ errors is 4.4 ± 2.5 while for the HzRG sample it is 3.3 ± 0.5.

Since the host galaxies of the QSO sample have not been resolved to

a similar degree to those of the HzRG sample (most are unresolved) it is unknown if the host galaxies themselves are similar.

Chapter 7

Conclusions and Future Work

7.1 Ground-Based Adaptive Optics Off-Axis Imaging

Observations of faint targets with adaptive optics (AO) and a natural guide-star require that star to be bright. Typically, observations are made with the telescope pointed at an offset from the guide-star. These off-axis observations have the disadvantage of providing poorer delivered correction to the point spread function (PSF) at the target position. But how much poorer? Figure 3.19 suggests that for the Canada-France-Hawaii Telescope (CFHT) Adaptive Optics Bonnette (AOB) an offset of 20″ might mean a delivered PSF with a full width at half maximim (FWHM) twice as wide as the guide-star PSF.

As discussed in Section 2.3.1 this drop in performance with offset is simply because the wavefront sensor can only sense wavefront distortions within the pupil of the telescope. The active optical components are only correcting the wavefront over the pupil as well. The wavefront outside the pupil - or equivalently at an off-axis telescope position - has a different shape than inside. This means the corrected wavefront and PSF for the off-axis

position is poorer than for on-axis.

One way of solving this problem is to permit the deformable mirror (DM) to correct an area larger than the pupil. This possibility is studied in the context of the Gemini North Telescope (Gemini) Altitude-Conjugate Adaptive Optics for the Infrared (Altair) system. A single wavefront sensor will still be able only to sense the wavefront within the telescope pupil but there are ways to extrapolate this information to outside the pupil and produce a better corrected PSF at off-axis positions. Simulations using the software Altair-Offaxis demonstrate that the extrapolation technique of slaving voltages sent to the deformable mirror components outside the pupil to those within the pupil can provide an increase in performance at off-axis positions. A later study by Véran (1998) has shown that this slaving technique can be optimized to provide significant improvement in the off-axis PSF for Altair.

Recently, it has been proposed that one could use several DMs and a constellation of laser guide-stars to correct a larger field of view (FOV) for an 8 m telescope like Gemini as well as a future generation of even larger telescopes (Ellerbroek and Rigaut 2000). A realistic simulation of such a multi-conjugate AO (MCAO) system is more complicated than a simple multiplication of the workings of Altair-Offaxis but there are many similarities in the optimization of the correction. I am interested in the challenge of determining an optimal slaving function for such a system. In the meantime I will study - by developing simulations similar to my NGST VI/MOS software - the scientific benefits of the Gemini MCAO for observations of faint galaxies.

7.2 Space-Based Imaging and Spectroscopy

A distinct advantage of imaging and spectroscopy performed with space-based telescopes over those on the ground, especially in the near-infrared (NIR), is the fainter and less variable background light. This is because the main component is the zodiacal background which is not variable over the course of a typical observation, as is the case for the background for ground-based observations. Another advantage over present AO observations is a larger field of view with a diffraction-limited PSF. The AO isoplanatic patch is, typically, only 30″ across.

A serious disadvantage for a non-Earth-orbit space-based observatory like the Next Generation Space Telescope (NGST), however, is that the instrumentation at launch is the only complement it will have. There can be no instrument repairs or adjustment. This requires very careful selection of parameters such as pixel scale for cameras and necessitates an extremely high degree of reliability in instrumentation, especially those with moving parts.

This was the impetus for the design of the NGST VI/MOS software. This 'holistic' approach to studying the design of the Visible Imager (VI), NIR imager, image slicers, and multi-object spectrograph (MOS) was necessary because the NGST will be capable of imaging and spectroscopy of objects fainter than anything yet observed. A simulation based on extrapolations of the deepest Hubble Space Telescope (HST) data is the most reliable means of predicting the results. A 'virtual telescope' and 'virtual instruments' allow for the rapid search of the specification parameter space and the determination of results for the actual observing campaigns that drive the telescope design in the first place.

The preliminary results of these virtual observing runs for deep imaging of galaxy fields show that a dedicated VI, with its better efficiency and pixel sampling will obtain higher S/N results than a NIR imager working at wavelengths shorter than 1 micron. This is also true for observations of globular cluster fields in nearby galaxies. A VI would detect the white dwarf sequence in these globular clusters with a reasonable amount of observing time while a NIR camera would not. The results for simulations of several MOS designs on galaxy fields suggest an optical-fibre positioning device is competitive with micro-mirror devices. An advantage of fibre-positioning devices would be their higher efficiency of detector coverage for high-spatial-resolution spectroscopy. Furthermore, a image-slicing IFU would be a powerful tool for studies of complicated high-z galaxies. The high spectral resolution it affords - due in part to efficient detector coverage with reformatting - is coupled with the high spatial resolution advantage of NGST.

An IFU will possibly give some of the most dramatic results for NGST. An especially interesting field of study would be high-redshift radio galaxies (HzRGs). Is there a difference in ages of stellar populations along the axis of the radio lobes? Is the star-formation induced by the radio jets? To answer these questions we need deep spatially resolved NIR spectra of all of the knots within the HzRG cores. This would elucidate the star-formation histories of all of the sub-components.

7.3 Observing Methods and Analysis of Adaptive Optics Imaging

Off-axis AO imaging of faint objects presents some unique challenges. Imaging with fainter guides than is desirable while the telescope is pointed 20 to 30 arcseconds off-axis means that the delivered correction is not optimal. Low flux from the target object, high and variable sky flux and the presence of bright stars in the observations make the imaging difficult. Also, since the PSF at the target position must be known, some calibration observations need to be made. These problems can be overcome. Several observing and image processing techniques have been discussed that overcome the particular difficulties associated with deep AO imaging.

For natural guide-star AO the observer must select targets carefully and generate a list of possible targets that permit sufficient AO correction to warrant observation while still maintaining a large enough sample to accomplish the scienctific goals. This is not a trivial task as demonstrated by the rather small list ($\sim$ 25) of HzRGs that were possible targets for CFHT AOB. Furthermore, during the observing run the observer must be alert to the changing natural seeing conditions in order best to select those targets that will permit the maintenance of good AO imaging.

The observer must obtain calibration data. These are data for the guide-star PSF throughout the run as well as separate images of dense star-fields. With the observing done and data in hand the observer will need to apply some AO processing and analysis methods to make the imaging a success. Flat-fielding of the images is difficult but best done with the target exposures themselves. The PSF must be determined at the target position. If there

exists observations of the guide-star on the target observations then this can be accomplished by correcting it using the calibration observations of the star-field. Even if the image of the guide-star is overexposed, a method of fitting the wings may be able to reconstruct the true PSF.

The software AOTOOLS is an image processing pipeline that deals with these concerns. Imaging with AO is a relatively new field and it is hoped that this preliminary attempt at an AO-image-processing package will provide assistance in the next generation of better, more user-friendly, software. Over the next few years I will be working on building such a software environment for the Keck Telescope AO system. My hope is both to automate the reductions and improve their quality. To improve the PSF calibration software for the Keck and other AO systems, more data are needed which correlate the observed AO PSF with atmopheric conditions for a wide range of seeing, air-masses, and guide-star brightnesses. This could be accomplished with programs of simultaneous dense star-field observations, temperature and wind measurements, and scintillation detection and ranging (SCIDAR) observations. The last yields a $C_n(h)$ profile to compare with the isoplanatic variation in the PSF (see Section 2.3.1). I am involved in such a campaign (excluding SCIDAR) for natural guide-stars with the AO system on the Lick Observatory 3 m telescope. We will expand this program to include laser guide-stars in 2001.

The great advantage of AO imaging, of course, is that it is comparable to space-based observations. By applying a few simple techniques to calibrate the two, essentially registering observations of dense star-fields observed with both the space and ground-based systems, the two can be be made to com-

plement each other well. Larger ground-based telescopes with better AO systems, observing stategies, and image processing techniques will probably always make ground and space-based imaging equally attractive possibilities.

7.4 Merging in High-Redshift Radio Galaxies

The main result of this study is that RGs become more knotty and complicated in restframe-visible light towards higher redshift. They, and QSO host galaxies, reside in similar cluster environments over the redshift range studied. The change in the morphology of the young stellar populations of HzRGs suggests that RGs are also being assembled at these redshifts. Deep imaging of a larger sample of RGs at $z > 1$ would improve this result. The present small sample makes it uncertain how the result is affected by radio brightness, for example.

Certainly this study demonstrates the benefit of obtaining high-resolution NIR imaging of these systems. This is the first study to show that at least some HzRGs are not passively evolved ellipticals at $z > 2$. The next generation of AO systems, notably for Gemini and Keck, will certainly help our understanding of the changing environments of HzRGs. We have detected only the brightest knots within these RGs. Perhaps the diffuse halo so notable in the likely low-redshift products of HzRGs is simply too faint to be detected in our CFHT and HST images.

Bibliography

Aretxaga, I., Le Mignant, D., Melnick, J., Terlevich, R. J., and Boyle, B. J.: 1998, *Mon. Not. R. Astron. Soc.* **298**, L13

Bahcall, J. N., Kirhakos, S., Saxe, D. H., and Schneider, D. P.: 1997, *Astrophys. J.* **479**, 642

Barvainis, R. and Antonucci, R.: 1996, *Publ. Astron. Soc. Pac.* **108**, 187

Beckers, J. M.: 1993, *Ann. Rev. Astron. & Astrophys.* **31**, 13

Bennet, A. S.: 1962, *Mon. Not. R. Astron. Soc.* **68**, 163

Bertin, E. and Arnouts, S.: 1996, *Astron. Astrophys.* **117**, 393

Best, P. N., Longair, M. S., and Röttgering, H. J. A.: 1996, *Mon. Not. R. Astron. Soc.* **280**, L9

Best, P. N., Longair, M. S., and Röttgering, J. H. A.: 1997, *Mon. Not. R. Astron. Soc.* **292**, 758

Best, P. N., Röttgering, H. J. A., and Longair, M. S.: 2000, *Mon. Not. R. Astron. Soc.* **311**, 1

Biretta, J.: 1996, *'WFPC2 Instrument Handbook'*, STScI

Bouwens, R., Broadhurst, T., and Silk, J.: 1998, *Astrophys. J.* **506**, 557

Bruzual A., G. and Charlot, S.: 1993, *Astrophys. J.* **405**, 538

Burgarella, D., Bouwens, R., and Broadhurst, T.: 1998, in *The Next-Generation Space Telescope: Science Drivers and Technological Challenges, Procedings of the 34th Liege Astrophysics Colloquium, June 1998*, p. 225

Carlberg, R. G., Yee, H. K. C., Morris, S. L., Lin, H., Sawicki, M., Wirth, G., Patton, D., Shepherd, C. W., Ellingson, E., Schade, D., Pritchet, C. J., and Hartwick, F. D. A.: 1998, in *Wide Field Surveys in Cosmology, Procedings of the 14th IAP meeting held May 26-30 1998 in Paris, France, Editions Frontieres*, p. 143

Chambers, K. C. and Charlot, S.: 1990, *Astrophys. J.* **348**, L1

Chambers, K. C., Miley, G. K., van Breugel, W. J. M., Bremer, M. A. R.,

Huang, J., and Trentham, N. A.: 1996, *Astrophys. J., Suppl. Ser.* **106**, 247

Cimatti, A., Dey, A., van Breugel, W., Hurt, T., and Antonucci, R.: 1997, *Astrophys. J.* **476**, 677

Cochran, G. M.: 1985, *Optical Sciences Report No. TR-663*

Cortial, F., Ossart, F., Albertini, J. B., and Aid, M.: 1997, *IEEE Trans. on Magnetics* **33**, 1592

Crampton, D., Roberts, S., Herriot, G., Lilly, S., Bakshi, S., Parameswaran, A., Syrzycki, M., Steinbring, E., Nahon, M., Sharf, I., Buckham, B., Erickson, D., Carretoro, J., Abbot, C., Gaunt, R., Kabush, G., McIlwain, A., Vrooman, R., Booey, D., Hill, A., Taylor, K., Townsend, B., Richardson, E. H., Bell, A., Buttner, G., Evans, C., Maule, D., and Rowlands, N.: 1999, *NRC/NASA Internal Report*

Crawford, C. S. and Fabian, A. C.: 1993, *Mon. Not. R. Astron. Soc.* **260**, L15

Crawford, C. S. and Fabian, A. C.: 1996, *Mon. Not. R. Astron. Soc.* **281**, L5

de Koff, S., Baum, S. A., Sparks, W. B., Biretta, J., Golombek, D., Macchetto, F., McCarthy, P., and Miley, G. K.: 1996, *Astrophys. J., Suppl. Ser.* **107**, 621

de Vaucouleurs, G.: 1948, *Journal des Observateurs* **31**, 113

Dey, A., van Breugel, W., Vacca, W. D., and Antonucci, R.: 1997, *Astrophys. J.* **490**, 698

Ellerbroek, B. L. and Rigaut, F. J.: 2000, *Preprint, to appear in SPIE*

Ferland, G. J. and Osterbrock, D. E.: 1986, *Astrophys. J.* **300**, 658

Fernini, I., Burns, J. O., Bridle, A. H., and Perley, R. A.: 1993, *Astron. J.* **105**, 1690

Freeman, K. C.: 1970, *Astrophys. J.* **160**, 811

Fried, D. L.: 1982, *J. Opt. Soc. Am.* **72**, 52

Giavalisco, M., Steidel, C. C., and Macchetto, F. D.: 1996, *Astrophys. J.* **470**, 189

Gower, J. F. R., Scott, P. F., and Wills, D.: 1967, *Mem. R. Astron. Soc.* **71**, 49

Gwyn, S. D. J.: 2000, *Private Communication*

Hickson, P., Bell, A., Buttner, G., Drissen, L., Hardy, T., Hutchings, J. B., Morbey, C., Murowinski, R., Rowlands, N., Steinbring, E., and Stetson, P.: 1999, *NRC/NASA Internal Report*

Hill, G. J. and Lilly, S. J.: 1991, *Astrophys. J.* **367**, 1

Hu, E. M., McMahon, R. G., and Egami, E.: 1996, *Bull. American Astron. Soc.* **28(2)**, 853

Hubble, E. P.: 1926, *Astrophys. J.* **64**, 321

Hutchings, J. B., Crampton, D., Morris, S. L., Durand, D., and Steinbring, E.: 1999, *Astron. J.* **117**, 1109

Hutchings, J. B., Crampton, D., Morris, S. L., and Steinbring, E.: 1998, *Publ. Astron. Soc. Pac.* **110**, 374

Ivison, R. J., Papadopoulos, P., Seaquist, E. R., and Eales, S. A.: 1996, *Mon. Not. R. Astron. Soc.* **278**, 669

King, I. R., Anderson, J., Cool, A. M., and Piotto, G.: 1998, *Astrophys. J., Lett.* **492**, L37

Kolmogorov, A. N.: 1941, *Dan. SSSR* **30(4)**, 229

Lacy, M. and Rawlings, S.: 1994, *Mon. Not. R. Astron. Soc.* **270**, 431

Le Fèvre, O., Deltorn, J. M., Crampton, D., and Dickinson, M.: 1996, *Astrophys. J., Lett.* **471**, L11

Leyshon, G. and Eales, S. A.: 1998, *Mon. Not. R. Astron. Soc.* **295**, 10

Lilly, S., Fall, M., Stiavelli, M., Madau, P., Loeb, A., Gardner, J., and Rieke, M.: 1998, *NGST Ad-Hoc Science Working Group Design Reference Mission*

Lilly, S. J. and Longair, M. S.: 1984, *Mon. Not. R. Astron. Soc.* **211**, 833

Lin, H., Yee, H. K. C., Carlberg, R. G., Morris, S. L., Sawicki, M., Patton, D. R., Wirth, G., and Shepherd, C. W.: 1999, *Astrophys. J.* **518**, 533

Lister, M. L., Hutchings, J. B., and Gower, A. C.: 1994, *Astrophys. J.* **427**, 125

Longair, M. S., Best, P. N., and Röttgering, H. J. A.: 1995, *Mon. Not. R. Astron. Soc.* **275**, L47

MacKenty, J. W.: 1999, *Bull. American Astron. Soc.* **31(3)**, 984

Mahajan: 1983, *Applied Optics* **22**, 3035

McCarthy, P. J.: 1993, *Ann. Rev. Astron. & Astrophys.* **31**, 639

McCarthy, P. J., Kapahi, V. K., van Breugel, W., and Subrahmanya, C. R.: 1990, *Astron. J.* **100**, 1014

McCarthy, P. J., van Breugel, W., Spinrad, H., and Djorgovski, S.: 1987, *Astrophys. J., Lett.* **321**, L29

Morbey, C.: 1999, *NRC Internal Report*

Morris, S. L.: 1999, *Private Communication*

Nadeau, D., Murphy, D. C., Doyon, R., and Rowlands, N.: 1994, *Publ. Astron. Soc. Pac.* **106**, 909

Naim, A., Ratnatunga, K. U., and Griffiths, R. E.: 1997, *Astrophys. J.* **476**,

510
Noll, R. J.: 1976, *J. Opt. Soc. Am.* **66(3)**, 207
Northcott, M. J.: 1991, *Proc. Int. Soc. Optical Eng.* **1542**, 254
Peebles, P. J. E.: 1993, *'Principles of Physical Cosmology'*, Princeton University Press, Princeton
Pentericci, L., Röttgering, H. J. A., Miley, G. K., McCarthy, P., Spinrad, H., van Breugel, W. J. M., and Macchetto, F.: 1999, *Astron. Astrophys.* **341**, 329
Pilkington, J. D. H. and Scott, P. F.: 1965, *Mem. R. Astron. Soc.* **69**, 183
Pritchet, C. J.: 2000, *Private Communication*
Racine, R.: 1996, *Publ. Astron. Soc. Pac.* **108**, 699
Racine, R. and Ellerbroek, B. L.: 1995, *Proc. Int. Soc. Optical Eng.* **2534**, 248
Rhee, G., Marvel, K., Wilson, T., Roland, J., Bremer, M., Jackson, N., and Webb, J.: 1996, *Astrophys. J., Suppl. Ser.* **107**, 175
Rich, R. M. and Margon, B.: 1998, *NGST Ad-Hoc Science Working Group Design Reference Mission*
Rigaut, F., Salmon, D., Arsenault, R., Thomas, J., Lai, O., Rouan, D., Véran, J. P., Gigan, P., Crampton, D., Fletcher, J. M., Stilburn, J., Boyer, C., and Jagourel, P.: 1998, *Publ. Astron. Soc. Pac.* **110**, 152
Rigaut, F. J., Arsenault, R., Kerr, J. M., Salmon, D. A., Northcott, M. J., Dutil, Y., and Boyer, C.: 1994, *Proc. Int. Soc. Optical Eng.* **2201**, 149
Roddier, F.: 1981, *Progress in Optics* **19**, 281
Roddier, F.: 1994, in *Adaptive Optics for Astronomy, Procedings of the NATO Advanced Study Institute on Adaptive Optics for Astronomy held June 29 - July 9 1993, Cargese, France, Eds. Alloin, D. M. and Mariotti, J. -M., Kluwer Academic, Boston*, p. 89
Röttgering, H. J. A., Lacy, M., Miley, G. K., Chambers, K. C., and Saunders, R.: 1994, *Astron. Astrophys. Suppl. Ser.* **108**, 79
Schlegel, D. J., Finkbeiner, D. P., and Davis, M.: 1998, *Astrophys. J.* **500**, 525
Steidel, C. C., Giavalisco, M., Pettini, M., Dickinson, M., and Adelberger, K. L.: 1996, *Astrophys. J., Lett.* **462**, L17
Steinbring, E.: 1998, *NRC Internal Report*
Steinbring, E.: 1999A, *NRC Internal Report*
Steinbring, E.: 1999B, *NRC Internal Report*
Steinbring, E.: 2000, in *Next-Generation Space Telescope Science and Technology, Astron. Soc. Pac. Conf. Series 207, Procedings of September 13-16*

1999 in Hyannis, MA, Eds. Smith, E., and Long, K., p. 526

Steinbring, E., Crampton, D., and Hutchings, J. B.: 1998, *Bull. American Astron. Soc.* **30(4)**, 1280

Stockton, A., Canalizo, G., and Ridgway, S. E.: 1999, *Astrophys. J., Lett.* **519**, L131

Storrie-Lombardi, L. J., Weymann, R. J., McLeod, K. K., Rieke, G. H., Hill, J., and Kulkarni, V.: 1998, in *NICMOS and the VLT: A New Era of High Resolution Near Infrared Imaging and Spectroscopy, Procedings of June 26-27 1998 in Pula, Italy, ESO Conf. and Workshop Proc., Eds. Freudling, W. and Hook R.*, p. 207

Tessier, E.: 1996, *Proc. Int. Soc. Optical Eng.* **2534**, 178

van Ojik, R., Röttgering, H. J. A., van der Werf, P. P., Miley, G. K., Carilli, C. L., Visser, A., Isaak, K. G., Lacy, M., Jenness, T., Sleath, J., and Wink, J.: 1997, *Astron. Astrophys.* **321**, 389

Véran, J. P.: 1998, *NRC Internal Report*

Véran, J. P., Rigault, F., and Maître, H.: 1996, in *Adaptive Optics, Procedings of October 2-6 1995, Garching, Germany, ESO Conf. and Workshop Proc., Ed. Cullum, M.*, p. 497

West, M. J.: 1994, *Mon. Not. R. Astron. Soc.* **268**, 79

Wheelock, S.: 1994, *STScI Internal Report*

Yee, H. K. C. and Green, R. F.: 1987, *Astrophys. J.* **319**, 28

Zirm, A., Dey, A., Dickinson, M., McCarthy, P. J., Eisenhardt, P., Djorgovski, S. G., Spinrad, H., Stanford, A., and van Breugel, W.: 1998, *Bull. American Astron. Soc.* **30(4)**, 1412

Glossary

AGN: active galactic nucleus

AO: adaptive optics

AOB: Adaptive Optics Bonnette

CADC: Canadian Astronomical Data Centre

CCD: charge-coupled device

CFHT: Canada-France-Hawaii Telescope

CSA: Canadian Space Agency

DM: deformable mirror

DRM: Design Reference Mission

FWHM: full width at half-maximum

HIA: Herzberg Institute of Astrophysics

HST: Hubble Space Telescope

HzRG: high-redshift radio galaxy

IDL: Interactive Data Language

IFU: integral field unit

IGM: intergalactic medium

IRAF: Image Reduction and Analysis Facility

KIR: 1024 × 1024 Infrared Array

MONICA: Montreal Near-Infrared Camera

MOS: multi-object spectrograph

NASA: National Aeronautics and Space Administration

NED: NASA Extragalactic Database

NGST: Next-Generation Space Telescope

NICMOS: Near-Infrared Camera and Multi-Object Spectrograph

NIR: near-infrared

NRC: National Research Council of Canada

PSF: point-spread function.

QSO: quasi-stellar object

SED: spectral energy distribution

STSDAS: Space Telescope Science-Database Analysis System

UV: ultraviolet

VI: Visible Imager

WFPC2: Wide-Field Planetary Camera 2

WFS: wavefront sensor

actuator: A device for manipulating the surface of a deformable mirror.

ANALYSIS: A package in IRAF for performing reductions of digital images.

AOTOOLS: The author's IRAF package for image processing of adaptive optics observations.

aperture photometry: Measuring the flux in an aperture centred on an object.

bad-pixel: A section, usually a single pixel or a small group of pixels, of a digital imaging device that does not operate properly. That is, with a non-linear response to input flux.

BADPIXEL: The author's IRAF program for finding and generating a map of bad pixels.

DAOFIND: An IRAF task for finding point-sources in images.

DAOPHOT: An IRAF task for performing aperture photometry on images.

DEGRADE: The author's IRAF package for accounting for changes in the adaptive optics point-spread function due to changes in seeing and anisoplanicity.

DIGIPHOT: An IRAF package for performing photometry on digital images.

DITHER: The author's IRAF task for reconstructing image mosaics.

D/r_0: The ratio of telescope pupil diameter to characteristic size of turbulent cells.

ELLIPSE: An IRAF task for determining elliptical isophotes for a galaxy.

F555W: A Hubble Space Telescope broadband filter centred at 5550 Angstroms.

F569W: A Hubble Space Telescope broadband filter centred at 5690 Angstroms.

F622W: A Hubble Space Telescope broadband filter centred at 6220 Angstroms.

F675W: A Hubble Space Telescope broadband filter centred at 6750 Angstroms.

F702W: A Hubble Space Telescope broadband filter centred at 7020 Angstroms.

F785W: A Hubble Space Telescope broadband filter centred at 7850 Angstroms.

F814W: A Hubble Space Telescope broadband filter centred at 8140 Angstroms.

FLATFIELD: The author's IRAF task for generating flat-field images from target observations.

flat-fielding: The compensation of the pixel-to-pixel variation of sensitivity of a digital detector.

H: A near-infrared broadband filter centred at 16000 Angstroms.

IMAGES: An IRAF package for the manipulation of digital images.

IMEXAM: An IRAF task for measuring the flux in digital images.

J: A broadband infrared filter centred on 12000 Angstroms.

K: A broadband infrared filter centred on 22000 Angstroms.

micro-mirror: A miniature micro-machined device composed of hundreds or thousands of individual mirrors.

NGST VI/MOS: The author's Next Generation Space Telescope Visible Imager and Multi-Object Spectrograph simulation program.

OFFAXIS: The author's program for determining the correction of the adaptive-optics point-spread function due to offsetting the telescope.

ONAXIS: The author's program for determining the correction of the adaptive-optics point-spread function due to changing natural seeing conditions.

PERSISTENCE: The author's program for determining the persistent signal - video noise - in a near-infrared detector.

persistence: A unwanted signal often associated with near-infrared detectors. Often referred to as video noise.

polarization: The percentage of incoming electromagnetic waves which are all oscillating in the same direction as opposed to random directions. Polarization in astrophysical applications is typically associated with scattering by dust.

pupil: The surface area of a telescope presented to the sky.

reconstruction map: The map of functions generated by the author's program DEGRADE which can be used to reconstruct the anisoplanicity of the adaptive-optics point-spread function.

R: A broadband filter centred at about 7000 Angstroms. Also, a dimensionless measure of the resolution of spectra.

r_0: The galaxy-galaxy correlation length. Also, the characteristic scale of atmospheric turbulence.

S/N: The ratio of signal to noise in an observation.

spectropolarimetry: A method for determining the fraction of polarization as a function of wavelength.

star-field: A small region of sky with an abundance of bright stars suitable for determination of the adaptive-optics point-spread function.

Strehl-ratio: The ratio of the height of the telescope point spread function to the expected result for an ideal telescope in space.

tip-tilt: The first aberrations after piston of the Zernike modes. These correspond to image motion.

TV: An IRAF task for display of digital images.

Zernike modes: A basis set of vectors describing the deformations induced by the Earth's atmosphere on an incoming plane wave.